Development of Broadly Tunable Parametric Light Sources and Their Application to Alkali Metal - Small Molecule Cluster Spectroscopy

Thesis by

Sheng Wu

In Partial Fulfillment of the Requirements
for the Degree of
Doctor of Philosophy

California Institute of Technology
Pasadena, California

1999
(Submitted May 19, 1999)

Acknowledgements

I am indebted to many people for the enjoyable and maturing experience during my seven years at Caltech. The first mentor that I wish to mention is Geoff Blake, who led me into the field of non-linear optical research, and gave me an unbelievable amount of freedom in exploring the latest developments. His interest in all aspects of science and breadth of knowledge are so profound that I am continually inspired to explore further.

The Blake group as a whole has been a very pleasant environment. Dave Rodham is my colleague and mentor, his exactness and diligence in conducting experiments gave me a good example of how to conduct scientific independent experiments. His kind suggestions on the ZEKE-PFI experiment helped me greatly in the last two months of data collection. Zulf Morbi is instrumental in the last year of experiments, his insight in spectroscopy and enthusiasm for results push me to work harder. Vadym Kapinius is a very bright young researcher, his hard work proved the idea of the seeded *ns* OPG/OPA design. I also want to mention Zifu Wang and Hui Zhang, whose work helped to prove the usefulness of the tunable laser sources. I am indebted to Pin Chen, Brian Meehan and Shuzi Matssura, who were always generous with their time and whose good cheer makes the Blake group a very pleasant place to work.

In all experimental chemical physics research, an essential prerequisite is a well equipped machine shop with very talented people. My work here would have been impossible without the help from Guy Duremburg, Mike Roy, Ray Garcia, Tom Dunn and Rick Gerhart. I am quite fortunate to have met them during my graduate school years, for they not only helped me on the machining, but also on dealing with the misfortunes of life.

The work here has also been made possible because of the help from CASIX, in particular, President Wang, John Ling and Sunny Sun. They are walking on a trail that they must blaze by themselves — high tech in a third world country. They are,

as the company's logo says, the "Light from China."

I am also indebted to my wife, Ying Feng, who has spent endless long nights with me during the last year of experiments. My thesis work would have dragged on much longer without her help in all aspects of my life.

Of course, none of this would have happened if not for my parents, especially my mom. My humble work presented here is a result of what they did for me. For their love and support, I dedicate this thesis to my Parents and my family.

Abstract

Widely tunable laser sources based on second order nonlinear optical (NLO) conversions and covering the 200 nm to 3 μm region have been constructed. Considerable effort is devoted to achieving reasonable linewidth and efficiency, two critical parameters for the practical use of NLO materials in spectroscopic and other experiments. Using these devices, the ionization behavior of alkali metal - small molecule clusters is explored. In particular, the spectroscopic results are used to investigate the physics of solvation between potassium atoms and ions with small molecules.

Recent advances in the fabrication of nonlinear optical materials have led to the discovery of several promising crystal candidates for high power applications. These advances, coupled with the rapid progress in high power pulsed pump laser technology, have made practically possible widely tunable laser sources based on nonlinear optical conversions. Three major devices have been developed that provide continuous coverage from 200 nm to 3 μm, and which combine reasonable power efficiency with a range of linewidths suitable for various spectroscopic measurements.

The design philosophy throughout is to create practical devices that are as simple and durable as possible. For example, a compact, low cost OPO based on type II phase matching in BBO and off-the-shelf optics has been fabricated. The type II BBO OPO is fully computer controlled, and provides wide tunability ($\approx$ 410 nm to 3 μm) and relatively narrow bandwidth ($\approx 1\ cm^{-1}$) in the same package. To generate narrow bandwidth radiation, *e.g.*, close to the transform limit, an extremely simple, unidirectional Optical Parametric Generator/Optical Parametric Amplifier (OPG/OPA) is designed based on an intense nanosecond (*ns*) pump source. Compared with other CW laser-seeded optical parametric devices, this OPG/OPA design combines simple operation with a remarkable insensitivity to the matching of the seed laser frequency to the OPO cavity mode. Numerical models are used to fully characterize the NLO behavior of these cavities, and to optimize their performance.

Finally, in order to produce UV harmonics of the fundamental oscillators, a broadly tunable harmonic generator which effectively covers the 190 to 420 nm region has been constructed. The thermal dephasing problem in high average UV power generation with NLO crystals is fully explored for the first time, and a new method of overcoming this thermal dephasing problem is proposed and tested. For each of the devices, several experiments had been carried out to characterize their performance, particularly their wide tunability, ease of operation, and high power scalability.

Most importantly for this thesis, fundamental research on the interaction between potassium and small molecules such as water, ammonia, and benzene has been carried out with the above mentioned laser sources by collecting the Photo-Ionization Efficiency (PIE) ion yield and Zero Kinetic Energy Electron - Pulsed Field Ionization (ZEKE-PFI) spectra of neutral alkali metal-solvent clusters. The tuanble sources made it possible to rapidly map out the ionization potentials of the different clusters, and to thereby estimate the binding energies of the neutral and ionic clusters; while the ZEKE-PFI spectra of $K(NH_3)$ reveal, as expected, a considerable increase in the angular anisotropy of the intermolecular forces in the charged clusters. Interestingly, the measured pair-pair interaction energies of the dimers stand in contradiction to the ion selectivity achieved by biological systems. Many body forces therefore must contribute substantially to the subtle balancing of forces that operate in the condensed phase, and the results indicate the importance of further characterization of large clusters, especially those with mixed constituents such as $K(C_6H_6)_n(H_2O)_m$. Additional applications in fields as diverse as atmospheric science and molecular astrophysics can be expected as NLO materials and processes are further refined.

Contents

List of Figures

List of Tables

Chapter 1 Introduction & motivation

1.1 Overview

The 200 nm to 3 μm region of the electromagnetic spectrum is of great importance to the study of many chemical, physical, and biological processes. Convention divides this interval into three distinct regions: Ultra-Violet (UV) radiation extends from 200 - 380 nm, Visible (Vis) light covers the 380 - 780 nm range, and the near-infrared (NIR) lies between 780 nm and 3 μm. Historically, the fundamentals of molecular spectroscopy emerged from studies in these regions, and they remain of great importance to many fields of scientific research to this day.

The workhorse methods of generating continuously tunable laser radiation to cover the 200 nm to 3 μm region include dye lasers and color center-based systems such as Ti:Sapphire. Lasers of this type matured in the 1970-1980s, are commercially available, and are in widespread use today. Their utility in a number of applications, however, is limited by a number of factors, one being their narrow tuning range. A dye lasers, for example, requires dozens of dyes in order to cover the visible range, while there are few dyes that lase efficiently beyond 1 μm. Furthermore, changing dyes is a time consuming process and the solvents/chemicals used are often toxic to humans along with being damaging to the environment. Although there has been progress on solid state dye discs, the lifetime and tuning range of these devices remains limited. Ti:Sapphire lasers are solid state systems with a fairly wide tuning range and a long lifetime. Compared to the potential tuning range of the UV pumped optical parametric devices presented in this thesis, the Ti:Sapphire laser's tuning range (680 nm to 1100 nm) is still relatively small. This situation is unfortunate since many scientific disciplines – including chemical physics, astrophysics, cosmochemistry, planetary/atmospheric sciences, to name but a few – rely on widely tunable laser sources to acquire essential information.

The remainder of this chapter discusses the types of chemical and physical questions that demand the use of broadly tunable all solid state laser sources. The major scientific focus will be on how the unique capabilities of parametric devices aid in the spectroscopic study of weakly bound small molecule - alkali metal/alkali metal cation clusters, but also briefly discuss in this chapter other potential applications of widely tunable laser sources in the fields of atmospheric chemistry and molecular astrophysics. We then summarize traditional tunable laser technologies, identify their most important shortcomings, and compare them to all solid state sources based on (NLO) conversions. Parametric oscillators and amplifiers are potentially devoid of such inherent drawbacks as limited tuning range, short lifetime, complicated plumbing setups, and environmental pollution associated with, e.g., dye lasers, and such devices are thus suitable for a new generation of tunable light sources. The research described here has contributed significantly toward demonstrating many aspects of the considerable potential of NLO conversions in the UV/Vis and NIR regions, but some important issues in the means of achieving both high efficiency and narrow bandwidth remain to be addressed.

1.2 Spectroscopy in the 200 nm to 3 μm region with nanosecond laser sources

A nanosecond (ns) laser source operating in the 200 nm to 3 μm region can be used to investigate a wide range of fundamental scientific problems. Many molecules have excited electronic states in the UV/visible range that can be pumped by a widely tunable laser source. Probing the electronic transitions of molecules, and any subsequent photophysical or reaction pathways such as intersystem crossing or predissociation, can yield an enormous amount of information about the properties of such compounds. Field or remote sensing studies of atmospherically relevant molecules involving coherent sources are a powerful means of examining the composition of the Earth's and other planetary atmospheres, and the chemical processes that occur therein.

Rovibrational spectra are located in the infrared. Typically, for larger molecules the unique, or "fingerprints", features in their spectra occur in the 5-20 μm region. Therefore, widely tunable IR laser sources would provide a powerful tool to identify different chemicals, to determine their abundance, and to study their vibrational dynamics. While sources in the 1-3 μm range are usefuly only for molecules containing hydrogenic stretches, they often form the basis for additional NLO conversion schemes to generate tunable mid-infrared light.

Pulsed lasers produce high energies over short periods of time that can be used to carry out ionization or dissociation spectroscopic experiments, where the high peak intensity is required to achieve high detection efficiencies. In such studies, or in absorption measurements, a major disadvantage of pulsed lasers is their shot-to-shot amplitude noise. The recent development of cavity ringdown laser absorption spectroscopy (CRLAS), however, reduces tremendously the sensitivity to such fluctuations, to the extent that nearly quantum-limited absorption spectroscopy can now be carried out with pulsed lasers. Furthermore, signal normalization schemes in ionization-based spectroscopies have also been developed over the past decade. Thus, widely tunable pulsed lasers are now quite attractive for detailed spectroscopic studies, as will be discussed at the end of this thesis.

The investigations presented here have been motivated by three primary goals:

- basic research in understanding the molecular structure and interactions of weakly bound clusters involving alkali metals.
- data collection for the analysis of remote sensing studies of the atmosphere and the interstellar medium, *e.g.*, photolysis cross section measurements
- remote sensing instrumentation development for space/air-borne missions

We discuss each, briefly, in turn below.

1.2.1 Spectroscopy of alkali - small molecule clusters

Many important chemical and biochemical processes involve the recognition and selection of specific molecules. One example is the Na^+/K^+ ATPase pump, which removes Na^+ from and imports K^+ into cells, thereby maintaining high intracellular K^+ and low intracellular Na^+ concentrations [4, 5]. To accomplish this task, the ATPase membrance protein has sites of high Na^+ affinity on the interior of the cell membrane, and sites of high K^+ affinity on the exterior, sites that are able to remove the ions, selectively, from the surrounding water. The ability of these binding sites to distinguish between Na^+ and K^+ depends on the site structure and on the energetics of removing the ions from water and placing them in the sites. It is difficult to explain the enormous difference in the permeability (10,000 to 1) of K^+ and Na^+ given only the differences in their ionic radii (0.97Å for Na^+, 1.33Å for K^+). Recently, the Lisy group [2] has observed size selectivity in the gas phase cation-π interactions of alkali metal cations with water and benzene. Their results indicate that $K^+(H_2O)_n$ clusters can be dehydrated by benzene, while $Na^+(H_2O)_n$ clusters cannot. This supports theoretical arguments that aromatic π bonding can compete successfully with water molecule interactions, but that for Na^+, the bonding between Na^+ and water is favored. $Na^+(H_2O)_n$ clusters, because of their large size, cannot pass through the ion channel. For K^+, the competition favors bonds between K^+ and benzene, and the $K^+(H_2O)_n$ clusters can be dehydrated, allowing the desolvated K^+ ion to pass through. Ultimately, such theories needs to be tested with quantitative thermodynamic or structural data and accurate intermolecular force fields, data that currently cannot be obtained by theoretical calculation alone.

Signal transmission in nerve cells, accomplished by voltage-gated ion channel membrane proteins, also depends critically on the interaction between polar (and possibly non-polar) molecules and Na^+ and K^+ [6, 10, 11]. Upon opening, Na^+ channel proteins selectively allow Na^+ ions to flow into the cell, while the K^+ channel proteins selectively allow K^+ to leave the cell. The ion selectivity achieved by these proteins is determined not only by the interaction between the ion and the pore region

of the protein, but also the water-cation and water-polar molecule interactions in the pore. Other factors affecting selectivity are hydrogen bonding between the pore and the water molecules surrounding the ion, and the physical dimensions of the pore's selectivity filter. Selected illustrations of ion channels are shown in Figure 1.1.

Although high-resolution structural data are not yet available for ion channel pores, there is evidence which indicates that Na^+ channel pore dimensions are approximately 0.3 nm $\times$ 0.5 nm, making them larger than the K^+ channel pores, which are believed to be 0.3 nm $\times$ 0.3 nm in size [7]. The Na^+ pores are thought to be formed from the interaction of Na^+ with partially-negative oxygen atoms such as those in carbonyl groups, while K^+ pores may involve the cation-π interaction between K^+ and non-polar aromatic rings, as shown in Figure 1.1c [8, 9, 3]. Recent theoretical results have suggested that the Na^+ channel pores must be large enough to allow a Na^+ ion along with its first solvation shell of water molecules to pass through intact. Na^+ has difficulty passing through K^+ channel pores because the desolvation required to drive the dehydrated Na^+ through the smaller pore is energetically prohibitive [12]. The results further suggest that K^+ does not pass through Na^+ channel pores because its interaction with H_2O is not sufficiently strong to displace the H_2O molecules in the pores, which are hydrogen-bonded to polar side groups on the protein. In the K^+ channels, the cation-π interaction is strong enough to displace the water molecules of hydration surrounding the K^+, thereby allowing it to pass through the channel.

While structural data for ion channels is lacking, some insight may be gained from the recently determined structure of the K^+ binding site in another protein, the dialkylglycine decarboxylase (DGD) enzyme, in which a K^+ ion in the site is coordinated by six oxygen atoms in an octahedral arrangement, as shown in Figure 1.1d [13]. Three oxygens are from carbonyl groups, and the other three are supplied by a carboxyl group, a hydroxyl group, and a water molecule. When a Na^+ ion occupies the site, the cavity shrinks to accommodate the smaller ion, forcing the hydroxyl oxygen out of the cavity and leaving the Na^+ coordinated by five oxygens in a distorted trigonal bipyramidal geometry. The site preferentially binds K^+, the selectivity being determined by the energetics of the interaction of the ions with the

Figure 1.1: (a) Schematic illustration of ion channel proteins embedded in a cell membrane [6]. (b) Cut-away illustration of an ion channel protein showing the water-filled pore and the selectivity filter [6]. (c) Illustration of the proposed selectivity filter in K^+ channel proteins (from Miller[3]). (d) Illustration of the K^+ binding site in DGD (from Miller[3]).

(a) (b)

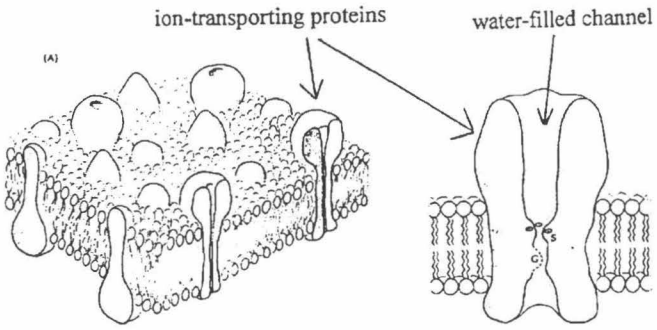

Ion channels in cell membrane select between Na^+ and K^+

(s) selectivity filter

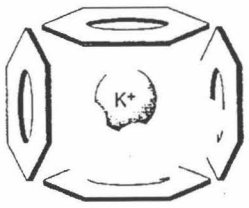

Proposed binding site

(c)

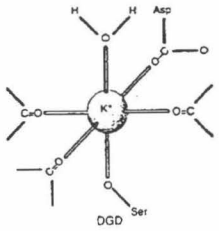

K^+ binding site

(d)

polar oxygen-containing groups as well as that of the overall protein structure.

Clearly, accurate intermolecular potential energy surfaces, or IPESs, describing the interaction between alkali metal ions and water and between the ions and groups that might line ion channels are required in order to determine how ion channels and protein binding sites achieve selectivity. Although much has been learned about alkali ion hydration from thermochemical and transport data [14], neutron diffraction [15], Raman spectroscopy [16], and theoretical methods [17, 18, 19], the modeling of the complex environment inside the ion channels and protein binding sites requires more accurate information on structure and energetics than these methods can provide. In order to provide stringent guides for computational work, the IPES describing the interaction between an alkali ion and one water molecule must be determined precisely, as must the IPESs describing alkali ion interactions with several solvent molecules.

The best way to gather the necessary experimental data is through the spectroscopic study of isolated clusters composed of an alkali metal ion and one to a few solvent molecules in the gas phase. While binding energies of clusters composed of Na^+ and a small number of water or ammonia molecules have been measured in high pressure mass spectrometry experiments [20, 21], there are only a handful of measurements of vibrational frequencies of such clusters. Hertel and coworkers, for example, have measured the sodium-water and sodium-ammonia stretching frequencies in the 1:1 clusters [22, 23]. No direct structural data exists for any of these species, but numerous calculations of their structures agree quite well [24, 25, 26, 27]. Accurate experimental structural data is still desired, however, because small changes in the geometry and energetics can have large consequences in constricted ion channels and binding sites.

As a further step toward acquiring the necessary structural and vibrational data, and following previous work in the Blake group by Rodham *et al.* on the $Na(H_2O)$ and $Na(NH_3)$ clusters [15, 16], a modified "pick-up" source has been used to create jet-cooled $K(H_2O)_n$, $K(NH_3)_n$, and $K(C_6H_6)_n$ clusters. A combination of threshold photoionization efficiency (PIE), zero kinetic energy electron-pulsed field ioniza-

tion (ZEKE-PFI), and resonance enhanced multi-photon ionization (REMPI) spectroscopies have been used to study them. ZEKE-PFI spectroscopy in particular is a powerful technique for obtaining high resolution spectra of molecular and cluster ions. This technique is based on the detection of threshold photoelectrons generated in the laser ionization of their neutral precursors [28]. With this technique, precise ionization potential and vibrational frequencies of certain clusters were measured, and some structural and interaction energy information inferred.

1.2.2 Research in atmospheric chemistry with all solid state laser sources

Studies of photolysis mechanisms

The wide tunability and high output powers of the light sources described herein have led to a number of other experiments in the Blake group. For example, the coupling of radiation and chemistry in the upper troposphere and lower stratosphere is very important to our understanding of the chemical balance of the environment, yet much uncertainty remains. For example, the photodissociation of a number of gases (e.g., nitric and peroxynitric acids) in these regions of the atmosphere may be driven by radiation longward of 300 nm where the photodissociation cross sections are very poorly known. A widely tunable, high average power laser would be very helpful in carrying out any new measurements by coupling an intense photolysis source with sensitive laser induced fluorescence detection systems.

Another example is provided by recent studies of nitrous oxide, or N_2O. N_2O is an important greenhouse gas and the major natural source of NO that initiates the catalytic NO_x ozone destruction cycles in the stratosphere. N_2O concentrations have been increasing rapidly for the past several decades, and it is uncertain what is causing this change. Measurements of the isotopic composition of atmospheric trace gases can be a useful tool for inferring their global production and loss rates. In this technique, if the isotopic signature of the various sources and sinks are known, then the atmospheric composition (that is, the concentration and ratios of the different

isotopomers) provides additional constraints on the sources and sinks.

Photolysis in the upper atmosphere represents the primary sink of N_2O. Caltech and JPL researchers have suggested [29] that N_2O should be isotopically fractionated as a result of this process. In particular they suggested that because the zero point vibrational energy of the isotopomers are different, the absorption cross section in the ultraviolet will be shifted as a result, leading to different photolysis rates for the different isotopomers. This mechanism has now been verified by experiments in the Blake group [30] in which the ^{15}N and ^{18}O isotopic signatures are measured as a function of the extent of photolysis at different wavelengths. The high average power and tunability of the parametric oscillators were essential to these experiments.

Atmospheric sensing and monitoring of reactive species

Laboratory studies of the mechanisms of photo-induced chemistry is essential to understanding the changes that are occurring in the atmosphere. At the same time, there is an urgent need to monitor the chemical composition of the atmosphere, particularly the reactive free radicals that drive much of the chemistry in the stratosphere and troposphere, *e.g.*, the OH radical [32], NO [31], and the BrO radical [33]. To carry out such *in situ* measurements, especially when multiple chemical species must be monitored simultaneously, widely tunable laser sources would be of great utility. Since these instruments must be airborne, there are stringent requirements on power consumption, size and weight, as well as the lifetime and reliability of the tunable laser sources and the sensitivity of the instruments. In this regard, all solid state laser sources based on nonlinear optical conversion would seem to be promising candidates for a new generation of spectrometers.

1.3 200 nm $\rightarrow$ 3 μm ns laser sources

1.3.1 Motivation

The preceding discussion elucidates the importance of spectroscopy in the 200 nm to 3 μm region for furthering our knowledge in chemical physics and the atmospheric sciences. In the following section, the attributes of an ideal, widely tunable ns pulsed laser source that covers this region will be outlined. The advantages and disadvantages of traditional tunable lasers to laser sources based on nonlinear optical conversions that form the basis of this thesis will then be compared.

1.3.2 The ideal, widely tunable ns laser source

An ideal widely tunable laser source would have the following qualities:

1. *High spectral resolution*: Transform limited resolution is ultimately desired for most spectroscopic studies. For a pulsed laser of width τ seconds, the transform limited resolution ($\delta\nu_{trans.}$) is

$$\delta\nu_{trans.} = \frac{1}{2\pi\tau c} \quad , \tag{1.1}$$

   where c is the speed of light in vacuum. Lasers with bandwidths of one to a few wavenumbers can be very useful in certain environment monitoring situations, however, particularly for preliminary or pilot studies.

2. *Frequency accuracy*: Line frequencies are the primary result of many spectroscopic experiments. Complicated mechanical designs often result in unstable laser frequencies, or lasers that can be difficult to calibrate.

3. *Wide tunability*: Continuous and wide-band tuning capabilities are highly desirable. Here, tunability not only means the possibility of tuning from one wavelength to the other, but also ease of use when changing wavelengths. This is especially true for narrow bandwidth operation, because narrow bandwidths

typically require much more complicated tuning mechanisms than those for broadband operation. The repeatibility of the wavelength setting and high power output are also challenging requirements.

4. *Long-term reliability*: For experiments on space/air-borne platforms, where manual maintenance opportunities are scarce or non-existent, long-term reliability is indispensable. For laboratory experiments, a spectrometer that demands frequent maintenance can eat up a staggering amount of research budget and man-hours over time.

5. *Automated operation*: Similar to the previous item, automated operation is indispensable for space/air-borne experiments. It also tremendously facilitates laboratory data acquisition.

6. *Small size and light weight*: Because limited space is available on space or air-borne systems, it is important for laser sources to be compact. Thus the preference of all solid state lasers over liquid solvent dye lasers that may require additional circulation and cooling accessories.

7. *Low power consumption*: These last three items, while very desirable in the laboratory, are absolutely critical to satellite/air-borne projects, where space, weight, and power are tightly rationed. Therefore, all solid state lasers must continually improve their efficiency. This is a major goal to be kept in mind during the development of laser devices such as those described in this thesis.

8. *Robustness*: A laser source that is not robust enough to pass flight-qualification tests will not be allowed on a satellite or air-borne platforms. Robustness to varying environmental conditions also sets a high standard for the thermal and opto-mechanical design of laser systems.

9. *Low cost*: The cost not only includes the prices paid at the time of purchase, but also the operational cost — for example, electric power consumption, and regular material changes, *e.g.*, gases, tubes, dyes, etc.

1.3.3 Traditional 200 nm to 3 μm ns tunable laser sources

The traditional tunable lasers in this region include:

- *Dye lasers*: Dye lasers are usually pumped by UV or visible (green) lasers. They have a wide tuning range from the near-UV/deep blue to the near IR. Each dye, however, only has a limited tuning range, and frequent dye changes are therefore needed when scans from one wavelength region to another are desired. Solid state laser dye discs are much easier to handle compared to dyes in liquid solvent, and there has been tremendous progresses in their lifetimes and damage thresholds, but at present such discs are available only over a limited portion of the full operating range of dye lasers.

- *Color center lasers*: These lasers use crystals such as Ti:Sapphire, Cr:LiSAF, Cr:LiSGaF and Cr:LiCAF as the gain medium, and they can cover a wider range with a single crystal than can dye lasers. Still, the tuning range is rather limited for many applications. For example, the Ti:Sappire laser has the widest tuning range of these systems, covering the 680 nm to 1100 nm interval when pumped in the green. Cr:LiSAF has a slightly smaller tuning range but can be pumped by diode lasers directly at 630 nm; while Cr:LiCAF can be pumped at 266 nm to provide direct tunability between 280 and 320 nm [37].

- A variety of other pulsed, tunable lasers can be envisioned in this region, but they are not as widely used as dye or color center lasers.

1.3.4 All solid state, widely tunable ns lasers based on NLO conversions

The recent progress in nonlinear optical (NLO) materials and solid state pump lasers has triggered rapid developments in all solid state widely tunable laser sources. The discoveries of new nonlinear optical crystals, such as KTP/KTA, several members in the borate crystal families (*e.g.*, BBO, LBO and CLBO, etc.), and periodically polled materials (*e.g.*, PPLN, PPKTP), have made the practical the longstanding

Table 1.1: General comparison of traditional lasers and optical parametric devices

Devices	*OPO, OPG/OPA*	*Color center lasers*	*Dye lasers*
Tuning range	Very wide, covers the phase matchable transparency region of the material, especially in the IR	Wide, covers the fluorescing region	Narrow, limited in the visible
Inherent bandwidth	Relatively narrow, 1 - 10 nm	Wide, 100nm	Wide, 10's of nm
Threshold energy	High	Low	Low
Operational cost	Low	Low	High
Requirements for narrow bandwidths	Narrow pump laser source	No requirement	No requirement on pump laser
Slope Efficiency	High	Medium	Medium

dreams of using NLO conversions to fabricate widely tunable, coherent light sources. These crystals exhibit exceptional qualities, such as large NLO coefficients, wide transparency regions, and high damage thresholds. The properties of these crystals and their applications will be discussed at length in Chapter 2.

The major tunable devices based on nonlinear optical conversions are those based on optical parametric processes, *e.g.*, optical parametric oscillators, or OPOs, and optical parametric generators (OPGs) and amplifiers (OPAs). In Table 1.1, some of the advantages and disadvantages of traditional tunable laser devices and devices based on optical parametric processes are compared.

It can be seen that optical parametric devices have much wider tuning ranges than do traditional tunable lasers, and their slope efficiencies are also higher than that of other tunable lasers. In addition, optical parametric devices without any linewidth narrowing elements have an inherent bandwidth that already relatively narrow, and that can be used directly in a variety of spectroscopic experiments. This is especially true for devices designed specifically for spectroscopy such as the type II OPO system described in Chapter 3 [38]. The inherent bandwidths of dye lasers and color center lasers are so wide that they are useful only for a limited number of *ns* experiments, but are of great utility in the generation of ultrafast pulses. Traditional dye lasers and

color center lasers do have relatively low threshold energies, however, and therefore put less demand on the damage threshold of the cavity optics and crystals. In this thesis, methods that lower the operational threshold energy for optical parametric devices will therefore be highlighted. Finally, optical parametric devices require a narrow bandwidth pump laser in order to operate at or near the transform limit, while traditional tunable lasers do not.

1.4 Summary

An outline of the remainder of this thesis is as follows. In Chapter 2, the theory and materials that form the foundation of second order nonlinear optical conversions is presented. In Chapter 3, the details of the type II phase matched OPO device is given along with some of the spectroscopic results that have been obtained. Chapter 4 provides the details of a simple, single frequency diode laser seeded OPG/OPA system that gives nearly transform limited bandwidth. The experimental techniques and apparatus used to investigate the spectroscopy of alkali metal-solvent clusters are described in Chapter 5, while Chapter 6 discusses the results of the cluster spectroscopy experiments. Conclusions and directions for future work are given in Chapter 7. Appendices are then included which reproduce the equations ncessary for calculating a variety of phase matching conditions and phase mismatch, along with the programs that perform the computer simulations for the nonlinear optical conversions. Also given are the operational details, such as computer programs, for the ZEKE-PFI experimental apparatus.

Bibliography

[1] J.J. Scherer, J.B. Paul, A. O'Keefe, and R.J. Saykally, *Chemical Reviews*, 97 (1997), 25.

[2] O.M. Cabarcos, C.J. Weinheimer, and J.M. Lisy, *J. Chem. Phys.* , 110 (1999), 8429-8435.

[3] C. Miller, *Science*, 261:1692, 1993.

[4] R.A. Kumpf and D.A. Dougherty, *Science*, 261 (1993), 1708.

[5] J.C. Ma and D.A. Dougherty, *Chem. Rev.*, 97 (1997), 1303.

[6] J.G. Nicholls, A.R. Martin, and B.G. Wallace, *From Neuron to Brain: A Cellular and Molecular Approach to the Function of the Nervous System, Sinauer Associates, Sunderland, MA* (1992).

[7] B. Hille, *Ionic Channels of Excitable Membranes*, Sinauer, Sunderland, MA, 1992.

[8] L. Heginbotham and R. MacKinnon, *Neuron*, 8:483, 1992.

[9] R.A. Kumpf and D.A. Dougherty, *Science*, 261:1708, 1993.

[10] C. Miller, *Science*, 252 (1991), 1092.

[11] W.A. Catterall, *Science*, 242 (1988), 50.

[12] L. Degreve, S.M. Vechi, and C. Quintale, Jr., *Biochim. Biophys. Acta*, 1274:149, 1996.

[13] M.D. Toney, E. Hohenester, S.W. Cowan, and J.N. Jansonius, *Science*, 261:756, 1993.

[14] J.O.M. Bockris and A.K.N. Reddy, *Modern Electrochemistry*, Vol.1, Plenum, New York, 1970.

[15] E. Kálmán and G. Pálinkás in *The Chemical Physics of Solvation*, part B, ed. by R.R. Dogonadze, E. Kálmán, A.A. Kornyshev, and J. Ulstrup, Elsevier, Amsterdam 1988.

[16] W. Rudolph, M.H. Brooker, and C.C. Pye, *J. Phys. Chem.*, 99:3793, 1995.

[17] L. Degreve and C. Quintale, Jr., *Electrochim. Acta*, 38:1405, 1992.

[18] L. Perera and M.L. Berkowitz, *J. Chem. Phys.*, 95:1954, 1991.

[19] M. Migliore, S.L. Fornili, E. Spohr, G. Palinkas, and K. Heinzinger, *Z. Naturforsch*, 41a:826, 1986.

[20] I. Džidić and P. Kebarle, *J. Phys. Chem.*, 74:1466, 1970.

[21] A.W. Castleman, Jr., P.M. Holland, D.M. Lindsay, and K.I. Peterson, *J. Am. Chem. Soc.*, 100:6039, 1978.

[22] C.P. Schulz, R. Haugstätter, H.U. Tittes, and I.V. Hertel, *Phys. Rev. Letters*, 57:1703, 1986.

[23] C. Nitsch, C.P. Schulz, A. Gerber, W. Zimmermann-Edling, and I.V. Hertel, *Z. Physik D*, 22:651, 1992.

[24] C.W. Bauschlicher, Jr., S.R. Langhoff, H. Partridge, J.E. Rice, and A. Komornicki, *J. Chem. Phys.*, 95:5142, 1991.

[25] K. Hashimoto and K. Morokuma, *J. Am. Chem. Soc.*, 116:11436, 1994.

[26] K. Hashimoto and K. Morokuma, *J. Am. Chem. Soc.*, 117:4151, 1995.

[27] J.C. Greer, C. Hüglin, I.V. Hertel, and R. Ahlrichs, *Z. Physik D*, 30:69, 1994.

[28] K. Müller-Dethlefs and E.W. Schlag, *Ann. Rev. Phys. Chem.*, 42:109, 1991.

[29] Y.L. Yung and C.E.Miller, *Science*, 278 (1997), 1778 - 1780.

[30] T. Rahn, H. Zhang, M. Wahlen, G.A. Blake, *GEOP. RES. LETT.*, 25 (1998), 4489-4492.

[31] J.H. Crawford, D.D. Davis, G. Chen, J. Bradshaw, S. Sandholm, Y. Kondo, J. Merrill, S. Liu, E. Browell, G. Gregory, B. Anderson, G. Sachse, J. Barrick, D. Blake, R. Talbot, and R. Pueschel, *J. Geo. Res-Atm.*, 102 (1997)28447-28468.

[32] P.O. Wennberg, R.C. Cohen, N.L. Hazen, L.B. Lapson, N.T. Allen, T.F. Hanisco, J.F. Oliver, N.W. Lanham, J.N. Demusz, and J.G. Anderson, *Rev. Sci. Instrum.*, 65 (1994), 1858-1876.

[33] T. Wagner, U-Platt, Nature, 395 (1998), 486-490

[34] D.A. Rodham and G.A. Blake, *Chem. Phys. Lett.*, 264 (1997), 522-530.

[35] K.H. Wang, D.A. Rodham, G.A. Blake, and V. Mckoy, *J. Chem. Phys.*, 108 (1998), 4817-4827.

[36] R.J. Saykally and G.A. Blake, *Science*, 259:1570, 1993.

[37] J.F. Pinto, L. Esterowitz, and T.J. Carrig, *APPL. OPTICS*, 37 (1998), 1060-1061.

[38] Sheng Wu, Geoffrey A. Blake, Zhaoyang Sun, and Jiwu Lin, *Applied Optics*, 36 (1996), 5898-5901.

Chapter 2 Second Order Nonlinear Optical Conversions

2.1 Basic principles of second order nonlinear optical conversions

2.1.1 Three wave interactions in 2^{nd} order NLO processes

The linear optical response of a material is proportional to the external electromagnetic fields that are incident upon it. Consider two coherent optical waves (with frequencies ν_1 and ν_2) that overlap in a certain material, whose electric fields are given by [1]:

$$\begin{aligned} E_1(t) &= E_1 e^{i\omega_1 t} \\ E_2(t) &= E_2 e^{i\omega_2 t}, \quad , \end{aligned} \tag{2.1}$$

where $\omega_i = 2\pi\nu_i$. The combined field in the overlap region is given by

$$\begin{aligned} E(t) &= E_1(t) + E_2(t) \\ &= E_1 e^{i\omega_1 t} + E_2 e^{i\omega_2 t} \quad . \end{aligned} \tag{2.2}$$

Now, if the material responds quadratically, rather than linearly, to the two incident beams, the response, $S(t)$, in such a material will be given by:

$$\begin{aligned} S(t) &\propto E(t)^2 \\ Re(S(t)) &\propto Re(1/2(E_1^2 + E_2^2) + 1/2[E_1^2\cos(2\omega_1 t) + E_2^2\cos(2\omega_2 t)] + \end{aligned}$$

$$+ \underbrace{E_1 E_2 \cos[(\omega_1 t + \omega_2 t)]}_{SUM-FREQUENCY\ FIELD} + \underbrace{E_1 E_2 \cos[(\omega_1 - \omega_2)t]}_{DIFFERENCE-FREQUENCY\ FIELD} \quad (2.3)$$

The last two terms are new fields oscillating at frequencies equal to the sum of and difference between the two incidental fields — representing the sum and difference between ω_1 and ω_2. For a detailed theory on the physical origin of such second order nonlinearities in materials, the interested reader is referred to the classic textbook by Yariv [2].

In the case when the response $S(t)$ is the dielectric polarization P, we may write in general:

$$P(E) = \kappa(E)E = \kappa_0 E + \chi^{(2)}E^2 + \chi^{(3)}E^3 + ..., \quad (2.4)$$

where κ is the linear dielectric susceptibility (denoted as κ_0 in the absence of the electric field), and $\chi^{(2)}$, $\chi^{(3)}$ and so forth are the nonlinear dielectric susceptibility coefficients (second order or square, third order or cubic, and so on, respectively).

The second order nonlinearity is non-vanishing ($\chi^{(2)} \neq 0$) only in asymmetric materials, *i.e.*, in crystals without a center of symmetry, or at the boundary of isotropic or symmetric materials where the symmetry is broken. In materials with a symmetry center, $\chi^{(2)}, \equiv 0$. In contrast, the third order nonlinear susceptibility is non-zero in all crystal and isotropic materials.

Thus, propagation of two monochromatic waves with frequencies ν_1 and ν_2 in a crystal with a non-zero second order nonlinearity gives rise to two new electromagnetic fields with frequencies that satisfy the conservation of energy, or

$$\omega_{3,4} = \omega_1 \pm \omega_2 \quad , \quad (2.5)$$

as demonstrated by equation (2.3). The sum frequency generation (SFG) component with $\omega_3 = \omega_1 + \omega_2$ provides a method for the conversion of long wavelength radiation, *e.g.*, IR or visible radiation, to short-wave radiation, namely, visible or UV light.

Difference frequency generation (DFG), with $\omega_4 = \omega_1 - \omega_2$, allows one to convert short wavelength radiation to long wavelength radiation. If $\omega_1 = \omega_2$, a special case of sum frequency conversion is obtained, called Second Harmonic Generation (SHG), where $\omega_3 = 2\omega_1$.

The optical parametric process is opposite to that of SFG. Here, two photons with the frequencies $\omega_{1,2}$ are generated from one higher energy photon ω_3. Generation of more complex combination frequencies is also possible with successive SFG stages. For example, Third-Harmonic Generation (THG) can be realized by SHG followed by SFG *i.e.*, $(\omega_3 = 3\omega_1 = \omega_1 + 2\omega_1)$. Fourth-harmonic generation, or 4HG, can be a combination of two SHG processes — $(\omega_4 = 2(2\omega_1))$; or a SFG process involving the third harmonic frequency and the fundamental frequency, *i.e.*, $(\omega_4 = 3\omega_1 + 1\omega_1)$. The latter is sometimes used to extend the so-called phase matching range of a nonlinear crystal (defined below).

When all the input frequencies (ω_1,ω_2), along with their sum and difference frequencies (ω_3,ω_4) lie in the optical region, the processes associated with the generation of new electromagnetic fields are termed second order nonlinear optical conversions. Each of the devices described in this thesis operate in the frequency range from 52600 $cm^{-1}$to 3300 cm^{-1}, or approximately 190 nm to 3 μm, and so can be characterized as nonlinear optical converters.

2.1.2 Phase matching conditions

The previous section describes energy conservation during 2^{nd} order nonlinear optical conversion. Under typical conditions nearly all optical materials are weakly nonlinear, *i.e.*, $\chi^{(2)} \simeq 10^{-8}\kappa_0$, and nonlinear effects can only be observed at measurable levels when light propagates through a fairly long crystal while satisfying the so-called phase-matching conditions [1]. For SFG or DFG, the appropriate condition is:

$$k_3 = k_2 \pm k_1 \tag{2.6}$$

Here, the k_i are the wave vectors corresponding to the electromagnetic fields with frequencies ω_i $(i = 1, 2, 3)$, or

$$\mid k_i \mid = k_i = \frac{2\pi n_i}{\lambda_i} = 2\pi n_i \nu_I \quad , \tag{2.7}$$

where ν_i, n_i and λ_i are the frequency, refractive index and wavelength of the corresponding photons. Along with the energy conservation equation (2.5), equation (2.6) requires that momentum also be conserved.

The relative location of the wave vector under phase matching can either be collinear (where scalar phase matching applies) or noncollinear (where vector phase matching applies). Under collinear phase matching we obtain the conditions for SFG and for parametric oscillation,

$$k_3 = k_2 + k_1, \text{ or } \omega_3 n_3 = \omega_2 n_2 + \omega_1 n_1 \quad . \tag{2.8}$$

For SHG, where $\omega_1 = \omega_2; \omega_3 = 2\omega_1$, the above equation simplifies to

$$k_3 = 2k_1, \text{ or } n_3 = n_1 \tag{2.9}$$

Note that in the optical region, the above equalities (2.9,2.8) for phase matching will never be possible for light waves with the same polarization because of the "normal" dispersion ($n_1 < n_3$) properties for the same polarization inside isotropic materials. The phase-matching conditions can only be met in anisotropic crystals under the influence of differently polarized waves, as is outlined in the following section. Therefore, both a non-zero 2^{nd} order susceptibility and appropriate phase matching geometries are required for efficient 2nd order nonlinear optical conversions.

2.1.3 Phase matching inside nonlinear optical crystals

In a uniaxial crystal a special direction exists called the optic axis (typically labeled the Z axis). The plane containing the Z axis and the wave vector k of the light wave is termed the principle plane. A light beam whose polarization is normal to the

principle plane is called an ordinary ray, or o-ray, while a beam polarized parallel to the principle plane is known as an extraordinary ray, or e-ray. The refractive index of an o-ray does not depend on the propagation direction, while that for the e-ray does. Thus, the refractive index in a nonlinear optical crystal generally depends both on the light polarization and propagation direction. The difference between the refractive indices of the o-ray and e-ray is known as birefringence, Δn. The Δn is equal to zero along the optic axis Z, and reaches a maximum in the direction normal to this axis. In the plane normal to the Z-axis, the refractive indices of the o-ray and the e-ray are termed the principle values of the refractive index, and are labeled by n_o and n_e, respectively. The refractive index of the e-ray depends on the polar angle θ between the Z axis and the vector k. It is determined by the equation:

$$n^e(\theta) = n_o \sqrt{\frac{1 + \tan^2\theta}{1 + (n_o/n_e)^2 \tan^2\theta}} \tag{2.10}$$

Here, the superscript "e" in "$n^e(\theta)$" denotes the changing refractive index for the e-ray. The following relations then follow immediately:

$$\begin{aligned} n^o(\theta) &\equiv n_o \\ n^e(\theta = 0) &= n_o \\ n^e(\theta = \pi/2) &= n_e \\ \Delta n(\theta = 0) &= 0 \\ \Delta n(\theta = \pi/2) &= n_e - n_o \\ \Delta n(\theta) &= n^e(\theta) - n_o \end{aligned}$$

If $n_o > n_e$, the crystal is called a negative crystal; while if $n_o < n_e$ the crystal is termed positive. Crystals like β-barium borate (BBO) and $LiNbO_3$ are negative uniaxial crystals. The dependence of the refractive index on the light propagation direction inside the crystal is a combination of a sphere with radius n_o (for the o-ray) and an ellipsoid of rotation with semi-axes n_o and n_e.

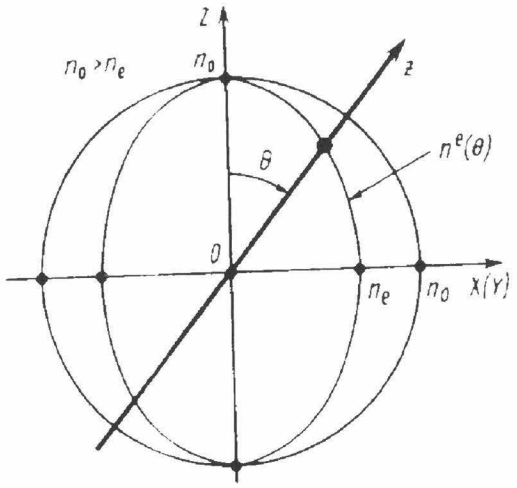

Figure 2.1: Index sphere in a negative uniaxial crystal. If at a certain angle $n^e(\theta) = n_o$, the type I phase matching condition is fulfilled for SHG.

In the Z-axis direction the sphere and ellipsoid are in contact with each other. By changing the value of θ, the phase matching condition is fulfilled (Figure 2.1) if it is possible to find an angle at which

$$\Delta n(\theta) = n^e(\theta) - n_o = 0 \quad . \tag{2.11}$$

In biaxial crystals, the refractive index sphere will be a 3-dimensional structure which not only involves the change of θ, but also the angle ϕ. Thus, phase matching in biaxial crystals is much more complicated than that in uniaxial crystals. The principle, however, remains the same – only with different polarizations can the three light wave phase matching be obtained in a birefringent crystal. Readers interested in further details are urged to consult reference [3].

The polarization combinations of the phase matching process permit the types of phase matching that are possible in NLO crystals to be classified. In negative crystals, if the three waves follow the relationship:

$$k_{o1} + k_{o2} = k_3^e, \tag{2.12}$$

then this combination is "ooe" phase matched or type I phase matched. In a positive crystal, the appropriate combination is "eeo," and it is still called type I phase matching. The generally accepted convention, and that adopted in this thesis, is: The first two symbols in the expression "ooe" or "eeo" refer to the waves with lower frequencies. Further, the first wave has a frequency lower or equal to that of the second, and the third symbol refers to the wave with the highest frequency. If the first two lower frequency waves have the same polarization, then the phase matching is refered to as a type I process. Alternatively, if the last two waves have the same polarization, the phase matching is of the type II variety. Finally, if the last two waves have the opposite polarization, then it is called type III phase matching. This convention applies not only to uniaxial crystals but to biaxial crystals as well.

To satisfy the phase matching conditions according to equation (2.11), one must calculate the phase matching angle θ_{pm} or ϕ_{pm}. Tables 1 and 2 in Appendix A, adapted from [3], list all the formulas needed to calculate the phase matching angle for different phase matching types and crystals. The phase matching angle can also be calculated with the Lagrange formula, which can be applied to any kind of phase matching combination, as is also described in the Appendix.

When an e-ray enters a crystal, the direction of the propagation of its wave vector k generally does not coincide with that of the energy flow vector s. The angle between s and k is called the "walk-off" angle ρ:

$$\rho(\theta) = \pm \arctan[(n_o/n_e)^2 \tan\theta] \mp \theta \tag{2.13}$$

The upper signs refer to a negative crystal, and the lower signs refer to a positive crystal. This walk-off effect will limit the effective interaction length of the three waves in nonlinear optical conversion, especially when the size of the laser beam is very small, and therefore should be eliminated whenever possible (see Chapter 3 for details).

2.2 Efficiency of NLO conversions

2.2.1 Basic differential equations for NLO conversions

Based on the electromagnetic field Maxwell equation inside a crystalline material,

$$\nabla^2 E(r,t) + \frac{\varepsilon_0}{c^2}\frac{\partial^2 E(r,t)}{\partial t^2} = -\frac{4\pi}{c^2}\frac{\partial^2 P_{NL}(r,t)}{\partial t^2}, \tag{2.14}$$

where equation (2.4) has been used for the 2^{nd} order nonlinear polarization

$$P_{NL}(r,t) = \chi^{(2)} E^2(r,t) \tag{2.15}$$

and the boundary conditions for the electric field $E(r,t)$, we have:

$$E(r,t) = \frac{1}{2}\sum_{n=1}^{3}(p_n A_n(r,t)\exp[i(\omega_n t - k_n r)] + C.C.) \tag{2.16}$$

In the above, the $A_n(r,t)$ are the complex wave amplitudes, ω_n and k_n are the frequencies and wave vectors, respectively; and C.C means "complex conjugate." From these three equations, the expressions

$$M_1 A_1 = i\sigma_1 A_3 A_2^* \exp(i\Delta k z) \tag{2.17}$$

$$M_2 A_2 = i\sigma_2 A_3 A_1^* \exp(i\Delta k z) \tag{2.18}$$

$$M_3 A_3 = i\sigma_3 A_1 A_2 \exp(-i\Delta k z) \tag{2.19}$$

and

$$M_n = \frac{\partial}{\partial z} + \rho\frac{\partial}{\partial x} + \frac{i}{2k_n}\left(\frac{\partial^2}{\partial x^2} + \frac{\partial^2}{\partial y^2}\right) + u_n^{-1}\frac{\partial}{\partial t} + ig_n\frac{\partial^2}{\partial t^2} + \alpha_n + Q_n(A) \tag{2.20}$$

may be derived, with

$$\sigma_i = \frac{\omega_i d_{eff}}{n_i c} \quad . \tag{2.21}$$

Here, the u_n are the group velocities, the g_n are the dispersive spreading coefficients, Δk is the total phase mismatch, the α_n are the linear absorption coefficients, the Q_n are the 2^{nd} order nonlinear absorption coefficients, n_i is the refractive index of the corresponding wave, d_{eff} is the effective nonlinear optical coefficient, and c is the speed of light.

In this thesis, we will be dealing with nano-second (ns) pulses, so the group velocity and dispersion variations are negligible and can be ignored. Hence, the factors that ultimately decide the final efficiency will be the phase mismatch Δk and optical absorption from both linear absorption, α_n, and 2-photon nonlinear absorption, Q_n.

Due to the complexity of the differential equations (2.17), (2.18) and (2.19), and the nonlinear nature of the interactions involved, it is impossible to solve them analytically. Therefore, numerical simulations are carried out. The appendix to this thesis describes a computer program which uses the Runge-Kutta step method to solve the above equations numerically. For each of the devices presented herein, the program can be modified to carry out the theoretical simulations, the results of which will be presented in later chapters.

2.2.2 Angular, spectral and temperature phase mismatch

In equations (2.17), (2.18) and (2.19), the Δk is the total phase mismatch and consists of

$$\Delta k = \Delta k_L + \Delta k_{pr} + \Delta k_{fcg} \quad , \tag{2.22}$$

where Δk_L is the linear phase mismatch, or

$$\Delta k_L = k_1 + k_2 - k_3 \quad . \tag{2.23}$$

Δk_{fcg} is the mismatch due to free-carrier generation in the conduction band of the crystal due to nonlinear absorption, and Δk_{pr} is the phase mismatch imposed by photorefractive effect inside the nonlinear optical crystal. The Δk_{fcg} and Δk_{pr} terms are not important to this thesis since we are dealing mainly with BBO crystals and

ns laser pulses. BBO crystals, unlike ferrite crystal such as $LiNbO_3$ and KTP (Potassium Titanyl Phosphate), have a small photorefractive effect. In addition, the deep UV peak power inside BBO crystals is not very high, and so the main effects that must be considered are those of the angular bandwidths, spectral, and temperature bandwidths.

In real nonlinear optical conversions, the situation is far from ideal. The input laser radiation is divergent, pulsed, and of finite spectral bandwidth. There is also absorption inside the crystal, both from the input and converted light waves, that results in a temperature variation inside the crystal. In practice, therefore, the following parameters of various nonlinear optical converters — the angular, spectral, and temperature bandwidths corresponding to maximum permissible divergence, the spectral width of the input radiation, and the temperature instability inside the specific crystal material - must be calculated.

The value Δk_L can also be rewritten as a function of crystal temperature T, the frequencies of the interacting waves ν_n, and the deviation from the phase matching angle $\delta\theta = \theta - \theta_{pm}$, as may be simply understood because as these three factors change, $k_1 + k_2 - k_3$ will change as well. The dependence of Δk (here we drop the subscript "$_L$" for simplicity) on these parameters, to first order, can be approximated by the first terms in the Taylor series expansion:

$$\Delta k(T, \delta\theta, \nu) \simeq \frac{\partial(\Delta k)}{\partial T}\Delta T + \frac{\partial(\Delta k)}{\partial \delta(\theta)}\Delta\theta + \frac{\partial(\Delta k)}{\partial \nu}\Delta\nu \quad . \tag{2.24}$$

It has been demonstrated that the power of a converted light wave in the fixed-field approximation is halved if the phase mismatch is equal to

$$\Delta k = 0.886\frac{\pi}{L} \quad , \tag{2.25}$$

where L is the interaction length. Based on equation (2.25), the angular ($\Delta\theta$), temperature (ΔT), and spectral ($\Delta\nu$) bandwidths can be expressed as

$$\Delta\theta \;=\; 1.772\frac{\pi}{L}[\frac{\partial(\Delta k)}{\partial(\delta\theta)}]^{-1}_{\theta=\theta_{pm}} \tag{2.26}$$

$$\Delta T = 1.772\frac{\pi}{L}[\frac{\partial(\Delta k)}{\partial T}]^{-1}_{T=T_{pm}} \tag{2.27}$$

$$\Delta \nu = 1.772\frac{\pi}{L}[\frac{\partial(\Delta k)}{\partial \nu}]^{-1}_{\nu=\nu_{pm}} \quad . \tag{2.28}$$

The derivation of these equations depends on the dispersion of the refractive indices and on the type of phase matching. The equations for calculating the internal angular, spectral and temperature bandwidths are listed in Appendix A.

It is worth mentioning that when the phase matching is achieved for both θ_{pm} and ϕ_{pm} equal to zero or 90 degrees, a special type of phase matching, called non-critical phase matching, or NCPM, is obtained. Here, the crystal has the largest angular bandwidth. In addition, the "walk-off" effect is eliminated, and NCPM is therefore widely used in SHG of continuous wave laser source where tight focusing is required. The tuning range of NCPM phase matching can be extended somewhat by temperature tuning.

Another important point to consider is that the angular and spectral acceptance bandwidth given in Appendix A can only be applied along the so-called sensitive direction, that is, the direction of the e-ray's polarization. For example, in a negative uniaxial crystal such as BBO used in a type I phase matching fashion (ooe, $\omega_1 + \omega_2 = \omega_3$), the acceptance angle in the θ direction is only about 1 mrad or less, while the acceptance angle in the ϕ direction is typically 50 times larger. This is illustrated in Figure 2.2. The relationship between the acceptance angle in the θ and ϕ direction is given by

$$l = \sqrt{\rho^2 \tan^2(\theta_{pm} + \Delta\theta) - \rho^2 \tan^2 \theta_{pm}} \tag{2.29}$$

and

$$\Delta\phi = \frac{l}{\rho/\cos\theta_{pm}} \quad . \tag{2.30}$$

Thus,

$$\Delta\phi = \cos\theta_{pm}\sqrt{\tan^2(\theta_{pm} + \Delta\theta) - \tan^2\theta_{pm}} \simeq \sqrt{2\tan\theta_{pm}\Delta\theta} \tag{2.31}$$

Numerically, for the type I BBO OPO process, the acceptance angle is only about 0.5 mrad in the sensitive (θ) direction at a phase matching angle of 30°, but in the

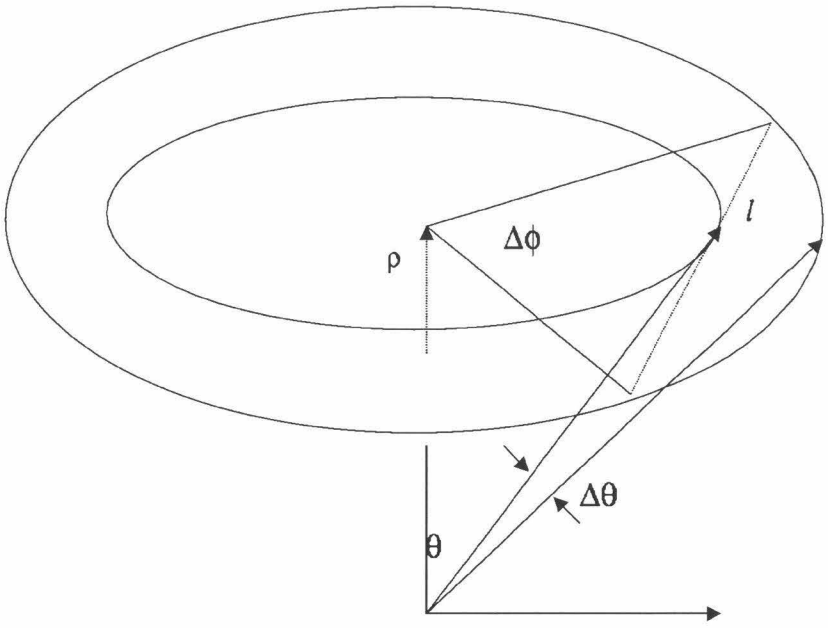

Figure 2.2: An illustration of the differing acceptance angles in the θ and ϕ directions.

insensitive (ϕ) direction the acceptance angle is 24 mrad. An important application of this difference in acceptance angles is the use of cylindrical focusing in the conversion systems described in Chapters 3 in order to increase the intensity while at the same time keeping the divergence smaller than the acceptance angle in both directions. This is applied to both SHG [28] and OPO processes [35].

The characteristic value of Δk from equation (2.25) is based on what is termed the fixed-field approximation, that is under the assumption that the input wave depletion and phase mismatch variation is negligible during the NLO conversion. This is true for processes in which the energy exchange of the three waves is sufficiently small. Obviously, this approximation is not true for processes with very high conversion efficiency or in cases where high absorption exists. For numerical simulations, however, it is still possible to use this approximation since during the simulation the crystal is divided into infinitesimally small units, in which the exchange of energy among these three waves can be made correspondingly small. The signal that the unit cell is small enough is that the resulting efficiency from the simulation does not change as the unit size is reduced further. Numerical simulations based on this approximation can be easily extended to include anisotropic phase mismatches such as the thermal distribution inside the crystal material [4], and is used later in this thesis to provide insight into high average power deep UV generation in absorbing nonlinear materials.

2.3 Nonlinear optical crystals

There have been many powerful nonlinear optical crystals discovered since the invention of the laser. In this section, some of the most important nonlinear optical crystals are reviewed, including a qualitative description of the very latest results. For a more detailed quantitative description, interested readers should consult reference [3] and the many specific papers cited therein that describe the properties of individual crystals.

2.3.1 Most often used nonlinear optical crystals

As early as 1961, Franken *et al.* [6] observed radiation at the doubled frequency when a ruby laser beam was directed into a quartz crystal. Because the phase matching is not fulfilled in quartz, the conversion efficiency to the second harmonic was very low (10^{-12}). After theory of phase matching in birefringent crystals was proposed, however, there was rapid development of nonlinear optical conversion schemes and the crystal materials used in these applications.

ADP (Ammonium Dihydrogen Phosphaste) and KDP (Potassium Dihydrogen Phosphate) were the first crystals used for robust nonlinear frequency conversion [7]. These two crystals, along with their derivative KD*P (Deuterated Potassium Dihydrogen Phosphate), are very easy to grow but have relatively low damage threshold, small 2^{nd} order nonlinear coefficients, small birefrigence, small temperature bandwidths, and a limited region of high optical transparency. The small birefregence puts a limit on the nonlinear optical crystals' phase matching capability as is outlined by the phase matching theory described in Section 2.1.3. Today, these crystals are still in wide use because of their low cost and large crystal size. For example, the National Ignition Facility at Sandia National Lab still uses KD*P in sizes as large as 250 mm to generate high power harmonics of the 1064 nm Nd:YAG fundamental [19]. Many powerful Nd:YAG lasers still use KDP and KD*P in their harmonic generators, although the small temperature bandwidth of KDP/KD*P requires a temperature stablized crystal oven for maximum conversion efficiency.

$LiNbO_3$ [9] and $LiIO_3$ [10] were invented in the 1960's and have pioneered difference frequency generation and optical parametric processes in the near IR region [11, 12]. These two crystals suffer, however, from low damage threshold and poor transmission in the visible and UV. The $KNbO_3$ derivative of $LiNbO_3$ is another very important NLO crystal, especially since it can be temperature tuned to fulfill the SHG phase matching condition in the 850 - 950 nm range in order to generate blue wavelengths from high efficiency near-IR diode lasers [13, 14]. Today, most of the all solid state diode pumped lasers use $KNbO_3$ as their SHG material. $KNbO_3$ is quite difficult to

grow and fabricate, it so it is now giving way to Periodically Poled $LiNbO_3$ (PPLN).

KTP (Potassium Titanyl Phosphate) [15] is a critical nonlinear optical crystal invented in 1976. It is easy to grow, and has low absorption in the 1064 nm and 532 nm region. This is the crystal of choice for 1064 $\rightarrow$ 532 nm SHG. It is also a better crystal than $LiNbO_3$ in the near IR region for DFG and OPO conversions [16] due to its higher damage threshold. The arsenate derivative, KTA (Potassium Titanyl Arsenate), has generated considerable recent enthusiasm because it has much better IR transmission in the chemically important 3 - 5 μm region [17], and so KTA should be a very good candidate for parametric interactions in this region.

The discovery of nonlinear optical materials is, at present, a slow and painstaking process, with much research having been focused on the phosphate crystals (KDP, ADP and KTP). The borate crystal family did not receive much attention because there was an error made in the 1930's on the structural properties of β -BaB_2O_4 (BBO). This crystal was determined to have a center of symmetry and therefore would be impossible for use in 2^{nd} order nonlinear optical applications. Liang *et al.* pointed out this mistake in the early 1980's [18] and proposed that BBO would be a very promising nonlinear optical crystal. BBO as a nonlinear optical crystal material was confirmed in 1985 [19], and has received great attention as the crystal growing technology improves.

BBO has a relatively large birefrigence and therefore is phase matchable from 409.6 nm to 3500 nm for SHG, and from 189 nm to 3500 nm for SFG. It has wide transmission region from 190nm to 3500nm and has a high damage threshold compared to KTP and $LiNbO_3$. Its nonlinear optical coefficient is also several times larger than that of KDP for harmonic generation at UV wavelengths. These favorable properties allowed allowed BBO to be the first commercially available crystal that can be used in a UV pumped OPO device to generate tunable laser radiation from the UV to the near IR [2, 21]. The devices described in this thesis are based on BBO crystals. Recent progress in the crystal growth techniques for BBO has begun to optimize the Czochralski, or pulling, method [22]. This method is almost 100 times faster than the current flux-grown method and the quality is expected to be better, and so its

widespread use should greatly reduce the cost of BBO crystals, making it a powerful yet affordable NLO material.

The LBO (LiB_3O_5) nonlinear optical crystal was invented in 1989 [23]. LBO has even higher damage threshold than BBO, and has the unique property that it does not show a photorefractive effect, unlike other types of NLO materials. Although its nonlinear coefficient is smaller than in BBO, it is NCPM phase matchable at an elevated temperature (152° C) for SHG of 1064 nm. Therefore, it has become the workhorse for high power, long term generation of 532 nm radiation (see, for example, the Millenia solid state green laser from Spectra-Physics).

Soon after the discovery of BBO and LBO, Cheng *et al.* [26] proposed a theory on the structure of the borate NLO crystals, which led to the discovery of many new borate nonlinear optical materials with exceptional merits, such as CLBO ($CsLiB_6O_10$), CBO (CsB_3O_5), SBBO ($Sr_2Be_2B_2O_7$) and KBBF (KBe_2BO_3F) were discovered. SBBO, for example, has the potential to generate VUV radiation down to wavelengths as short as 170 nm directly by SHG.

The CLBO ($CsLiB_6O_10$) crystal is the newest member in the borate nonlinear optical crystal family [24]. It has a damage threshold even higher than that of BBO. Although it has smaller nonlinear optical coefficients, it does have much larger angular, spectral and temperature acceptance bandwidths and a much smaller walk-off effect than BBO. Since absorption starts to reduce the performance of SHG or SFG at UV wavelengths, the larger acceptance bandwidths and smaller walk-off effect in CLBO allow for much higher conversion efficiency at high input power. A detailed comparison of BBO, KTP and CLBO crystal for the SHG and SFG processes is given in Chapter 4. CLBO is therefore a promising crystal for harmonic generation of deep UV radiation, but is presently hampered by its unstable crystal structure, which leads to an unpredictable natural life time [25].

In the longer wavelength IR region (2 - 10 μm), two crystals, $AgGaS_2$ [27] and $ZnGeP_2$ have recently attracted much attention. Because of the improved quality and transmission in this region for $ZnGeP_2$ crystals [28], for example, they are now promising crystals for high efficiency, high power NLO conversion in this pivotal

region. Possible integrated optical/IR schemes will be discussed at the end of this thesis.

Another recent development is that of periodically poled materials, *e.g.*, periodically poled $LiNbO_3$ (PPLN) or KTP crystals. This technology [12] applies a spatially periodic strong electric field onto ferroelectric crystals such as $LiNbO_3$ and KTP, which changes the dipole orientation inside the crystal, thereby effectively changing the sign of the crystal's nonlinear optical coefficient. By changing the period of the spatial electric field, the phase matching conditions can be achieved throughout the optical transparency region of the material using the largest NLO coefficient with no walk-off losses. This technology enables many nonlinear optical conversions that were difficult to achieve previously, *e.g.*, efficient SHG of CW laser without external cavity enhancement [31], a singly resonant OPO pumped by a CW laser source [30], and a *ns* OPO pumped by low pulse energy lasers [32]. Periodically poled materials are currently limited by their small size. Commercially available PPLN crystals, for example, have apertures of only 0.5 mm in height, and therefore cannot handle very high pump powers. With improvements in the electric poling the aperture size is being enlarged. Recently, periodically poled RTA (Rubidium Titanyl Arsenate) wafers as large as 4×4×20 mm have been successfully fabricated [37].

2.3.2 Damage thresholds of nonlinear optical crystals

One critical figure of merit of a nonlinear optical crystal is its damage threshold. There is much ambiguity in the definition and measurement of the damage threshold of nonlinear optical crystals. The sources of the ambiguity include, but are not limited to:

- The damage can arise at the surface or in the bulk material. The bulk damage threshold is considered as the "true" damage threshold of the material, since surface damage threshold is expected to be much lower than the bulk damage threshold due to the disruption of the crystal structure at the surface and the introduction of impurities during the optical grinding of the surface(s). Some

crystals, *e.g.*, KDP and BBO are slightly hygroscopic, and so the surface damage threshold will be much lower if the uncoated crystal is left in the air for a long period of time. Thus, crystals can easily become damaged at their surfaces, and this damage grows quickly under intense laser radiation. The damage growth rate also varies from crystal to crystal.

It is this author's experience that KTP and $LiNbO_3$ crystal surface damage can easily transfer to the bulk material. In contrast, BBO crystal surface damage usually begins on the coating and its growth rate is rather slow. This property is related to the crystal structure of the NLO materials. Therefore, in order to preserve the value of the nonlinear optical crystal it is essential to stop the laser operation once optical damage is observed at the surface, especially for $LiNbO_3$ and KTP. The bulk damage is usually related to any impurities, *e.g.*, tiny inclusions and inhomogeneities, inside the crystal. This damage mainly depends on the crystal's production quality, and indeed varies with production runs among different crystal suppliers.

- The optical damage threshold is a wavelength dependent quantity. Very often it is difficult to test the damage thresholds at all wavelengths of interest. For nonlinear crystals used in the UV, visible and near IR, the damage threshold decreases as the wavelength gets shorter and shorter. This is because as the photon energy increases, so to does the two photon absorption cross section increase [33]. For example, BBO's transparency region ends at 189 nm (50% loss/cm), and it is therefore reasonable to expect the band gap of the BBO crystal to be equal to the photon energy of 189 nm [23]. The damage threshold of a BBO crystal thus decreases much faster in the UV, especially below 400nm. Also, the shorter UV wavelength results in stronger scattering around tiny inclusions and inhomogeneities.

- For pulsed lasers, the optical damage threshold strongly depends on the pulse width. It is a function of both the energy density (mJ/cm^2) and power density (MW/cm^2). The damage threshold in terms of power density increases as pulse

width get shorter. There is no strict formula to describe this relationship. Generally, the magnitude of damage threshold increase is much less than the magnitude of pulse width reduction.

2.4 Pump lasers

Efficient nonlinear optical conversion requires not only novel nonlinear optical crystals but also high quality pump lasers. In this thesis, the emphasis is on nanosend (ns) processes, and therefore only ns pump lasers are discussed here.

Before 1985, all commercially available high power pulsed Nd:YAG lasers used unstable resonator cavities in order to generate the highest possible pulse energies. Unstable cavities can utilize the largest possible volume of the gain media, usually a Nd:YAG rod, because the beam waist is not located inside the resonant cavity. However, diffraction effects are unavoidable consequences of unstable cavity design, and all of the earliest Nd:YAG lasers, such as the DCR series from Spectra-Physics, possess intense diffraction patterns in their beam profiles. Since the nonlinear optical conversion depends quadratically on the fundamental input power, the diffraction pattern is much stronger at the harmonics of the Nd:YAG laser's fundamental output. Pump lasers with this kind of diffraction pattern are especially bad for nonlinear optial conversions. Because the energy distribution is not homogeneous inside the laser beam, there can exist hot spots with intensities that are orders of magnitude above the average. This results in damage of optics and crystals used for nonlinear optical conversions – especially for visible OPOs because the short UV pumping wavelengths are typically involved where the damage threshold is low. To overcome this problem, one solution is to propagate the laser beam a long distance before directing it into the OPO cavity. After the long optical path, the high diffraction orders are removed from the laser beam — making the laser beam profile much smoother. This technique, although simple, leads to two disadvantages:

- The energy loss during this long optical path can be large, usually over 50% of the energy is lost due to diffraction after 3 meters of propagation.

- The pointing stability of these lasers were typically poor, and propagation over a long optical path causes large laser beam position changes that makes stable operation very difficult.

- When the laser deviates from perfect alignment, there is small phase disorder in the laser beam as it exits the laser, even though the laser beam profile looks normal. As the propagation path gets longer, the phase disorder will form hot spots which damage subsequent optics and crystals.

To eliminate the diffraction pattern, instead of using an appodized output coupler in the Nd:YAG laser, an output coupler with rapid varying reflectivity (RVR or "Guassian coupler") is now used. The RVR mirror can correct the diffraction pattern by tailoring the radial reflectivity appropriately. Early RVR mirrors were not very good, and residual diffraction patterns remained, especially in the harmonics. The latest RVR mirrors can be almost perfectly matched a to laser's output characteristics at the fundamental wavelength, and smooth beam profiles, even those close to a step function, or "flat top," can be generated at the fundamental and higher harmonics. Present lasers still suffer from thermal loading inside the Nd:YAG laser rod, which is especially severe at higher pulse repetition rates, and phase variations across the beam profile.

More recently, phase conjugate mirror technology has been introduced commerically. This coupled with thermal compensation enables the amplification of small pulse energy laser beams with exceptionally good beam profiles, leading to high quality laser beams at high repetition rates and high pulse energies. Such lasers should provide very stable output energies and beam profiles over a long period of time. There are also a number of other factors that must be considered for the pump laser in various OPO/OPG/OPA processes, and these will be discussed at greater length in Chapters 3 and 4.

For experiments with *ns* pulses, high repetition rate ($>$ 1kHz), high average power (multi-watt) with low pulse energy (mJ/pulse) lasers are sometimes needed or desirable. Lasers with these properties have dramatically improved their performance and

reduced their size due to diode pumping technology[38]. Diode pumping provides energy to the laser gain media with much better efficiency than that available with flash lamp pumping. Therefore, the thermal load in the gain media is reduced, making cooling processes correspondingly more efficient. The diode pumping also reduces the operating costs of these lasers. Diode-pumped lasers have high average power, but low pulse energy and therefore low peak power. In order to drive efficient nonlinear optical conversion, focusing is required. Focused beams usually have a divergence much larger than the acceptance angle of a NLO crystal, and the volume at the focal point is very small. Then, this focusing put acceptance angle problem and thermal load problem on the nonlinear optical devices. In Chapters 3 and 4, OPO and SHG processes with diode-pumped lasers are explored, paying close attention to the large difference in acceptance angles in the two orthogonal directions in order to address the thermal loading and acceptance angle problems.

2.5 Conclusion

In this chapter, we explored the basic equations for energy conversion and phase matching conditions in a nonlinear optical crystal. Computer modeling software has been designed based on the theory outlined herein, and is presented in Appendix A. A survey of the lastest developments in NLO crystals and some of their interesting properties in ns pulsed laser operation were discussed.

Bibliography

[1] A. Yariv, *Quantum Electronics*, 3rd ed., New York, John Wiley & Sons, 1989.

[2] A. Yariv, *Optical Electronics*, 4th ed., New York, Saunders College Publishing, 1991.

[3] V.G. Dimitriev, G.G. Gurzadyan, and D.N. Nikogosyan, *Handbook of Nonlinear Optical Crystals*, 2nd ed., New York, Springer, 1991.

[4] Sheng Wu, Geoffrey A. Blake, Sunny Sun and John Lin, *to be submitted*

[5] Rodney I. Trickett, Michael J. Withford, and Daniel J. W. Brown *Opt. Lett.*, 23 (1998), 189-191

[6] P.A. Franken, A.E. Hill, C.W. Peters, and G.Weinreich, *Phys. Rev.Lett.*, 7 (1961), 118-119

[7] F. Jona and G.Shirane, *Ferroelectric Crystals.*, Oxford Pergamon, 1962

[8] David Eimerl *Journal of Quantum Electronics*, 23 (1987), 575.

[9] R.C. Miller *Appl. Phys. Lett.*, 5 (1964), 17-19.

[10] G. Nath and S. Haussahl *Appl. Phys. Lett.*, 14 (1969), 154-156.

[11] T.K. Minton, S.A. Reid, H.L.Kim, and J.D. McDonald, *Optics Communications*, 69 (1989), 289-293.

[12] Y.B. Cao, "Vibrational predissociation spectroscopy of mass-selected ionic clusters." *CIT PhD thesis* (1994).

[13] J.C. Baumert, P. Günter, and H. Melchior, *Optics Communications*, 48 (1983), 215-220.

[14] P. Günter, *Appl. Phys. Lett.*, 34 (1979), 650-652.

[15] F.C. Zumsteg, J.D. Bierlein, and T.E. Gier, *J. Appl. Phys.*, 47 (1976), 4980-4985.

[16] W.R. Bosenberg and D. R. Guyer, *J. Opt. Soc. Am. B* 10 (1993), 1716-1722.

[17] A.H. Kung, S.L. Fei, and H.L. Strauss, *Appl. Spectroscopy* 50 (1996), 790-794.

[18] J.K. Liang, Y.L. Zhang, and Q.Z. Huang, *Acta Chimica Sinica*, 40 (1982), 994-1000.

[19] C. Chen, B. Wu, A. Jiang, and G. You, *Sientia Sinica, Ser. B*, 28 (1983), 235-243.

[20] B.C. Johnson, V.J. Newell, J.B. Clark and E.S. McPhee, *J. Opt. Soc. Am. B*, 12 (1995), 2122-2127.

[21] Sheng Wu, Geoffrey A. Blake, Zhaoyang Sun, and Jiwu Lin, *Applied Optics*, 36 (1996), 5898-5901.

[22] H. Kouta and Y. Kuwano, *Appl. Optics*, 38 (1999), 1053-1057.

[23] C. Chen, Y. Wu, A. Jiang, B. Wu, G. You, R. Li, and S. Lin, *J. Opt. Soc. Am. B*, 6 (1989), 616-621.

[24] Y. Mori, T. Kuroda, S. Nakajima, T. Sasaki, and S. Nakai, *Appl. Phys. Lett.*, 67 (1995), 1818-1820.

[25] Yoshimura M, Kamimura T, Murase K, Mori Y, Yoshida H, Nakatsuka M, and Sasaki T, *Jpn. J. Appl. Phys.*, 38(2A), (1999), L129-L131.

[26] C.T. Chen, Y.B. Wang, B.C. Wu, K.C. Wu, W.L. Zeng, and L.H. Yu, *Nature*, 373:(6512), (1995), 322-324.

[27] V.V. Badikov, V.S. Solomatin, N.I. Cherepov, V.V. Shuvalov, V.V. Badikov, and O.N.Pivovarov, *So. J. Quantum Electron.*, 5 (1975), 597-598.

[28] Peter Schuneman, *Laser Focus World* 35 (1999), 85-90.

[29] W.R. Bosenberg, A Drobshoff, J.I. Alexander, L.E. Myers, and R.L. Byer, *J. Opt. Soc. Am. B*, 12 (1995), 2102-2116.

[30] W.R. Bosenberg, A Drobshoff, J.I. Alexander, L.E. Myers, and R.L. Byer, *Opt. Lett.*, 21 (1996), 1336-1338.

[31] D.H. Jundt, G.A. Magel, M.M. Fejer, and R.L. Byer, *Appl. Phys. Lett.*, 59 (1991), 2657-2659.

[32] L.E. Myers and W.R. Bosenberg, *IEEE J. Quan. Elec.*, 33 (1997), 1663-1672.

[33] H Kouta, *Appl. Optics*, 38 (1998), 545-547.

[34] R. DeSalvo, A.A. Said, D.J. Hagan, E.W. Van Stryland, and M. Sheik-Bahae, *IEEE. J. Quan. Elec.*, 32 (1996), 1324-1333.

[35] S. Wu and G.A. Blake, "Low-threshold BBO OPO with cylindrical focusing" Proc. SPIE, No. 17, 3263 (1997).

[36] Rodney I. Trickett, Michael J. Withford, and Daniel J. W. Brown, *Opt. Lett.*, 23 (1998), 189-191.

[37] Private communication with Dale Reitcher at ITT Industry.

[38] C. Frederickson, M. Keirstead, and M. Watts, *Laser Foc. World*, 35 (1999), 127.

Chapter 3 A simple 355 nm-pumped type II BBO OPO with broad tuning range

3.1 Theory of ns OPOs

Optical parametric oscillators are powerful solid-state laser sources with potentially very large continuous tuning ranges. For example, OPOs based on BBO can be continuously tuned from 410 nm to 2.5 μm with a single set of mirrors when they are pumped at 355 nm [1] [2] [3], or from 310 nm to 2.5 μm when pumped at 266 nm [4],[5]. 532 nm pumping of OPOs based on KTP and KTA crystals can cover the range from 620 nm to 4 μm[6]. With proper pump lasers, crystal materials, and optics, the conversion efficiency of such pulsed OPOs can be as high as 70%. The basic theory of the parametric process was known long before the invention of practical OPO devices. There was considerable interest in the microwave parametric amplifier in the 1950's [9], for example, while first theoretical analysis of an OPO was put forward by Kroll in 1962[7]. Shortly after the first demonstration of the OPO process by Giordmaine ad Miller in 1965 [8], there was tremendous hope that a robust, widely tunable OPO light source was well within reach. The experimental development of such devices was hampered primarily by the lack of suitable nonlinear optical crystals, and secondly by the availability of good pump lasers. In the 1970's and 1980's, KTP and several new borate crystals were discovered, especially BBO, and these discoveries have had a great impact on the development of UV pumped OPOs that can be tuned from the UV to the near IR region.

Optical parametric oscillation is a NLO process in which an input pump photon propagating in a nonlinear optical material is converted into two lower-energy pho-

tons. The energy conservation and phase matching conditions described in Chapter 2 are thus applicable to OPOs. Next, the operational threshold, efficiency, beam characteristics, and bandwidth of OPO cavities will be examined.

3.1.1 Operational threshold and efficiency of *ns* OPOs

The simplesst OPO consists of a plane-parrallel two mirror cavity. While such a plane-parallel cavity is unstable, the gain profile generated by the pump beam quickly confines the resonant wave and stabilizes the cavity mode.

When a *ns* OPO lies near threshold, it is safe to assume no pump depletion occurs and to invoke a slowly varying optical power envelope (so that time can be disregarded). Other effects such as two photon absorption and two dimensional pump beam inhomogeneity can also be ignored, and in this limit equations (2.17), (2.18), and (2.19) can be simplified to yield:

$$\frac{\partial A_s}{\partial z} + \delta_s A_s = i\sigma_s A_p A_i^* \exp(i\Delta K z), \tag{3.1}$$

$$\frac{\partial A_s}{\partial z} + \delta_i A_i = i\sigma_i A_p A_s^* \exp(i\Delta K z). \tag{3.2}$$

Here, the subscript p, s and i denote the pump, signal, and idler waves. If the idler field is assumed to be zero at the entrance to the crystal, the signal field at the end of a crystal of length l is given by

$$A_s(l) = A_s(0) \exp^{-\alpha l} \cosh \Gamma L \quad , \tag{3.3}$$

where

$$\Gamma = \sqrt{\sigma_s \sigma_i g_s |A_p|^2} \tag{3.4}$$

is the parametric gain coefficient, and

$$g_s = \frac{w_p^2}{w_p^2 + w_s^2} \quad , \tag{3.5}$$

where w_p and w_s are the pump and signal laser beam diameters. An effective gain

length L has also been introduced where

$$L = l_w erf(\frac{\sqrt{\pi}}{2}\frac{l}{l_w}) \quad . \tag{3.6}$$

The walk-off length, l_w, is given by

$$l_w = \frac{\sqrt{\pi}}{2}\frac{w_p}{\rho}\sqrt{\frac{w_p^2 + w_s^2}{w_p^2 + w_s^2/2}} \quad , \tag{3.7}$$

where ρ is the walk-off angle. Therefore, the single pass signal power gain is

$$|\frac{A_s(l)}{A_s(0)}|^2 = \exp(-2\alpha l)\cosh^2 \Gamma L \tag{3.8}$$

For ns OPO operation, the buildup to threshold may be calculated by assuming a Gaussian time profile for the incident pump intensity. This yields a time dependent gain coefficient, Γ, described by

$$\Gamma = \Gamma_0 \exp -(t/\tau)^2, \tag{3.9}$$

where τ is the $1/e^2$ intensity of the pump pulse width. The generated signal wave is amplified from the initial parametric noise field as it makes m cavity trips. During a single trip the pump intensity is assumed to be constant.

Thus, in a single cavity after m passes, the signal power is

$$P_m = P_{m-1}\{R\exp(-4\alpha l)\cosh^2[\Gamma_0 \exp -(t_m/\tau)^2 L]\} \quad , \tag{3.10}$$

where R is the reflectivity of the cavity. Here, the threshold output level is defined either as a signal energy of 100 μJ, or a signal power-to-noise power ratio of $\ln(P_m/P_0) = 33$ [11]. A time independent gain profile of width $\overline{\tau}$ is introduced,

$$\overline{\tau} = 2\tau\{\ln[\frac{\Gamma_0 L}{\ln(1/\sqrt{R} + \sqrt{(1/R) - 1})}]\}^{-1/2} \tag{3.11}$$

which, in the long pulse limit (*i.e.*, pulse width $\gg$ round trip time), leads to [13]

$$\Gamma_0 L = 2\sqrt{\pi}[\frac{\overline{\tau}/2\tau}{err(\overline{\tau}/2\tau)}] \tag{3.12}$$

Solving equations (3.12) and (3.11) iteratively generates values for $\overline{\tau}$ and $\Gamma_0 L$. The threshold pump peak intensity is therefore, using equation (3.4) and $I = \frac{1}{2}nc\epsilon|A_p|^2$,

$$I_0 = (\Gamma_0 L)^2/\sigma g_s L^2 \quad , \tag{3.13}$$

where

$$\sigma = \frac{2\omega_s\omega_i d_{eff}^2}{n_s n_i n_p \epsilon_0 c^3} \quad . \tag{3.14}$$

The energy fluence threshold is calculated by integration to be $J_0 = \sqrt{\frac{\pi}{2}}\tau I_0$. Assuming $\overline{\tau}$ is fixed at 2τ, we find

$$J_0(\overline{\tau} = 2\tau) = \frac{2.225}{\sigma g_s L^2}\tau[\frac{L_c}{2\tau c}\ln(\frac{P_n}{P_0}) + 2\alpha l + \ln(\frac{1}{\sqrt{R}}) + \ln 2]^2 \quad . \tag{3.15}$$

This is the threshold energy for a Gaussian profile time dependent pump pulse with the pump passing through the cavity only once. L_c is the optical length of the cavity. If the pump beam is double passed by back reflecting it, the threshold energy is lowered to

$$J_0(\overline{\tau} = 2\tau) = \frac{2.225}{\sigma g_s L^2}\frac{\tau}{(1+\gamma)^2}[\frac{L_c}{2\tau c}\ln(\frac{P_n}{P_0}) + 2\alpha L + \ln(\frac{1}{\sqrt{R}}) + \ln 2]^2 \quad , \tag{3.16}$$

where γ is the ratio of the backward to forward pump field amplitude inside the crystal. The above equations, (3.15) and (3.16) provide considerable guidance as to the design of *ns* OPO cavities:

- The first term in the square bracket indicates the effective loss due to the buildup time during pulsed operation. Therefore, the cavity length L_c should be minimized to be as short as possible.

- The second and third terms describe the increase of threshold due to absorption

loss and cavity output coupling losses. The final term is due to single pass pump or double pass pump operation. According to these two equations, the reflectivity R should be as high as possible in order to reduce the threshold. Many pump lasers have short pump pulses, however, *e.g.*, the Coherent Infinity laser has a pulse width of $\simeq 2$ ns at 355 nm. If the cavity length is roughly 9 cm, or 0.3 ns in optical path length, these two equations are no longer valid, and an exact numerical simulation is required. The first term will likely dominate the threshold factors and dictate the operational threshold under such conditions if the other losses are not too high.

- The double passing of the pump beam is very helpful in reducing the operational threshold of the OPO cavity. If $\gamma \simeq 1$, the threshold is lowered by approximately a factor of *four*.

- The threshold pulse energy is proportional to the inverse of σ, which means that the threshold pulse energy is proportional to the inverse of the *square* of d_{eff}, the 2^{nd} order nonlinear optical coefficient. Therefore, choosing a crystal's cut angle so as to optimize the d_{eff} is very important in lowering operational threshold of the OPO.

Significantly, the above equations assume that the pump laser beam is well collimated (*i.e.*, $\Delta k = 0$) and has a uniform phase front of high optical quality. In reality, the beam quality is far from ideal, and the threshold may be increased significantly because of poor pump laser beam quality.

The efficiency of a *ns* OPO is closely related to its operating threshold. In order to operate efficiently, assuming low cavity loss due to absorption and unwanted Fresnel reflection, the pump laser pulse energy should be at least twice the operating threshold. In addition to the oscillation threshold, one should also consider the process of "back conversion" for efficient operation. Back conversion, that is parametric conversion of energy in the phase matched beams back ino the pump laser field, is very important factor to consider if high efficiency operation is envisioned. Numerical models based on the energy flow equations (2.17), (2.18), and (2.19) of Chapter 2 are

presently under development to simulate OPO and OPG processes. An interesting general feature that follows from these considerations is that the length of the crystal should not be as long as commercially feasible due to back conversion.

In order to operate efficiently, the damage threshold of all the crystals and optics should lie well above the oscillation threshold. Generally speaking, in order to run the OPO reliably over a long period of time, the crystal material and optical coatings should have a damage threshold at least ten times that of the oscillation threshold. In order to achieve this goal, the NLO crystal quality and the optical coating damage thresholds all need to be improved over present values, or one needs to find new NLO crystals with lower operating thresholds. The $LiNbO_3$ crystal is a perfect example of these two directions. Bulk $LiNbO_3$ has a low damage threshold so it cannot be used in an OPO over long periods of time. The improved MgO:$LiNbO_3$ version of the material has a slightly higher damage threshold but remains sufficiently low that OPOs based on $LiNbO_3$ are not very durable. On the other hand, Periodically Poled $LiNbO_3$ (PPLN) lowers the oscillation threshold by two orders of magnitude, therefore, OPOs based on PPLNs can be very easy to setup and are quite reliable [12].

3.1.2 Bandwidth properties of *ns* OPOs

The linewidth of an OPO is dictated by a crystal's Single Pass Gain (SPG) bandwidth, along with its dispersion and crystal length, as given by the spectral acceptance bandwidth formulae in Chapter 2. When the pump beam is not perfect, it is also necessary to include the contributions from the pump beam's full angle divergence ($\delta\theta_p$) and optical bandwidth ($\delta\nu_p$). The signal bandwidth inside the OPO is then proportional to

$$\Delta\nu_s^{SPG} \simeq |[(c/L) + (c/2\lambda_p)(\partial n_p/\partial\theta_p)_0\delta\theta_p + \Delta\nu_p\beta_{pi}]|/\beta_{si} \tag{3.17}$$

$$\beta_{jk} = [(n_k - n_j) - \lambda_j(\partial n_j/\partial\lambda_j)_0 + \lambda_k(\partial n_k/\partial\lambda_k)_0] \quad , \tag{3.18}$$

where $j, k = s, p$ or i are the signal, pump and idler respectively. β_{jk} is derived from the acceptance bandwidth $\Delta\nu_j$ given in Appendix A.

The actual spectroscopic linewidth of the OPO radiation, emitted under stable operation conditions well above oscillation threshold and after multiple passes in the OPO cavity, can often be several times *narrower* than the $\Delta\nu_s^{SPG}$. This is due to the fact that the multiple passes inside the cavity allow the OPO crystal act as a spectral filter. Thus, it is convenient to introduce an empirical scaling factor to reduce the SPG bandwidth to match the observed bandwidth. This factor is related to the number of round trips the OPO pulse undergoes inside the cavity. The larger numbers of round trips (decided by the pulse width of pump laser and cavity length), the larger the scaling factor. In order to reduce the OPO bandwidth, an OPO cavity should be made as short as possible to keep the pump laser pulse in the cavity for as long as possible while not compromising peak intensity and total pulse energy. This approach is bourne out by our BBO-3B II OPO pumped by a Spectra-Physics GCR-16s Nd:YAG laser with an extended cavity length option, for which the pulse width about 8-10 ns at 355 nm. The OPO cavity produces radiation with a bandwidth of about 1 cm^{-1}. When the same OPO cavity is pumped by a Coherent Infinity Nd:YAG laser (pulse width about 2 - 2.5 ns at 355 nm), the output bandwidth increases to $\geq$2 cm^{-1}, a factor of 2 larger.

Equation (3.17) predicts that the SPG bandwidth should be different for the signal and idler waves. In reality, they have the similar bandwidths. This arises because the signal and idler exchange energy as the the three waves interact inside the nonlinear crystal, especially when the starting signal or idler field is strong. The final bandwidth will then be decided by the initial wave bandwidth, be it signal or idler.

3.2 Simple 355 nm-pumped Type II BBO OPO

3.2.1 Design considerations

Optical Parametric Oscillators (OPOs) based on type I phase matching in BBO crystals have been developing rapidly over the past decade. Type I BBO OPOs can achieve high effciency and wide tunability [1],[2], particularly when pumped at 355 or

266 nm. The inherent gain linewidth in type I BBO OPOs varies from sub-nanometer to many nanometers as the wavelength is tuned toward degeneracy, however. For free running type I BBO OPOs, this inconsistent linewidth precludes many applications where (sub-)wavenumber resolution is required. Alternatively, type I BBO OPO designs based on grazing incidence gratings offer high spectral resolution, but lower efficiency. In order to generate >10 mJ of energy in the visible and UV, for example, over 300 mJ of 355 nm is routinely required to pump an $OPO + OPA$ design, which adds to the cost and complexity of such systems [2]. Here, a very simple free running OPO based on type II phase matching in BBO crystals is described which contains no frequency selective elements, yet has consistently narrow linewidth. It has a simple plano-plano cavity design, low threshold, extraordinarily high doubling efficiency, and covers the same tuning range as BBO OPOs based on type I interactions.

To our knowledge, *ns*-pulse length OPOs based on type II phase matching in BBO crystals have been reported only once before [14], and these authors were only able to demonstrate tuning the from 480 to 630 nm. There are two main reasons that type II BBO OPOs have not received the same wide attention as their type I BBO counterparts. First, type II phase matched BBO crystals, although they give consistently narrow linewidth output, have much smaller non-linear coefficients than do BBO crystals cut for type I interactions, especially near degeneracy. The value of d_{eff} for type II BBO is

$$d_{eoe} = d_{22} \cos^2 \theta \sin 3\phi \quad . \tag{3.19}$$

Where ϕ =30°, d_{eff}^2 is proportional to $\cos^4 \theta$. Based on equation (3.19), the threshold will increase quickly as the tuning angle θ increases. Figure 3.1 shows a plot of the d_{eff}^2 for type I and type II BBO material over the 410 - 700 nm tuning range. Clearly, the d_{eff}^2 for a type II BBO at $\lambda_s = 700$ nm decreases to 30% of the d_{eff}^2 value when $\lambda_s =$ 420 nm. This means that the operational threshold of the II BBO OPO cavity should increase two-fold as it is tuned toward the red limit of the cavity. The reported type II OPO cavity [14] has a limited tuning range up to 630 nm (signal) mainly because of the rapidly decreasing d_{eff}^2 near degeneracy.

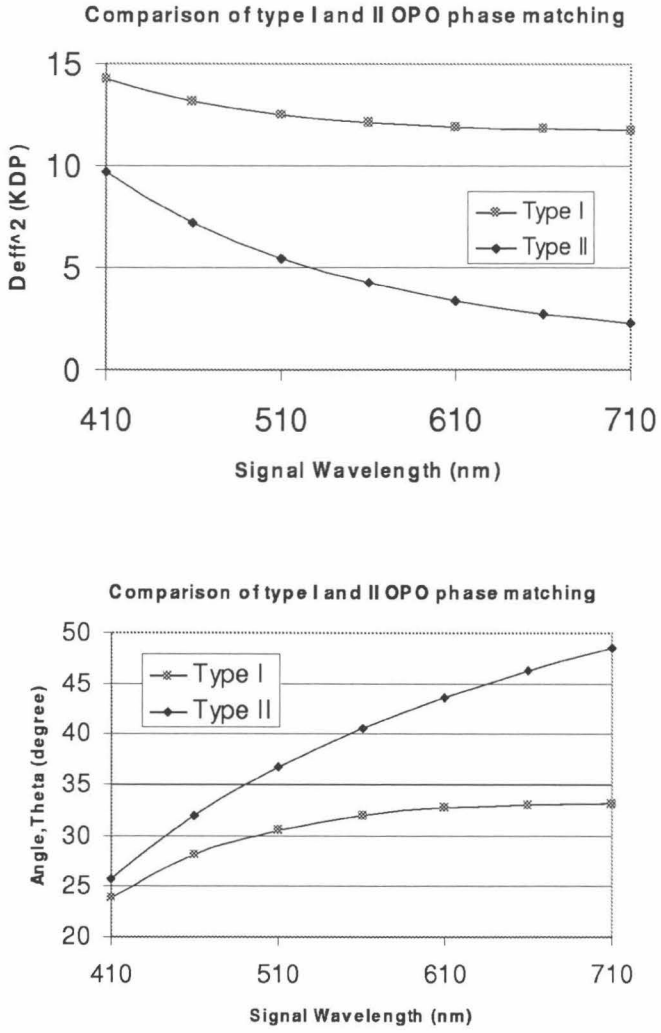

Figure 3.1: The upper plot shows the d_{eff} of the type II BBO when it is phase matched to generate radiation from 410 nm to 710 nm when pumped at 355 nm, and the lower plot shows the internal angle tuning range required to perform the same tuning range.

Second, type II BBO crystals require much larger tuning angles than do their type I counterparts in order to cover the complete tuning range when pumped at 355 nm. Therefore, long and large aperture BBO crystals must be used to generate efficient output. For example, to cover the 410 - 710 nm signal region, a type II BBO crystal must be rotated from 27° to 48° internally, or 38° externally. For a pump beam size of 6 mm, and an interaction length of 12 mm, a crystal of size 12×6×12 mm^3 is required. The cost for such crystals was well over \$10K/piece even as recently as three years ago. Fortunately, improved crystal growing technology has now made such large crystals routinely available. Commercially grown BBO crystals using flux methods can now use boule sizes up to $\phi = 135$ x 32 mm^3, and this permits the mass production of BBO crystals with high optical homogeneity in sizes up to 20×20×25 mm^3. More recently, R&D efforts have improved the Czochralski (CZ) method such that high quality BBO crystals can now be grown 100 times faster (8 hours vs. 2 months) than the traditional flux method. Although the size of CZ grown crystals still need to be increased in order to obtain large volume BBO crystals suitable for OPO systems, it is predictable that a sizable quantity of high purity, large size BBO crystals will soon be routinely available. Along with the crystal growing methods, crystal polishing and coating techniques have also been improved. Protective coatings from CASIX, for example, also serve as a broad band Anti-Reflection (AR) coating that provides less than 2% reflection over a 500 nm tuning range in the UV/visible region. It can also withstand up to 500 MW/cm^2 355 nm power densities for *ns* pulses — or 1 J/cm^2/pulse (data collected from OPO operational tests).

The limited tuning range of the previously reported II BBO OPO arose from its cavity design. In this design [14], the signal wave (λ <710 nm) was resonated, so the cavity mirrors had to withstand high laser intensity (up to 100 MW/cm^2) throughout the visible tuning range. For broadband dielectric mirrors that provide over 95% reflectivity in bandwidth of at least 250 nm in the UV/visible, all have damage thresholds lower than 100 MW/cm^2; and metallic mirrors, such as protected Al mirrors, have wide reflectivity but low damage thresholds, especially in the 410 to 480 nm region. On the other hand, metallic mirrors, especially protected Ag mirrors,

have very high reflectivity (> 98%) at wavelengths longer than 700 nm, and a peak damage threshold well above 100 MW/cm^2 from 700 nm to 10 μm.

As pointed out in the previous section discussing the oscillation threshold of short cavity *ns* OPOs, the equation describing the operating threshold does not always accurately characterize the relationship between the output coupler reflectivity and the OPO operational threshold. Similar experimental results were obtained by Byer *et al.* [13] in the case of a 1064 nm-pumped $LiNbO_3$ OPO, for which there was a large discrepancy bewteen theory and experiment for pump pulses even as long as 10 to 20 ns. Indeed, they demonstrated that the oscillation threshold is insensitive to the reflectivity (R). We are in the process of developing a numerical model which quantitatively considers the short duration of the *ns* pump laser pulse. Qualitatively, intense pump pulses can exceed the operational nearly instantaneously — this is verified by the fact that the delay between 355 nm-pumped OPO pulses and the pump pulse itself is only 1 ns, at most, for both 2 ns and 5 ns pump pulses at 2x-3x threshold. Therefore, the feedback, or reflectivity, of the cavity is no longer critical, and efficient utilization of the pump pulse becomes the key to improved operational efficiency and lowered threshold values.

3.2.2 Details of the type II BBO OPO cavity

Building on the above results, a very simple linear cavity was Designed and tested. As shown in Figure 3.2, it consists of a plano rear mirror M_1, which is a standard metallic reflector in the near-IR (protected Ag); a plano output coupling mirror M_2, which is a standard normal incidence Nd:YAG high reflector at 355 nm; and a pump input coupler M_3, which is a standard 45° high reflector for P-polarized 355 nm light. There are two counter-rotating type II BBO crystals inside the cavity that are controlled by digital DC servo motors The 6×12×12 mm crystals are cut for type II phase matching at θ=37° and ϕ=30°, and are coated with the high damage threshold (>500 MW/cm^2 at 355 nm for ns pulses) protective coating mentioned in the previous section, which also serves as a broad band AR coating. The 355 nm pump beam is

P-polarized with respect to the surface of M3, and so with type II phase matching the signal is S-polarized while the idler is P-polarized, respectively. Thus, the idler experiences low losses while the signal experiences higher losses inside the cavity. A long wave pass filter (RG715 from Schott Glass) is also inserted between M_3 and M_1 at a 45° angle of incidence for the P-polarized idler. This filter will completely absorb all the signal wavelength while being close to Brewster's angle for the idler, and a (weakly) singly resonant OPO is therefore formed on the idler.

The servo motors have very high translational resolution (0.5 μm) and repeatability, ± 2 μm (Model 850F from Newport Corporation). They are controlled by an OEM motional control PC plug-in card (Model DCX-PC100) from Precision Motion Control (PMC), Inc. Each card can control up to 8 digital servo motors and does not require additional power supplies. The PC can host as many motion control cards its slots will allow. This configuration makes the control of the OPO very flexible. Theoretically, it should be straightforward to add as many control axes as needed later in order to further extend the OPO wavelength and to control different experiments automatically. The PC100 card can also control any type of digital DC servo motor or stepper motor, and it houses an RS232 serial port and GPIB functionality so that an independent OPO system can be constructed with this card in a PC compatible computer. Windows-based software drivers, such as Visual BASIC, Visual C, and LabView, are provided by PMC to enable a variety of programming languages to be used for control of the DC servo motors.

The two crystals are controlled independently, in order to synchronize the angle of incidence for each crystal. In many OPO cavities, a grating in the Littrow or Litman configuration is used to narrow the bandwidth. Therefore, there is a relatively simple relationship between the angle of the grating and the wavelength — *i.e.*, an OPO cavity with a grating acts as a monochromator, and the wavelength calibration is relatively simple once the crystal and grating angles are synchronized. Typically, some 20 to 30 calibration points over the tuning range can be used to precisely calibrate the OPO. In the cavity design described here, there are no internal dispersive elements which have a simple relationship to the wavelength. Instead, it is the relatively

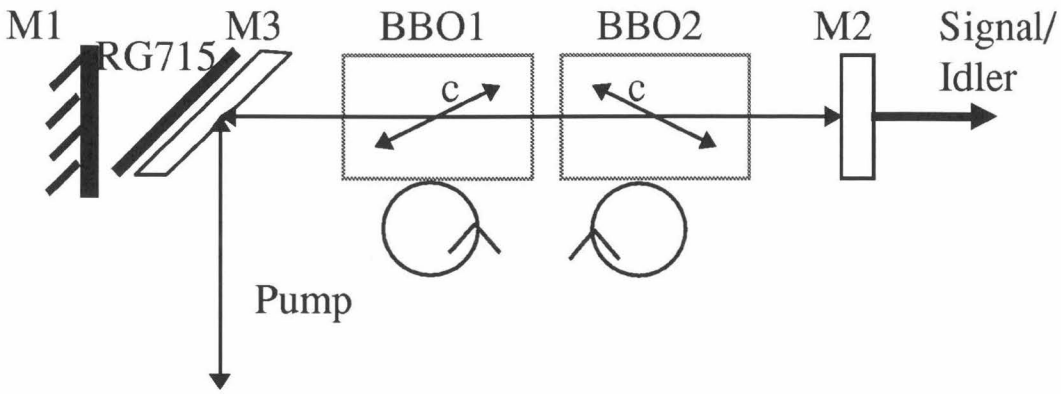

Figure 3.2: A type II BBO OPO pumped at 355 nm. The type II BBO OPO cavity resonates the idler wave, and uses two counter-rotating BBO crystals to cover the 410 to 2500 nm region. This design can be readily changed to 266, 532 or 1064 nm pumping with proper optics and crystals in the cavity.

complex phase matching relationship of type II BBO crystal that determines the wavelength-crystal positioner relationship. Thus, to generate precise and repeatable wavelengths with this OPO cavity, the wavelength must be calibrated very accurately with respect to the angle of the crystal, or directly to the position of the digital servo motors.

Theoretically, this should be a simple calibration and regression process. Since the motor's absolute step size is only 0.05 μm, however, the digital motor counts can be very high — over 10^6 for the complete tuning range! Thus, there is no simple function that can accurately correlate the wavelength even to a single axis, much less to the two axes simultaneously. Further, even small errors introduced by a regression polynomial function can easily translate into a position error of well over 100 motor counts because of the large number of total motor steps involved. A "dynamic" regression method was therefore adopted. In the dynamic regression method, calibration tables as outlined above can still be used. Instead of performing the regression over the complete tuning range to a high order ($n > 3$) polynomial, however, only a 2^{nd} order polynomial is used over a smaller number (<10) of calibration points that span a limited tuning range (<50 nm). The center point of the limited number of calibration points is dynamic, following the target wavelength. In this way, the potentially large calibration errors are avoided by retaining only 2^{nd} order polynomials, yet the regression is accurate enough over the entire tuning range using only a single calibration table. This table consists of about 60 points covering the complete signal tuning range from 420 to 680 nm, and from 740 to over 2500 nm for the idler wave.

3.2.3 Performance of the 355 nm-pumped type II BBO OPO

The OPO power spectrum measured external to the cavity and without Fresnel corrections is given in Figure 3.3. A Spectra Physics Nd:YAG GCR-16 laser produced the pump beam with a beam diameter of 5.5 mm, a pulse energy of 135 mJ, and a beam divergence of less than 0.5 mrad (FWHM). The spectrum shows the usable efficiency of the OPO is as high as 30%. We attribute this high efficiency to the following

factors – pump beam double passing, walk-off compensation inside the BBO crystals, and extra-long interaction lengths coupled with an efficient broadband AR coating on the BBO crystals. Double passing lowers the threshold of this OPO design by almost 70%, while the counter rotating BBO crystals [1, 10] provide walk-off compensation. The walk-off compensation efficiency increase is fairly small in an idler-resonating type II BBO OPO because the idler has the same polarization as the pump. Thus, they walk-off in the same direction although at slightly different angles ($\sim 0.1°$). The two crystals design does reduce the linewidth of the OPO output due to the longer effective interaction length inside the cavity, however [10]. Also, the counter rotation cancels the optical displacement caused by the crystal refraction. Finally, durable broadband AR coatings on the BBO crystals reduce the overall loss inside the OPO cavity, and improve the lifetime of the crystals as well. Figure 3.3 also shows that the tuning gap at the degeneracy point (710 nm) can be easily covered with this OPO design. Because the signal and idler have orthogonal polarizations, a simple polarization beamsplitter can be used to separate the signal and idler waves near the degeneracy point. This feature has been used in the doubling experiments outlined below.

The OPO's signal (410 - 710 nm) linewidth was mesaured with a Burleigh WA-4500 pulsed wavemeter, and that of the idler by collecting the photoacoustic absorption spectra of various gases in the near infrared. The results are summarized in Table 3.1. Due to energy conservation and three wave interactions in the nonlinear optical process, the linewidths of the signal and idler are equivalent, being consistently narrower than 2 cm^{-1} throughout the entire tuning range when pumped by a single frequency injection seeded Nd:YAG laser at twice the threshold intensity. The linewidth is less than 1 cm^{-1} when the signal wavelength is below 600 nm, as shown by the photoacoustic absoprtion spectrum of C_2H_2 presented in Figure 3.4.

When pumped with an unseeded Nd:YAG laser ($\Delta\nu$ at 1064 nm $\sim$ 1 cm^{-1}), the linewidth increases by a factor of two, as is also demonstrated in Figure 3.4. The rotational structure of C_2H_2 is nicely resolved when a seeded single frequency pump source is used, but only barely so for an unseeded pump source. This effect, namely

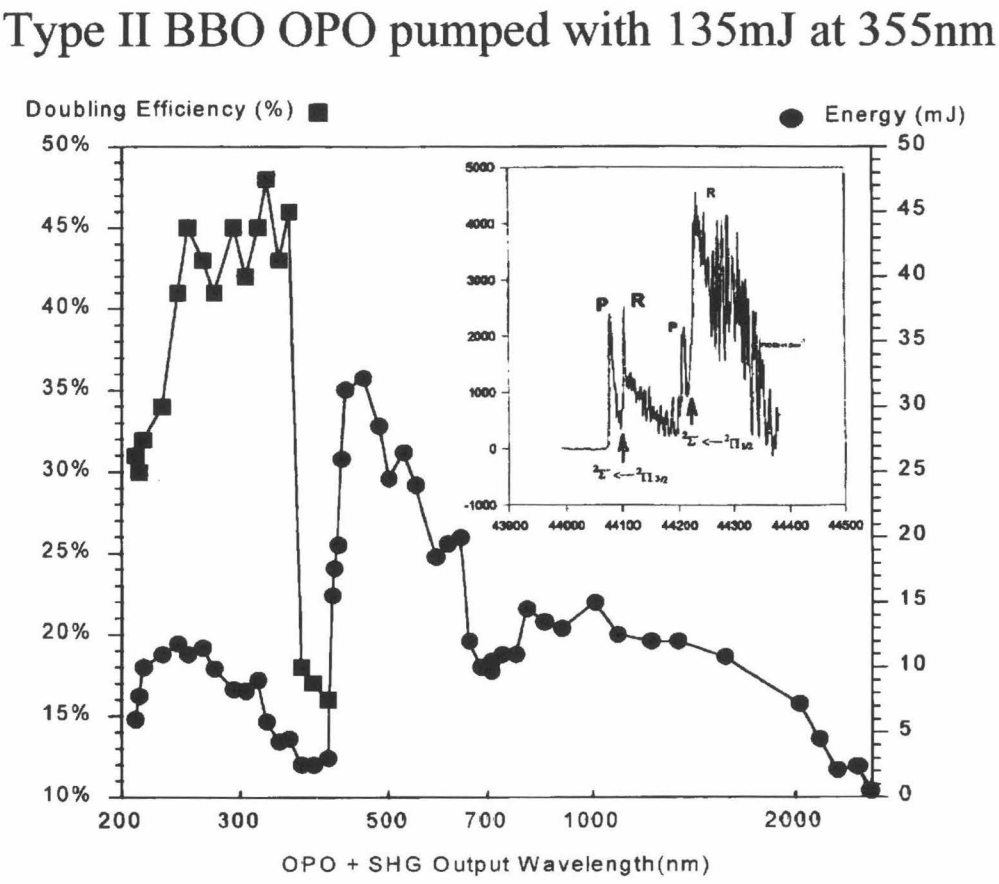

Figure 3.3: The power spectrum and doubling efficiency of the 355 nm-pumped type II BBO OPO, measured at a pump pulse energy of 135mJ/pulse. The pump laser operates in a single frequency mode. The direct output of the OPO ranges from 410 to 2500 nm. Subsequent UV generation from 208 to 410 nm is achieved in three BBO doubling crystals.

Table 3.1: Material parameters for 7 mm long BBO type I doubling crystals, and the linewidth characteristics of the type II BBO OPO system. The corresponding idler radiation has linewidths comparable to the signal due to the conservation of energy.

Wavelength (Signal / Idler, nm)	420	500	580	660	700	780	860
II BBO OPO output linewidth (cm^{-1})	0.7	0.8	1.0	1.4	1.7	1.4	1.2
SHG Acceptable Linewidth (FWHM, cm^{-1})	1.0	1.7	2.7	3.7	4.4	5.8	7.5
Angular Acceptance (μrad, FWHM)	680	430	500	620	680	820	970
d_{eff} (x KDP)	1.1	2.5	3.0	3.3	3.4	3.6	3.7
Doubling Efficiency	30%	45%	45%	48%	45%	16%	15%

Note: SHG efficiency measured with OPO pumped at 2x threshold.

that the linewidth of the OPO is affected by the linewidth of the pump source, is not significant when the change in pump linewidth is small (see, for example [14]), but is clearly measurable when a single frequency pump source is used.

Table 3.1 also summarizes the doubling efficiency that can be obtained with this OPO design. The doubling experiments were performed in 7 mm long AR-coated BBO crystals. Over 40% doubling efficiencies have been observed for signal wavelengths bewteen 470 and 710 nm, over 30% efficiency for doubling signal radiation from 418 to 470 nm, and over 10% efficiency for doubling idler input in the 710 to 900 nm range. The relatively low efficiency for idler doubling was improved to over 30% with a zero order waveplate (see below), and the highest efficiency obtained was 48%. These doubling efficiencies are among the highest ever reported for an OPO. The highest doubling efficiency previously obtained in BBO crystals was 20% [2], while values near 30% have been reported in KDP crystals and for tunable dye lasers as well. The doubling efficiency we obtained is especially high in the deep UV range between 208 and 225 nm. This technology should ultimately provide a compact, efficient and tunable deep UV source, which is finding increasing applications in many areas such as the subsequent generation of tunable vacuum UV radiation, environmental characterization, and material processing.

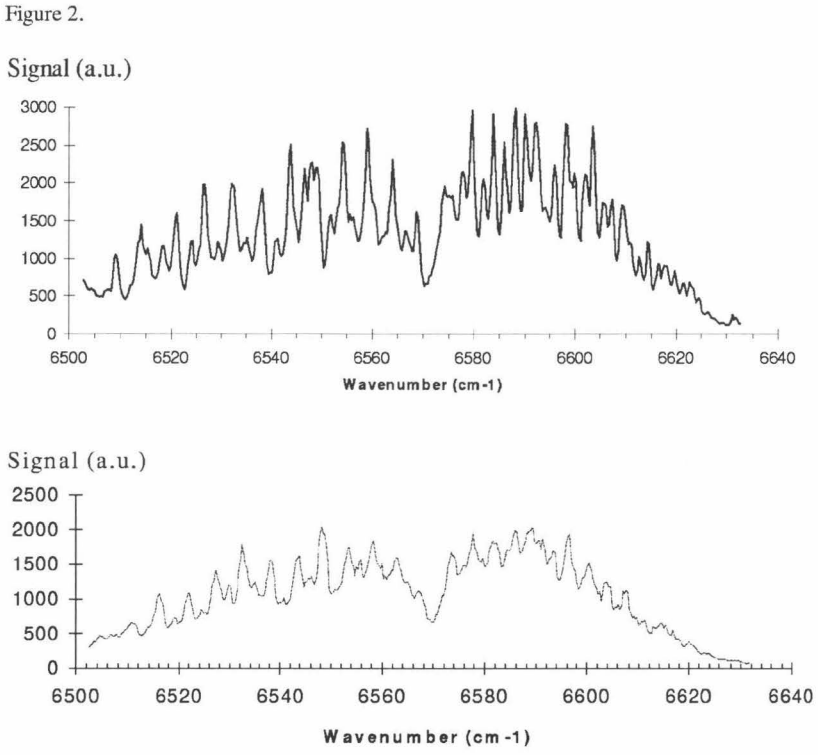

Figure 3.4: Comparison of the OPO linewidths when pump the laser operates under SLM conditions. (a) Photoacoustic absorption spectrum of C_2H_2 taken with a type II BBO OPO pumped by the third harmonic (pulse width $\simeq$10 ns of a seeded Nd:YAG laser (whose linewidth is about 100 MHz), showing clearly resolved rotational structure. The measured linewidth of the OPO signal is about 1 cm^{-1}. (b) The same photo acoustic absorption spectrum of C_2H_2, now taken with a type II BBO OPO pumped by an unseeded Nd:YAG laser (of linewidth $\simeq$ 1 cm^{-1}). Here the rotational structure of C_2H_2 is only barely discernible and the signal-to-noise ratio drops as the linewidth goes up. The measured linewidth is about 2 cm^{-1} for the OPO signal beam near 460 nm.

In order to generate such high doubling efficiencies, both the linewidth and divergence of the OPO output must be smaller than the spectral and angular acceptance of the doubling crystal. The type II BBO OPO linewidth is consistently narrower than 2 cm^{-1}, while the linewidth acceptance of a type I BBO doubling crystals varies from less than one wavenumber at 420 nm to a few wavenumbers at 710 nm. Table 3.1 compares the linewidth acceptance of type I BBO doubling crystals with the linewidth of the type II OPO at various wavelengths throughout the tuning range. As can be seen, the OPO linewidth is always smaller than the linewidth acceptance (FWHM) of the doubling crystal. Thus, no energy is lost in the doubling process.

As noted above, the divergence of the OPO must also be smaller than the angular acceptance (FWHM) of the doubling crystal for efficient doubling to be achieved. It is well known that in a plano-plano cavity the beam divergence of the non-resonated photon, be it idler or signal, will be substantially reduced. For example, Orr *et al.* [15] observed the divergence for the idler from a plano-plano signal resonant type I BBO cavity to be so small as to be indistingushable from the pump – or even smaller. Similar cavities resonated on the idler also possess very small signal wave divergences. We have, for example, achieved less than 0.5 mrad divergence for the signal from a type I idler resonant BBO OPO system, with a doubling efficiency (>18%) that is limited primarily by the fact that the linewidth of type I BBO OPO is larger than the linewidth acceptance of the doubling crystal.

In the present work on an idler resonated type II BBO OPO, less than 400 μrad signal beam divergence has been observed in the sensitive plane of the doubling crystal. This divergence is smaller than the angular acceptance of BBO type I doubling crystals throughout the OPO tuning range. The divergence of the signal in the insensitive plane of the doubling crystal is about 600 μrad when the signal is less than 600 nm, but increases to >2 mrad at degeneracy. This relatively large divergence in the insensitive plane of the doubling crystal does not affect the doubling efficiency because the acceptance angle in the insensitive plane is very large, as was discussed in Chapter 2. At the blue end of the tuning range, the doubling efficiency drops below 40% because the d_{eff} of the BBO doubling crystals decreases rapidly below 460 nm,

as is summarized in Table 3.1. Also, the absorption by the BBO crystal rises quickly in this wavelength region, which places limits on the average power that a single BBO crystal alone can produce. New theories and technologies are proposed to solve this problem below.

The doubling efficiency of the idler (710 - 840 nm) is only 10% because the divergence is >2 mrad in the sensitive plane of the BBO doubling crystal, which is larger than its angular acceptance. Because the divergence of the idler in the other direction is as small as that of the signal, the idler doubling effciency can be improved by using a zeroth order half-wave plate to rotate the polarization of the idler by 90 degrees, thereby greatly reducing the idler divergence in the sensitive plane of the doubling BBO crystal. Indeed, doubling efficiencies of >30% were obtained after inserting a zeroth order waveplate optimized for $\lambda = 780$ nm. The introduction of a zeroth order waveplate has two advantages, one is the improvement of the doubling efficiency as demonstrated, and the other is the simplification of the doubling setup after the type II OPO. The idler output of the OPO is polarized perpendicularly to that of the signal. To double the idler using the same type I BBO crystal, the axis of rotation must be changed. The zeroth order waveplate has an effective wavelength range of over 150 nm (or ± 75 nm), centered at 780 nm, and can therefore be inserted in the beam path as needed to change the idler's polarization and thus use the same BBO crystal to double both the signal and idler.

Next, we attempt to explain why the divergence of the non-resonated wave in a singly resonant plano-plano OPO cavity is so small. To our knowledge, this phenomena has not been well explained despite having been observed many times. Since the non-resonant wave obtains all its energy in a single pass, its beam quality will be dictated by the beam quality of both the pump and the resonated wave. Following Brosnan and Byer [13], the steady state equation for obtaining the beam diameter of the resonated wave inside a singly resonant plano-plano oscillator (SRO) is given by

$$(\frac{\pi}{2L_c\omega_s\lambda_s})^2\overline{\omega_s}^6 + \overline{\omega_s}^2 - \omega_p^2/2 = 0 \quad , \tag{3.20}$$

where $\overline{\omega_s} = \omega_s$ are the beam waists under steady state conditions, L_c is the cavity length, and the subscripts i, s and p denote the idler, signal and pump fields, respectively. Note that here, idler refers to the wave that is not resonated while signal refers to the resonated wave. From the above equation, we note that the smaller the resonating wave's wavelength (λ_s) gets, the smaller the steady state ω_s becomes. For a Gaussian beam (in the far field, all three waves will have Gaussian profiles), the beam's divergence will become correspondingly larger. Thus, if the longer wavelength part of the OPO output is chosen as the resonated wave, a smaller output divergence is obtained. At the same time, the acceptance angle of the OPO crystal also starts to limit the divergence of both the resonated and the non-resonated waves.

Furthermore, because of phase-matching restrictions, if the longer wavelength side of the degeneracy point is resonated, a smaller divergence for the non-resonated wave is produced. Phase matching restrictions also explain the fact that the divergence of the signal in the insensitive plane increases as it approaches degeneracy. The divergence of the signal in the sensitive plane stays the same because it is always limited by the acceptance angle of the type II BBO crystal. Numerical simulations are currently being developed to quantitatively examine these phenomena.

The divergence of the type II OPO output is quite large in the insensitive direction, and becomes worse when the pump laser pulsewidth is short. For example, the Coherent Infinity laser has a pulse width of ~2 ns at 355 nm. The divergence of an Inifinity-pumped type II OPO in the insensitive plane is extremely large at the red limit (*e.g.*, >2 mrad full angle at 670 nm), while the divergence in the insensitive plane is less than 0.5 mrad. We attribute this to the difference of the *sign* of d_{eff} in each of the two crystals used inside the OPO cavity. This is illustrated in Figure 3.5, where it can be seen that the sign of the two type II BBO crystals cut with the same crystal angle (both θ & ϕ) must be opposite if they are arranged in a counter rotating fashion. The opposed signs of d_{eff} favor the amplification of the (slightly mismatched) sideband of the angularly diverging signal of the OPO, which is also within the crystal's acceptance angle in the insensitive plane (ϕ).

On the other hand, counter rotation is also necessary in order to cancel optical

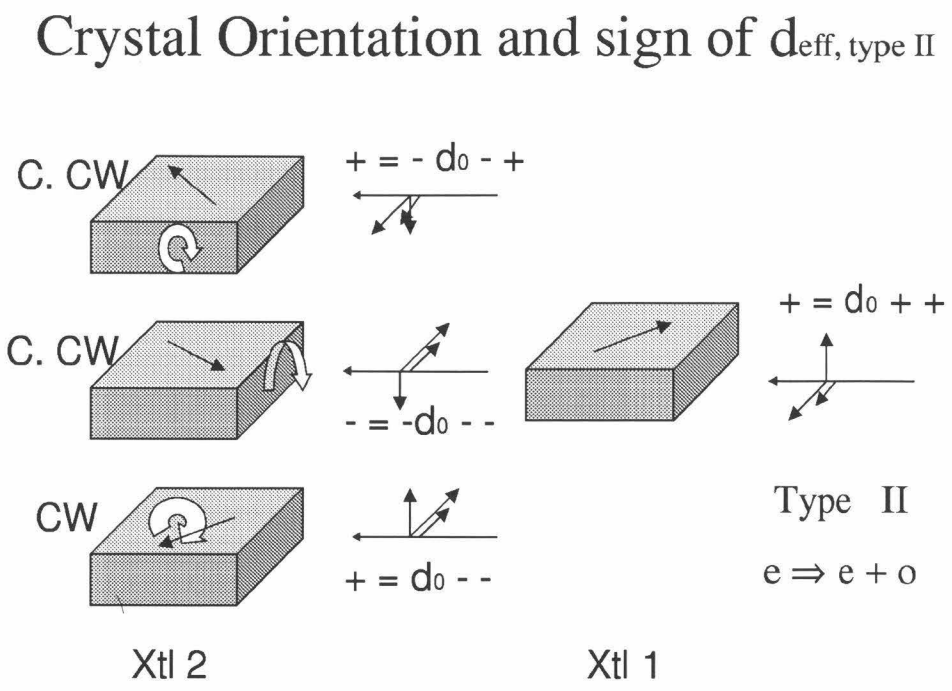

Figure 3.5: The sign of d_{eff} changes under different crystal orientations for a type II BBO crystal with $\phi = 30°$. None of the orientations above combine the proper counter-rotation sense with the same sign of d_{eff}. The two short arrows stand for the two lower energy photons, *i.e.*, signal and idler; while the long arrow stands for the higher energy photon, *i.e.*, pump.

displacements and the walk-off effect. From equation (3.19), it is clear that the the sign of d_{eff} will be opposite if the angles ϕ are set $\pi/3$ away from each other for the two crystals. This theory has not yet been tested for the type II cavity, but a comparable effect was seen in the type I BBO OPG/OPA setup described in Chapter 4.

A great deal of effort was also expended to investigate further reductions of the bandwidth of such a simple type II BBO OPO cavity. One test that was carried out involved inserting an etalon inbetween the filter and the rear mirror. Depending on the thickness (or free spectral range) and reflectivity of the etalon, a spectral resolution between 0.1 cm^{-1} and 0.01 cm^{-1} could be achieved. In order to ensure that the cavity with the etalon runs only on a single resonant frequency of the etalon, the relationship between etalon thickness (l_e in cm) and the bandwidth ($\delta\nu_{free}$ in cm^{-1}) of the simple free running type II BBO OPO shuold be related as follows,

$$\delta\nu_{free} < \frac{1}{2n_{sub}l_e} \quad , \tag{3.21}$$

where n_{sub} is the refractive index of the substrate of the etalon. The resulting OPO bandwidth ($\delta\nu_{etalon}$) with the etalon inserted is then

$$\delta\nu_{etalon} = \alpha\frac{1}{2n_{sub}l_eF} \quad . \tag{3.22}$$

α is an empirical parameter less than 1 that represents the further reduction of bandwidth as a result of multipassing inside the OPO caivty, and F is the finesse of the etalon, or

$$F = 1/\sqrt{1-R} \quad . \tag{3.23}$$

To achieve this bandwidth, the center frequency of the NLO material must be the same as the center frequency of the etalon. The center frequency of the etalon can be continuously angle tuned, and therefore the crystal angle tuning must be synchronized with the etalon angle tuning, adding complexity to the OPO operation.

When the $\frac{1}{2n_{sub}l_eF}$ is less than the cavity's free spectral range ($1/(2l_{o.c.})$, where

$l_{o.c.}$ is the optical path length of the cavity), and the center frequency of the etalon is matched to the center frequency of the OPO cavity, single longitudinal mode operation can be obtained. To match these two frequencies, a piezo is used to servo control the length of the OPO cavity, adding further to the complexity of the design. The narrowband operation of such an OPO cavity has been deomonstrated with an etalon coated at 1.6 μm, as may be seen with the NIR photoacoustic spectra of water's O-H stretch overtone vibration presented in Figure 3.6.

Operation with an etalon is quite complicated compared to that of the simple free running OPO, and the insertion loss of the etalon can be large. There are two sources of loss, one is the Fresnel loss on the surfaces of the etalon, and depends on the reflectivity of the etalon and the tuning angle — the loss increases quickly with higher etalon reflectivity and larger tuning angles. It is therefore difficult to achieve a wide tuning range with a high finesse etalon, but for nearly fixed frequency (or "step tunable") operation high efficiency can be maintained. The second source of loss depends on the pump laser pulse width, because the multi-passing of the resonant wave inside the etalon drops the number of round trips inside the cavity, thereby reducing the efficiency of the OPO, especially when the pump laser pulse is short. Due to these two factors and the broad wavelength coverage of most of the experiments presented in this thesis, the etalon design was used only infrequently.

3.3 Tunable UV generation for spectroscopy

3.3.1 Introduction

Scientifically, widely tunable laser radiation in the UV region is of great importance. Many mature spectroscopic techniques – photoionization, photolysis, UV absorption – require widely tunable UV laser sources. In the alkali metal - small molecule cluster spectroscopy experiments presented in Chapter 6, widely tunable UV laser radiation is required to accurately measure the ionization potentials of different cluster sizes. For example, the ionization potentials of the $K(NH_3)_n$ (n=1,2,3...) clusters are

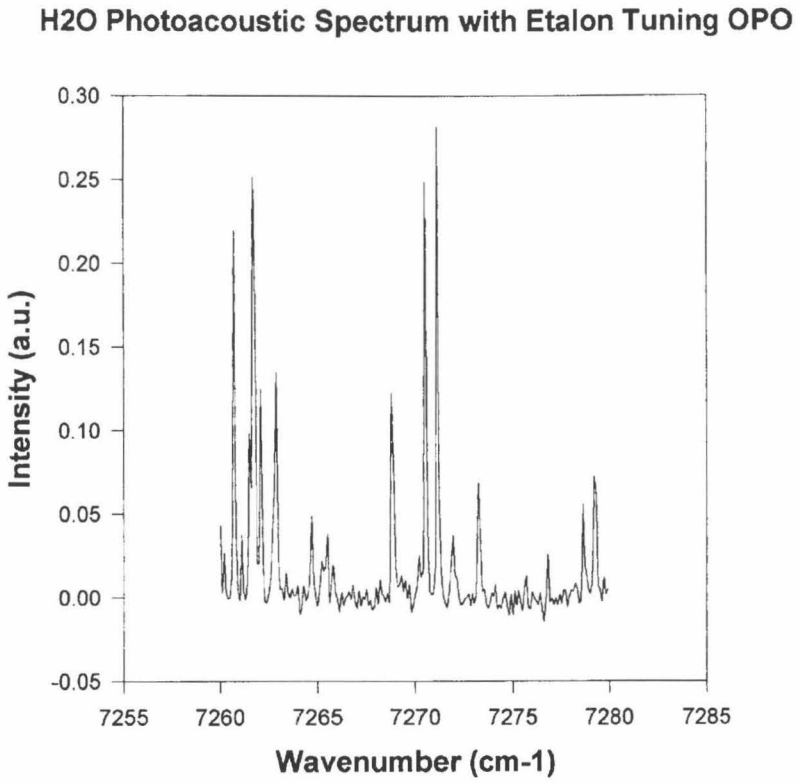

Figure 3.6: Photoacoustic spectrum of water's second overtone vibrational band at $1.6\mu m$, taken with the type II BBO OPO pumped at 355 nm and a 1.5 mm etalon with a finesse of 20 at 1.6 μm.

spread from 327 nm to 480 nm, while studies of the photolysis cross sections of molecules of atmospheric and astrophysical interest require highly tunable, highly efficient UV light sources [17, 18]. High average power UV sources could also enable many measurements were previously difficult or impossible to perform. For example, in the generation of tunable VUV radiation (λ <200 nm), the production high energy (several mJ/pulse) 212 nm pulses at repetition rate up to 100 Hz is desired.

In this section, the systems set up at Caltech to generate high Average power, widely tunable UV laser radiation will be examined. The optimum choice of crystal material will be discussed, as will the optical set up and possible ways to improve the efficiency and to extend the UV wavelength below 205 nm.

3.3.2 SHG of widely tunable UV laser radiation

Crystal materials for SHG in the UV

Shortly after the discovery of the earliest robust NLO crystals (*e.g.*, KDP and KD*P), they were used to generate widely tunable UV laser radiation. KDP and KD*P have relatively large angular and spectral acceptance. At elevated temperature (177° C), KDP can double the 532 nm at θ=90°, or in the noncritical phase matched (NCPM) condition. NCPM offers exceptionally large spectral and angular acceptance for the SHG process. KDP and KD*P have a relatively small birefregence, however, and therefore they cannot phase match direct SHG over a wide wavelength range. After the discovery of BBO, it is found that, due to its very large birefregence, BBBO could be SHG phase matched over a very wide wavelength region. Shown in Figure 3.7(a) is the SHG phase matching angle for BBO from 410 nm to 3500 nm. BBO's large birefregence limits its angular and spectral acceptance. Thus, for the same length of crystal material, BBO requires that the input beam be of much better quality, *i.e.*, that it possess smaller divergence and narrower spectral bandwidth, than is needed for KDP. The nonlinearity of BBO, however, is 3.8 times that of KDP (phase matched for 532 nm SHG). Therefore, a very short BBO crystal is just as efficient as relatively long KDP and KD*P crystals. The relationship of d_{eff} to the crystal thickness l

follows from the derivation below.

The SHG process is governed by the three wave interaction equations (2.17),(2.18), and (2.19), given in Chapter 2. For SHG the relationships are in fact much simpler since $A_1 = A_2 = I$, and $\omega_1 = \omega_2 = \omega_3/2 = \omega$ [19]. If it is supposed that Δk is a constant along the crystal axis of propagation, we have an analytical solution for SHG can be derived, namely

$$\frac{P^{2\omega}}{P^{\omega}} = \frac{|A_3(l)|^2}{|A_1(0)|^2} = \tanh^2[\frac{1}{2}\tanh^{-1}(sn[2\eta_0^{1/2}, 1+\delta^2/4\eta_0])] \quad , \tag{3.24}$$

where $\eta_0 = C^2 l^2 I(0)$, $\delta = (1/2)\Delta k L$, and $C = 5.46 d_{eff}(pm/V)/\lambda_1(\mu m)(n_1 n_2 n_3)^{1/2}$.

If $\Delta k = 0$, that is, the input beam is nearly perfect, then the above relation is reduced to

$$\frac{P^{2\omega}}{P^{\omega}} = \frac{|A_3(l)|^2}{|A_1(0)|^2} = \tanh^2(\eta_0^{1/2}) \quad . \tag{3.25}$$

So, for a perfect input beam the SHG efficiency is directly related to the nonlinear drive η_0, or more directly to $d_{eff}^2 l^2$. Clearly, in order to generate the same kind of nonlinear drive, d_{eff} is proportional to $1/l$. A BBO crystal's thickness is therefore chosen to be about one fourth that of an analogous KDP crystal (30 mm vs. 7 mm) for single input pulse considerations.

Table 3.2 compares the UV SHG properties of KDP and BBO. Apparently, with the same level of nonlinear drive, BBO actually has larger angular, spectral, and temperature acceptances and damage thresholds than does KDP. All these properties make BBO the crystal of choice to perform UV SHG.

To generate the UV radiation across the entire SHG phase matchable wavelength region (205-420 nm), 3 BBO crystals are typically used; altough novel two BBO crystal designs (θ= 56°and 36°) which use the same optical beam path and counter-rotate provide continuous coverage from 225 - 450 nm and compensate for the optical displacement during angle tuning. By adopting this design with 2 crystals that are cut for shorter wavelength SHG phase matching (θ =58°and 37°), continuous UV coverage from 215 to 410 nm has been obtained. A third crystal cut at θ= 81° is needed for the remaining 205 to 218 nm region of the phase matchable window. In the

Table 3.2: Properties of KDP and BBO when used for UV SHG

Parameters	KDP(30 mm)	BBO(7 mm)
Phase matching UV wavelength range(nm)	260-340	204.9-450+
Number of crystals to cover the tuning range in UV	4	3
Spectral Acceptance (cm^{-1}, FWHM @550nm)	1.9	2.8
Angular Acceptance (μrad, FWHM @550nm, external)	400	430
Temperature Acceptance (°C @532 nm)	0.7	6
Damage threshold (ns laser pulse, MW/cm^2 @266 nm)	>100	>60

Beam size = 5 mm, external angular tuning range = $\pm$ 20° for SHG crystal size and cut

two doubling crystal design, the crystal axes are linked together with a 0.5″ wide by 0.002″ thick steel shim stock in order to provide a flexible rotation link with minimal extension. The two axes are controlled by a single digital motor, which simplifies the design and lowers the cost. The calibration and automatic scanning process is very similar to that of the type II BBO described in the previous sections. The substantial amount of average UV power that can be generated leads to substantial thermal heating of the doubling crystal and introduces stability and repeatability problems. This is especially true for UV wavelengths below 300 nm, and possible solutions to this problem are presented next.

3.3.3 Schemes for deep UV SFG

The shortest wavelength that can be accessed through direct SHG in type I BBO is 204.9 nm. As Figure 3.7 shows, the d_{eff} of BBO decreases rapidly toward the short wavelength limit. This means that longer BBO crystals are needed to give reasonable efficiency, but at wavelengths close to 200 nm absorption by the crystal worsens. Longer crystals will absorb the UV more efficiently, driving thermal gradient that degrade the efficiency. Therefore, if possible, SFG with 1064 nm radiation should be used. Happily, OPOs are usually pumped by Nd:YAG lasers, and by using SFG

with a 1064 nm and a tunable UV photon, the type I d_{eff} is much larger. The larger d_{eff} and high 1064 nm intensity lead to mixing efficiencies that are quite high. BBO is SFG phase matchable down to 189nm, but the efficiency is limited by the strong absorption that starts to appear. LBO [26] and CBO [27] appear to have better transmission properties in this region, and are therefore promising crystals for SFG processes below 200 nm.

3.3.4 Thermal effects & the stability and scalability of high power NLO conversions

Thermal effects provide the major obstacle to manufacturing high average power all solid state lasers. For output at the fundamental frequency, thermal lensing and thermal phase distortion are the primary factors affecting solid state laser performance. Improvements in cavity design and the introduction of diode laser pump sources have led to ever higher average power lasers over the past several years. The nonlinear optical conversion of the fundamental has also improved greatly due to the optimization of a variety of novel NLO materials, *e.g.*, LBO, BBO, KTP, PPLN and CLBO [24]. These NLO conversions can be classified into two categories: harmonic generation or optical up-conversion, and optical parametric generation or optical down-conversion. Output powers in the multi-Watt range are now achievable from 355 nm to 3 μm. There is tremendous interest in scaling up the power at all wavelengths in order to take full advantage of the efficiency of solid state lasers – especially in the UV, where the currently available excimer lasers have >100 W output capabilies, but suffer from high operational cost and frequent down time. In comparison, solid state lasers can be much more rugged and reliable, particularly at the fundamental wavelength, with consumables consisting of only the final harmonic generators. Excimer lasers generate high peak intensities and average powers, placing a demanding challenge on the optics since their UV damage thresholds are typically much lower than in the visible and near IR.

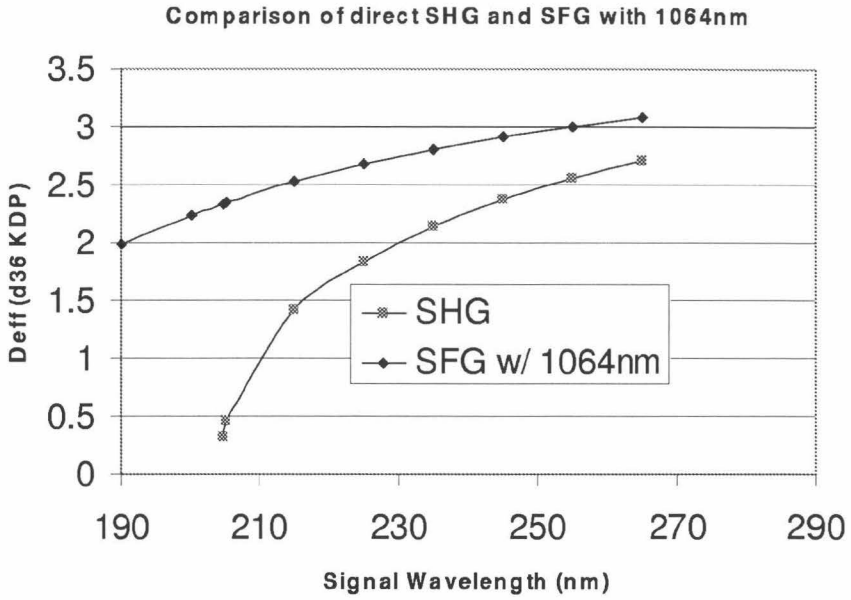

Figure 3.7: The d_{eff} of direct SHG is much less that of SFG with 1064 nm.

Phenomena observed

The availability of excellent NLO crystals such as LBO, has enabled the generation of hundreds of Watts of CW power at 532 nm. Much lower levels are available as the wavelength is pushed down into the UV/VUV or out into the IR, due to thermal heating effects inside the nonlinear optical crystals.

For example, the Infinity Nd:YAG laser can achieve 50% conversion efficiency from 532 nm to 266 nm under single shot conditions, but the efficiency drops to 35% at 10 Hz repetition rates, to 25% at 30 Hz, and to 12% at 100 Hz. Similar trends are observed for high repetition rate (>kHz) high average power lasers, namely that the conversion efficiency drops as the repetition rate or average power increases. Further, the beam shape worsens dramatically as the power is scaled up. At sufficiently high power, the output beam becomes hollow in the center due to strong back-conversion at the end of the crystal driven by the thermally induced phase mismatch. Under such conditions, the crystals has must be detuned to compensate for the thermally induced phase mismatch, and the stability of such high harmonic generators are therefore quite poor. Even under relatively low average UV power conditions, *e.g.*, about 500 mW at 280 nm, for doubling of the type II BBO OPO's tunable radiation at 560 nm, there is already substantial angular detuning as a result of thermal effects.

Similar phenomena are observed in the IR region. For example, $ZnGeP_2$ and $AgGaSe_2$ crystals enable OPO processes to be extended into the 5-10 μm region, but under higher average power, the OPO output beams are hollowed in the center, and their stability is poor. Similarly, periodically poled materials such as PPLN can be used to perform parametric conversion with low peak intensity high average power lasers, but due to visible light generated as a result of higher order quasi-phase matching, PPLN-based OPOs cannot be scaled to very high power. The same is true when PPLN is used to directly double high power 1064 nm CW light to 532 nm. When pumped at the multi-Watt level, PPLN generated beams also begin to have hollowed out beam shapes.

Sources of thermal effect

The phenomena of thermally induced phase mismatch was first discussed in detail by Eimerl *et al.* [19], who encountered the problem in their efforts to generate high average power at 532 nm by doubling 1064 nm pulses in KDP. Here, the main problem is absorption of the 1064 nm radiation inside the KDP crystals.

As shown below, however, for high order UV harmonic generation the main source of thermal loading is absorption of the UV. For any realistic nonlinear optical material, the absorption at short wavelengths will arise from two photon absorption and increased scattering by very fine inclusions inside crystal as the wavelength is decreased. The absorption from scattering around fine inclusions is a linear, and the absorption coefficient is proportional to the laser radiation intensity. This kind of absorption can be lowered by improving the crystal growing techniques to minimize the inclusions. Experiments have shown that CZ-grown BBO crystals followed by high temperature annealing have much lower scattering than flux grown BBO crystals [22]. Special procedures have also been developed by some crystal producers to select those BBO crystals with the lowest UV scattering from a crystal boule. As the UV harmonic wavelength reaches a certain limit, however, nonlinear, or two-photon, absorption begins to dominate the absorption since this cross-section increases rapidly if the two photon energy lies above the band gap of material. For example, the band gap of BBO is estimated to be $\approx$189 nm, and the two-photon absorption cross-section rises steeply as the wavelength drops below 380 nm [23]. Below 300 nm, the two-photon absorption cross-section is especially problematic because the two photon process can now be realized by one doubled UV photon and one fundamental, or visible, photon, the latter of which has a much higher intensity than the UV field. Therefore, to reduce the absorption in the UV for new nonlinear optical crystals, it is vital that their band gap be as large as possible.

For parametric processes at IR wavelengths (3-10 μm), the main heating is also that generated by the output waves, and not the fundamental input. Here, the absorption is a result of the characteristic vibrational modes inside the crystal coming

into resonance with the OPO wavelengths. Therefore, this kind of absorption is also linear in nature.

To accomodate the thermal load inside the crystals, one possible solution is to use a highly thermally conductive material to dissipate the heat. Many nonlinear optical crystals, however, are characterized by a poor thermal conductivity. For example, BBO has a thermal conductivity 50 times less than that of Sapphire, and it is thus difficult to remove the thermal load from such NLO crystals.

The thermally induced phase mismatch

For a linear absorption coefficient of α_m (m=idler, signal and pump), the heat deposited per unit volume in a crystal is

$$W = \sum_{m=1,2,3} \alpha_m I_{av}^m = \sum_{m=1,2,3} \alpha_m f \tau I_{pk}^m. \tag{3.26}$$

Regardless of the direction of the temperature gradients relative to the direction of propagation, the temperature profile established will be quadratic:

$$\nabla^2 T = W/K \tag{3.27}$$

where K is the thermal conductivity (which may not be isotropic). Along the laser propagation direction, the temperature gradient is

$$\delta T = T_1 \delta l + (\delta l)^2 W/2K = T_1 \delta l + \frac{(\delta l)^2 \sum_{m=1,2,3} \alpha_m f \tau I_{pk}^m}{2K} \quad , \tag{3.28}$$

where f is the laser frequency, and τ is the duration of the laser pulse. Therefore, along the laser propagation direction the thermally induced phase mismatch is

$$\delta k = \delta T / \Delta T \quad , \tag{3.29}$$

where ΔT is the temperature acceptance bandwidth given in Chapter 2.

The phase mismatch increase δk should be included in the three wave interaction

equation, or

$$\Delta k(l_0 + \delta l) = \Delta k(l_0) + \delta k \quad , \tag{3.30}$$

and a function of the crystal length and intensities of the three waves. Analytical solutions to such a complex differential equation are rare and depend sensitively on the nature of the boundary conditions, while a numerical solution is tedious, but straightforward.

Figure 3.8 demonstrates the SHG efficiency of a BBO cyrstal calculated by a computer simulation model under different conditions. Plot *a* shows that under perfect phase matching conditions, *i.e.*, $\Delta k \equiv 0$, the SHG efficiency increases along the crystal length and approaches unity. Plot *b* shows that when Δk is small but constant along the crystal length (*i.e.*, there is no thermally induced phase mismatch), the SHG efficiency increases along the crystal length, but cannot reach unit conversion efficiency before back conversion begins. Plot *b* further reveals that long crystals do not necessarily mean high conversion efficiency, due to beam divergence in the input laser beam. Plot *c* presents the case where Δk changes because of thermally induced phase mismatch. The efficiency is seen to increase at first, but after reaching a maximum it flattens out as the interaction crystal length increases. This saturation effect has been observed by several research groups [20]. For example, in the generation of the fourth harmonic of the Infinity Nd:YAG laser, our tests have shown that the efficiency remains nearly constant as the BBO crystal length is increased from 2 to 7 mm. Plot *d* shows that under heavy thermal loading, when the crystal is angle detuned in the direction that compensates for the thermally induced phase mismatch, the peak efficiency can be increased slightly. Importantly, there is a difference in the signs of the angular and temperature phase mismatch terms. Thus, if the crystal is detuned as the laser power is raised to maintain SHG efficiency under very heavy thermal loads, and the laser power is cycled off and on, the initially generated UV power and thermal loading is small, and the efficiency obtained before the laser was turned off cannot be regained without a complete reoptimization of the crystal position and orientation.

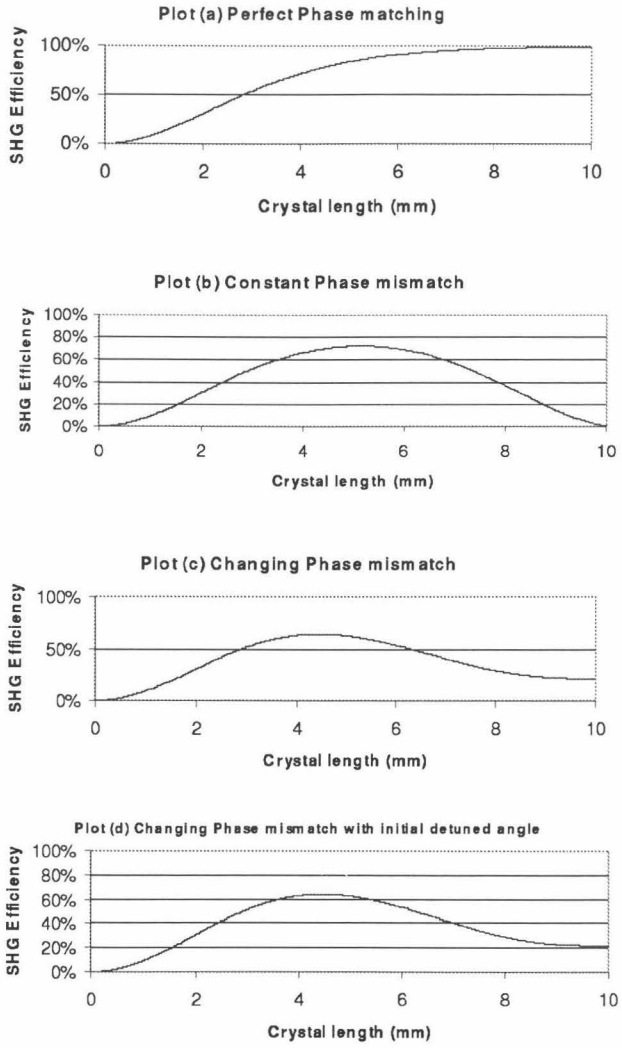

Figure 3.8: Theoretical calculation results showing SHG efficiency under different phase mismatch conditions.

Methods to solve the thermal effect problem

One way to relieve the thermal phase mismatch is to utilize the N-plate designed by Eimerl [19]. In the N-plate design, a single piece of crystal is cut into N pieces, and coolant gas is introduced over the surfaces to remove the heat gradient generated under high power operation. In this way, the scalable power llimit for the N-plate should increase as N^2. Alternatively, for constant pulse energy the conversion efficiency should be constant with repetition rates from a single shot to N^2.

For the N-plate solution to work well, however, the crystals absorption should be the same for both the fundamental and the second harmonic. This condition provides a uniform heating rate along the crystal interaction length, and the maximum of the temperature gradient is formed is in the center of the crystal(s). In reality, most crystal have drastically different absorption coefficients for the input and output waves. Thus, the heating of the crystals will not be uniform. In a single piece of NLO material, the temperature gradient will be approximately parabolic with its maximum at the entrance face and its minimum at the exit face, or *vice versa.* This behavior has been experimentally characterized YAP *et al.* [21], who utilized an IR camera to map the temperature profile at the end of a CLBO crystal. These authors found that after the laser was turned on, the temperature of the exiting face of the CLBO harmonic crystal increased 8 degrees. The authors used a thin jet of gas to cool the surface and thus reduce this temperature increase at the exit face of the crystal. In this way, the 532 nm to 266 nm SHG efficiency of the Nd:YAG 4th harmonic generator could be doubled.

The other way to relieve the thermal loading is to distribute the laser power over as large an area as possible. Toward this end, beam-scanning devices have been designed in which the input laser was scanned through the crystal aperture at a certain speed in order to distribute the heat generated over as large an area as possible [25]. Therefore, the temperature gradient is reduced inside the NLO crystal, and the power handling capability goes up. The other, fixed, version of this design is to expand (or up-collimate) the laser beam in the sensitive direction, and then cylindrically focus it

in the insensitive direction. This technique was successfully demonstrated in the low threshold OPO discussed in the previous sections, but here it could be used not only to take full advantage of the acceptance angle difference in two directions, but also to minimize the thermal load [28].

A new technique of solving this thermal loading problem in high average power fourth harmonic generation of Nd:YAG lasers is recently experimented in our lab. It is to our belief that for 266 nm harmonic generator, the actual temperature gradient inside the crystal has its minimum at the crystal's input face, and its maximum at the exit face. As the average 266 nm power increases, the temperature gradient and hence the thermally induced phase mismatch becomes larger and larger. Therefore, shorter and shorter crystals have to be used, and the total conversion efficiency also goes lower. The new technique utilizes 2 or more pieces of thin BBO crystal (<1mm), the first crystal is always tuned for optimal 266 nm harmonic generation at room temperature, with the second crystal detuned to compensate for the thermal gradient introduced by the UV radiation out of the previous crystal. This design effectively removes the accumulated thermally induced phase mismatch inside a single piece of crystal. Figure 3.9 shows that the efficiency and average 266 nm output power are improved nearly one fold at the highest power input with the new technique compared to the conventional single piece crystal design. The new technique is also able to restore the UV power after laser is cycled off and on, and the beam shape is also greatly improved [29].

Further work is underway to improve the performance of the new technique. Theoretical calculation is important in choosing the correct crystal lengths in order to optimize the 266 nm UV output.

3.4 Sample spectroscopic applications

With such a widely tunable UV/Vis/NIR laser source, many experiments that were previously difficult or impossible can now be pursued. One of the major advantage of a relatively narrow but widely tunable laser source when compared to a white

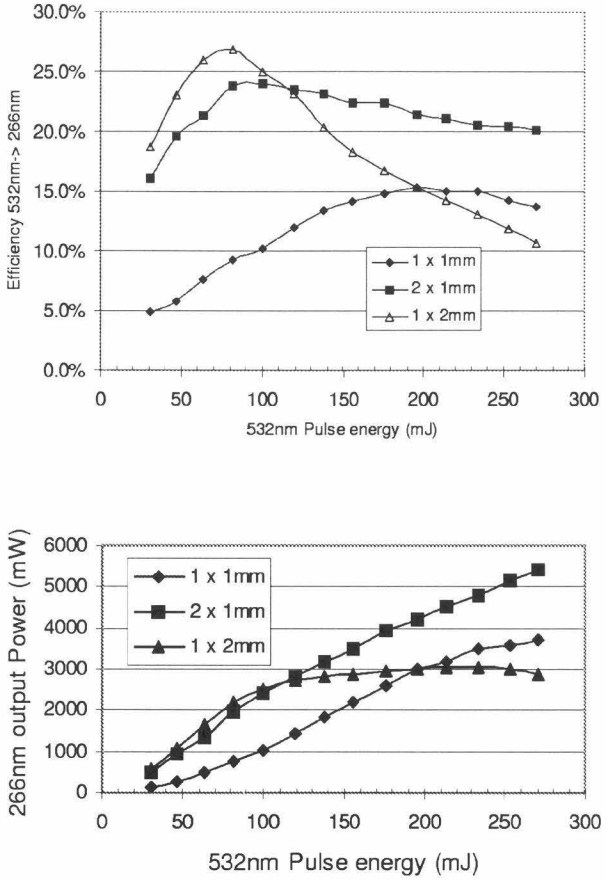

Figure 3.9: The doubling efficiency and average 266 nm UV output is improved significantly with 2 piece of 1mm BBO crystal.

light source (*e.g.*, a deuterium lamp or glowbar), is that the laser's brightness per spectral interval is is orders of magnitude higher than that of white light sources. With a widely tunable OPO, this brightness enhancement can be easily tuned to a wide variety of wavelengths to perform traditional measurements at much better resolution, both spectral and spatial, and dynamic range.

The dynamic range capabilities of an OPO spectrometer are illustrated by the transmission spectra of a dielectric dichroic mirror shown in Figure 3.10. This kind of spectrum is routinely performed with UV-Vis spectrometer to characterize the coating quality. Due to the relatively weak light source inside a traditional spectrometer, however, the highest reflectivity that can be measured by such a transmission spectra is 99.9%. With an OPO source, the reflectivity that can be accurately measured is >99.99%. It is also possible to measure very high absorptivities (up to $OD = 5$) that were previously unobservable with conventional sources, as is shown in the optical garnet spectrum presented in Figure 3.11. With proper electronics and photodetectors, the detection limit can be pushed down to 10^{-7}, as was verified in measurements of the extinction ratio of a Glan-Taylor polarizer.

An OPO similar to the design described above, but pumped at 532 nm, has been used by Wang and coworkers in the lab to generate up to 0.5 mJ/pulse energies from 680 nm to 3000 nm. The 532 nm-pumped type II BBO OPO can be tuned to 3000 nm because the transmission of BBO between 2500 nm and 3000 nm is different for the "e" ray and "o" ray polarizations. The transmission of BBO in unpolarized light has a substantial dip between 2500 nm and 3000 nm, but for polarized light the "e" ray transmission is much better [31]. In the 532 nm-pumped type II BBO OPO, the pump and the idler are both "e" rays, and resonating the "e" ray therefore gives better efficiency and a wider tuning range at the longer idler wavelengths. Figure 3.12 presents results taken between 2000 nm and 3000nm for a topaz thin section through a pinhole only 12.5 μm in diameter. Microsampling spectra beyond this level of spatial resolution cannot be obtained with conventional (*i.e.*, FTS) spectrometers, but are "straightforward" with a widely tunable OPO.

The combination of high sensitivity with a tuning range that covers the optical

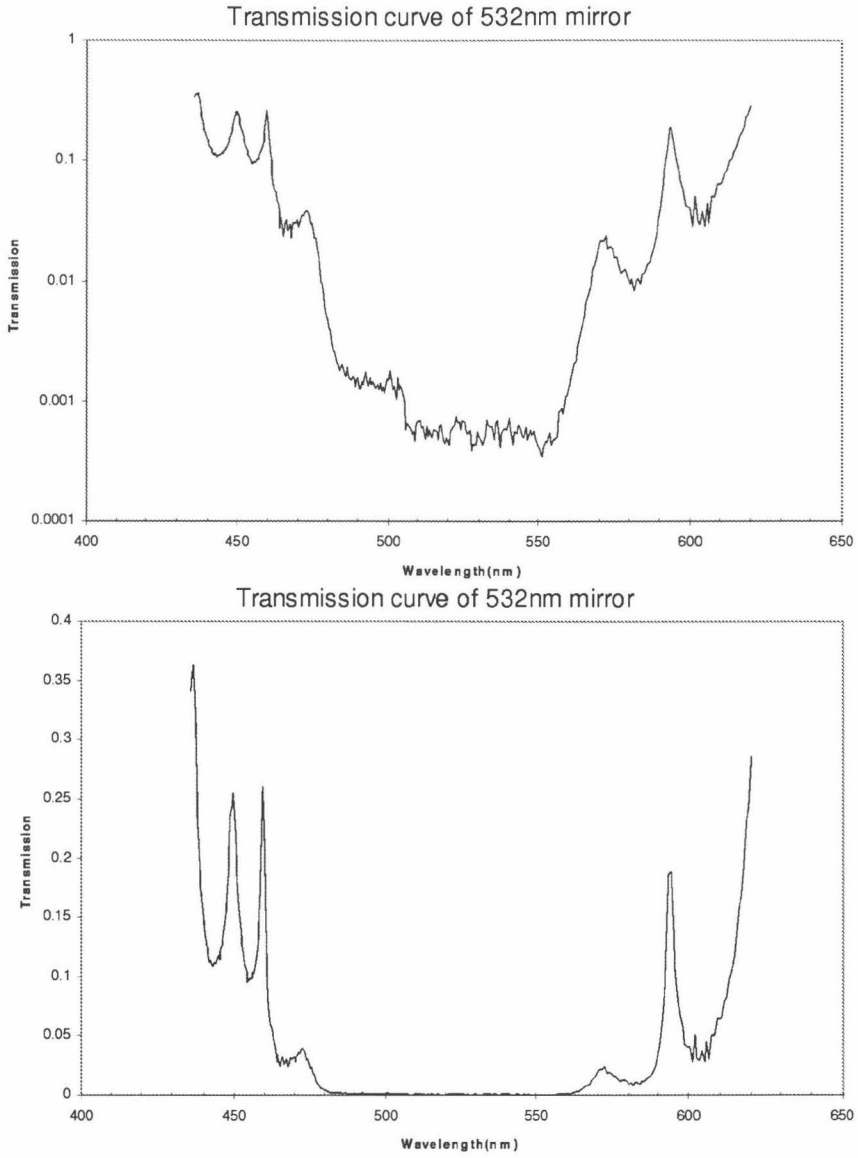

Figure 3.10: Spectra demonstrating the dynamic range limit of the OPO spectrometer. The upper trace is the transmission of a 532 nm dichroic mirror plotted on a normal scale, while the bottom trace is the transmission of the same 532 nm dichroic mirror plotted on a logarithmic scale. Conventional spectrometers yield a plot like the upper one with a transmission detection limit higher than 0.1%.

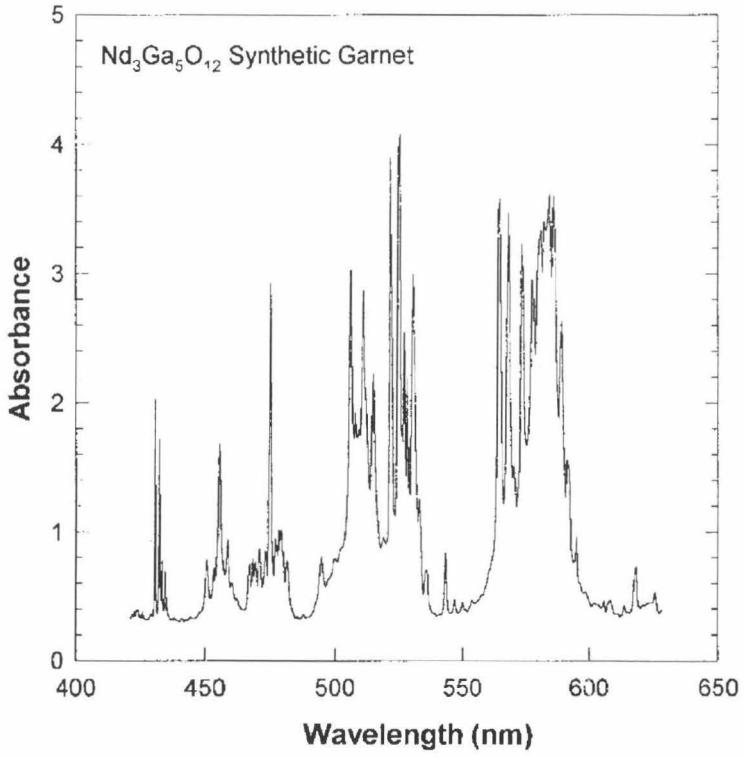

Figure 3.11: OPO absorption spectrum of a synthetic garnet crystal.

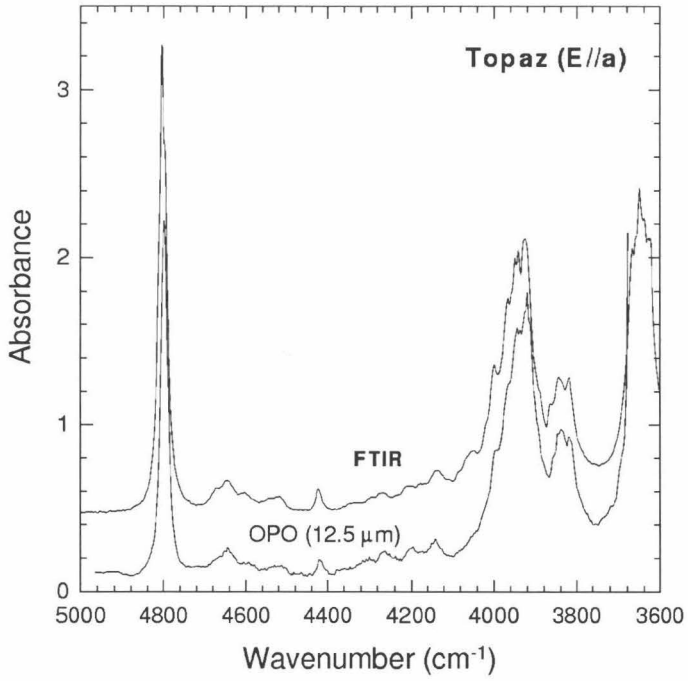

13

Figure 3.12: A comparison of the spectra from an OPO system and one obtained from a commercial FTIR instrument through a 12.5 μm pinhole [32].

and near-IR enable a range of precision diagnostic applications that were previously impossible. The application of OPOs to real world applications presents several challenges, such as the need to reduce the overall system size and to lower the cost. The most cumbersome and expensive component of an OPO spectrometer is the pump laser. Conventional flashlamp-pumped Nd:YAG pump lasers with large beam sizes and pulse energies deliver the kind of pump beam required by *ns* OPOs, and miniaturized versions of such pump lasers are developing rapidly.

Alternatively, laser heads pumped by diode lasers may be considered. The size of a diode pumped laser can be extremely compact, and often does not require cooling water when run at low repetition rates. The electrical power such lasers consume is also low compared to flash lamp pumped versions. These properties have opened many new possible applications for diode-pumped lasers, and wavelength tunable versions will add a great many additional capabilities. At present, the laser pulse energy of diode-pumped Nd:YAG lasers is less than 20 mJ at 1064 nm, and about 3-4 mJ at 355 nm. The divergence is typically 2 mrad or larger, and it is therefore difficult to pump conventional BBO OPOs with such weak and diverging lasers because the acceptance angle of BBO is very small in the sensitive direction (<1 mrad). On the other hand, the acceptance angle in the insensitive direction is nearly 50 times larger. If it were feasible to collimate the pump beam in the sensitive direction, while focussing the pump beam in the insensitive direction, it should be possible to reach the intensity needed for efficient OPO conversion while at the same time satisfying the acceptance angle restrictions. Indeed, we have tested a type I BBO OPO was constructed with such a design, and demonstrated a a low oscillation threshold of only 1 mJ/pulse [35]. Similar initial designs have also worked well with a type II BBO device. Here, a cylindrical lens with a focal length of 200 mm was used in the pump beam path of the same cavity described in this Chapter. The pump beam size was 2 mm in diameter before the lens, and the focal point lay inside the BBO crystal with the beam being focused only in the insensitive direction (ϕ), as is illustrated in Figure 3.13.

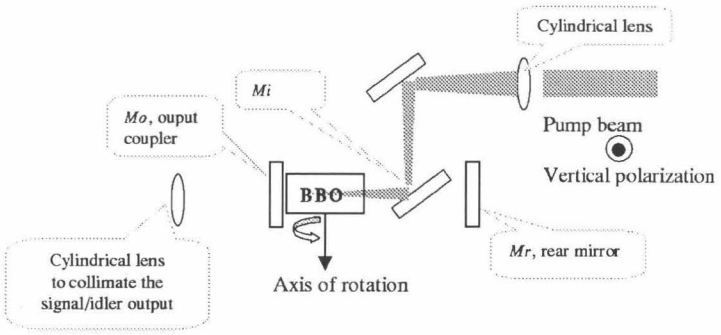

Figure 3.13: A cylindrically focused OPO pumped at 355 nm, whose oscillation threshold is only 1 mJ/pulse. The BBO used in this cavity is of type I BBO with a length of 17 mm.

3.5 Conclusions

Type II phase matched BBO has proven to be a very useful crystal in a widely tunable OPO cavities pumped at 355 nm and 532 nm. With the simple cavity described here, the type II BBO OPO gives good efficiency under moderate pump energy and reasonable linewidths, making the OPO more useful to many experiments. A number of possible improvements have also been proposed and a theoretical model is being developed to assist the further improvements. The basic techniques of extending the OPO radiation into the UV by SHG and SFG processes with type I BBO crystals were also discussed. The problems of two photon UV absorption induced thermal effects in nonlinear optical crystals were described, and a computer simulation model developed to assist the present and future studies.

Bibliography

[1] W. R. Bosenberg, W.S. Pelouch and C.L. Tang, *Appl. Phys. Lett.*, 55 (1989), 1952.

[2] B.C. Johnson, V.J. Newell, J.B. Clark and E.S. McPhee, *J. OPT. SOC. AM. B*, 12 (1995), 2122-2127.

[3] Sheng Wu, Geoffrey A. Blake, Zhaoyang Sun, and Jiwu Lin, *Applied Optics*, 36 (1996), 5898-5901.

[4] L.K. Cheng, W. R. Bosenberg, and C.L. Tang, *Appl. Phys. Lett.*, 53 (1988), 175.

[5] W. R. Bosenberg, L.K. Cheng, and C.L. Tang, *Appl. Phys. Lett.*, 54 (1989), 13.

[6] W.R. Bosenberg and Dean Guyer, *J. Opt. Soc. Am. B*, 10 (1993), 1716-1722.

[7] N.Kroll, *Phys. Rev.*, 127 (1962), 1207.

[8] A. Giordamine and R.C.Miller, *Phys. Rev. Lett.*, 4 (1969), 973.

[9] W.H. Louisell, *Coupled Mode and Parametric Electronics* New York, Wiley, 1960.

[10] W.R. Bosenberg and C.L. Tang, *Appl. Phys. Lett.*, 56 (1990), 1819.

[11] R.L. Byer and S.E. Harris, *Phys. Rev.*, 168 (1968) 1064-1068.

[12] W.R. Bosenberg, A Drobshoff, J.I. Alexander, L.E. Myers, R.L. Byer, *J. Opt. Soc. Am. B*, 12 (1995), 2102-2116.

[13] S.J. Brosnan and R.L. Byer, *IEEE. J. Quan. Elec.*, 15 (1979), 415-431.

[14] W. R. Bosenberg and C. L. Tang, *Appl. Phys. Lett.*, 56 (1990), 1819.

[15] B.J. Orr, *in "Tunable Laser Applications"* edited by F. J. Duarte, Marcel Dekker, 1995

[16] Y.L. Yung and C.E.Miller, *Science*, 278 (1997), 1778 - 1780.

[17] T. Rahn, H. Zhang, M. Wahlen, and G.A. Blake. Stable isotope *GEOP. RES. LETT.*, 25 (1998), 4489-4492.

[18] P.O. Wennberg, R.C. Cohen, N.L. Hazen, L.B. Lapson, N.T. Allen, T.F. Hanisco, J.F. Oliver, N.W. Lanham, J.N. Demusz, and J.G. Anderson.

[19] David Eimerl, *Journal of Quantum Electronics*, 23 (1987), 575.

[20] *OSA Proc. ASSL, ed. B.H.T Chai adn S.A. Payne*, 24 (1995), 223-226.

[21] Y.K. Yap, K. Deki, Y. Kagebayashi, M. Horiguchi, Y. Mori and T. Sasaki em Opt. Lett., 23 (1998), 1016-1018.

[22] H. Kouta and Y. Kuwano, *OSA TOPS* 19 (1998), 28.

[23] R. DeSalvo, A.A. Said, D.J. Hagan, E.W. Van Stryland, and M. Sheik-Bahae, *IEEE. J. Quan. Elec.*, 32 (1996), 1324-1333

[24] Larry Marshall, *Laser Focus World*, 34 (1998), 63

[25] D.T. Hon and H. Bruesselbach *IEEE J. Quan. Elec.*, 16 (1980), 1356-1364.

[26] A. Borsutzky, R. Brunger, and R. Wallenstein, *APPL. PHYS. B* 52 (1991), 380-384

[27] Y.C. Wu, P.Z. Fu, J.X. Wang, Z.Y. Xu, L. Zhang, Y.F. Kong, and C.T. Chen, *OPT. LETT.*, 22 (1997), 1840-1842.

[28] Rodney I. Trickett, Michael J. Withford, and Daniel J. W. Brown *Opt. Lett.*, 23 (1998), 189-191.

[29] S. Wu, G.A. Blake, S. Sun, and J. Ling, *Submitted to Opt. Comm.*

[30] G. Imeshev, M. Proctor, and M.M. Fejier, *Opt. Lett.*, 23 (1998), 673-675.

[31] Data collected with a Perkin-Elmer spectrometer by CASIX, Inc.

[32] Z.F. Wang, G.R. Rossman, and G.A. Blake, *SPECTROSCOPY*, 13 (1998), 44-47.

Chapter 4 A *ns* OPG and OPA system seeded by an external CW diode laser

4.1 Introduction

The type II OPO system described in the previous chapter provides very wide tunability. Although its bandwidth is consistent and can be applied to many spectroscopic experiments, it is still considered to be "too wide" for many spectroscopic studies. For example, theoretical calculations on the structure of alkali metal - small molecule clusters, cannot predict to experimental precision the bond strength or the length of the van der Waals bond between the alkali metal atom and the small molecule. Rotationally resolved spectra recorded with a tunable high resolution laser ($\Delta\nu \approx 0.01$ cm^{-1} resolution) do contain the necessary information. For laser pulses of *ns* duration, an important goal in developing these non-linear optical devices is to develop compact, widely tunable coherent light sources with narrow bandwidth for use in a variety of laboratory, *in situ*, and remote sensing applications. Such studies may often require spectral resolution approaching the transform limit. As described in Chapter 3, while it is possible to design very high resolution free-running OPO cavities, they tend to be inefficient and difficult to tune over long ranges [1],[2]. Injection-seeding an OPO with high resolution lasers forms an alternative approach to achieve high spectral resolution, and has been demonstrated in a wide variety of designs [3]. Transform limited OPGs based on picosecond (ps) [4],[5] and femtosecond (fs) [6], [7], [8] pump lasers have also been designed by several groups. Commercial *ps*- and *fs*-OPGs are now available from several manufacturers, but *ns*-OPGs have not been investigated to date because the non-linear optical drive provided by *ns* pump lasers is typically very low, and one therefore expects that *ns*-OPG thresholds will be high and their efficiencies low. Here, we propose and characterize a novel OPG that is pumped by

a *ns* Nd:YAG laser and seeded by an external single longitudinal mode (SLM) CW diode laser. This new design combines high efficiency and narrow bandwidth with wide tunability and low angular divergence.

4.2 OPG/OPA theory

The OPG is a device based on a nonlinear optical crystal pumped by an intense external field that generates parametric fluorescence from quantum noise [9]. An OPA is the subsequent NLO medium that uses the optical parametric process to amplify the parametric fluorescence from an OPG or any other low power laser source, *e.g.*, the mW of level output of a continuous wave (CW) laser. OPG/OPA theory is relatively simple compared to that for OPO operation, since there is no cavity feedback to consider. From the three wave interaction equations (2.17), (2.18), and (2.17), if the initial intensities, phases, and divergences of the signal, idler and pump waves are specified, it is straightforward to calculate the power, phase and divergence for each of these three waves at any position in the crystal.

We have developed a computer simulation that is based on the plane wave approximation, or equivalently that the beams are far from their Gaussian beam waists. This plane wave model is suitable for most of the nonlinear optical coversion systems of interest, provided the pump laser beam remains collimated as it propagates through the crystal. Wherever strongly focused beams are involved, this model is no longer valid [10].

4.3 A OPG/OPA based on type I BBO crystals

4.3.1 Some design considerations

As pointed out in the first section of this chapter, OPGs based on ns pump lasers have not been studied primarily because the non-linear optical drive provided by a ns pump laser is usually too low, and therefore one expects that the OPG's operational

threshold is high and its efficiency low.

Figure 4.1 compares the pump depletion in an optical parametric generation processes under different levels of pump intensity with type I BBO crystal, calculated with the computer modeling software noted above. In all three plots, the beam divergence is assumed to be zero, and the initial power of the signal and idler fields are 1 mW. The pump laser wavelength is 355 nm, while the signal and idler are chosen to lie at 532 nm and 1064 nm. As Figure 4.1 shows for three different pump intensities — 10 MW/cm^2, 100 MW/cm^2, and 1000 MW/cm^2 — appreciable (10%) pump depletion is not observed until the BBO crystal lengths are exceed 160 mm, 55 mm, and 19 mm!

The three pump intensity levels given above correspond to the typical minimal available pump intensity of ns (10 ns $\rightarrow$ 100 mJ/pulse in a beam area of 1 cm^2), ps (10 ps $\rightarrow$ 1mJ/pulse in a beam area of 1 cm^2) and fs (100 fs $\rightarrow$ 0.1mJ/pulse in a beam area of 1 cm^2) laser pulses. Therefore, it is clear that a typical ns pump laser can be used to pump an OPO, where multipassing of the signal inside the cavity provides sufficient nonlinear drive to achieve reasonable efficiency; while for ps and fs pump lasers, OPG/OPA designs are easy to realize in terms of pump intensity.

On the other hand, OPGs are preferred over OPOs for external seeding by narrow bandwidth light sources such as CW SLM diode lasers. First, an OPG has no cavity and therefore there is no need to actively control the cavity length to match the frequency of the seed laser [11]. Closed-loop servo controls for frequency calibration and tuning are therefore only required for the CW seed laser, which greatly simplifies scanning of the OPG wavelength. Second, OPGs can operate in a single pass fashion, and therefore there is no feedback from the OPG back toward the external seeding or pump lasers. This is important for CW SLM lasers because small amounts of feedback can disturb SLM operation, and under certain circumstances can even damage the gain material. The latter is particularly important when diode lasers are used as the seeding sources [14],[15].

As discussed in Chapter 2, there has been tremendous improvement in ns Nd:YAG performance over the past decade as RVR mirror technology has been combined with

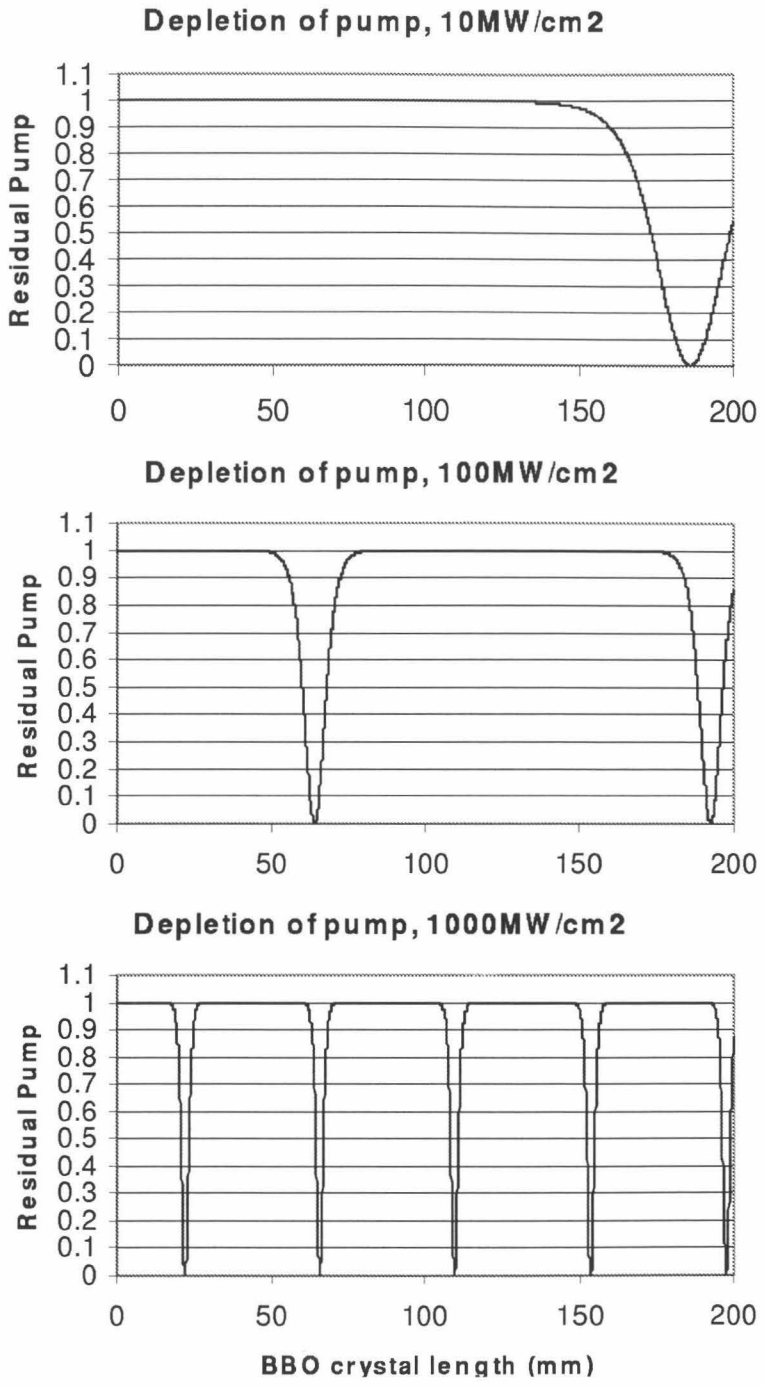

Figure 4.1: Depletion of pump in OPG under different pumping fluence.

efficient utilization of the YAG rod volume; thereby extracting the highest pulse energy while retaining nearly perfect beam profiles. The other major obstacle in very high pulse intensity and repetition Rates is the thermal loading problem, in which the thermal gradient inside the YAG rod causes it to act as a lens. The thermal lensing focuses the laser beam, but can be overcome using a phase-conjugation mirror in the amplification stage.

The Coherent Infinity laser is a good example of these two technologies [20]. The Infinity yields pulses of up to 400 mJ/pulse in a 5.5 mm beam diameter with repetition rates up to 100 Hz. The pulse width is also short, only 3 ns at 1064 nm, which makes nonlinear optical conversion very efficient. For example, up to 180 mJ/pulse of 355 nm light is generated when the the 1064 nm energy is 400mJ/pulse at 100 Hz. With a pulse width close to 2 ns and beam diameter of 5 mm, it is easy to achieve 200 MW/cm^2 with a 100mJ pulse at 355 nm. This about a factor of 4 to 5 higher than any other commercially available *ns* Nd:YAG laser without beam reduction. Recalculating the crystal lengths needed for meaningful OPG operation under such pump intensity, the Infinity is expected to be a promising candidate for *ns* OPG operation. Even so, nearly 50 mm of effective interaction length is needed for type I phase matched BBO crystals in order to achieve a reasonable efficiency level.

4.3.2 Description of the *ns* OPG/OPA

As Figure 4.2 shows [12], the OPG consists of four BBO crystals, arranged in two pairs. Crystals 1 and 2 form the OPG stage, and their optical axes are arranged in such a way that the two crystals counter-rotate with respect to each other as the wavelength is changed. Crystals 3 and 4 also counter-rotate with respect to each other and form an OPA stage which amplifies the OPG output. This widely used counter-rotating design cancels both the "walk-off" effect in non-linear optical crystals and dramatically reduces the output beam position shifts that are generated when the crystals are angle tuned [17]. The signal and idler generated in the OPG stage pass through a pump beam reflecting dielectric mirror and then are directed through a long

Table 4.1: Free-Running OPG/OPA Characteristics

Wavelength Signal / Idler	Parametric Threshold (mJ/pulse)	Efficiency (signal + idler)@120 mJ/pulse	Bandwidth (nm)
435 nm/1921 nm	33	35%	0.2
550 nm/999 nm	31	37%	0.5
630 nm/812 nm	32	35%	2

pass filter which absorbs the signal wavelength generated in the OPG. Therefore the OPA stage is seeded only by the idler beam. This idler-seed OPA design maintains a small angular divergence for the overall OPG/OPA output, as will be demonstrated in the test results described below.

Pump pulses are provided by the third harmonic (355 nm) output from a Coherent Infinity 40-100 pulsed Nd:YAG laser. The Infinity delivers pulses of 2.5 ns width at 355 nm, with 0-160 mJ pulse energy at repetition rates from 0 to 100 Hz. The beam is circular, approximately 5 mm in diameter, and has a flat-top intensity profile. As noted above, the OPG/OPA gain media consists of four type I BBO crystals, cut at $\theta = 30°$ and coated with a protective AR coating. Crystals 1 and 2 are 10 mm in length each, while crystals 3 and 4 are 17 mm in length. The pump beam is directed into the OPG/OPA layout without prior collimation or focusing.

The initial series of tests characterized the free-running OPG/OPA's tuning range, parametric threshold, and efficiency. Table 4.1 lists the parametric thresholds and conversion efficiencies at three different wavelengths. The OPG/OPA setup is capable of tuning from 410 nm to 2400 nm without gaps. The efficiency and the parametric threshold are rather constant over the signal tuning range from 435 nm to 700 nm (idler from 1920 nm to 720 nm), but the efficiency drops and the threshold rises steeply when the OPG/OPA is tuned to signal wavelengths below 435 nm. This is due primarily to infrared absorption by the BBO material at idler wavelengths greater than 2 μm. The bandwidth of the OPG/OPA is very close to that of a type I OPO [2], and can be as small as 0.1 nm at deep blue (430 nm) signal wavelengths, but rises quickly to several nm as degeneracy (710 nm) is approached.

The angular divergence of the signal wavelength was measured at 630 nm with

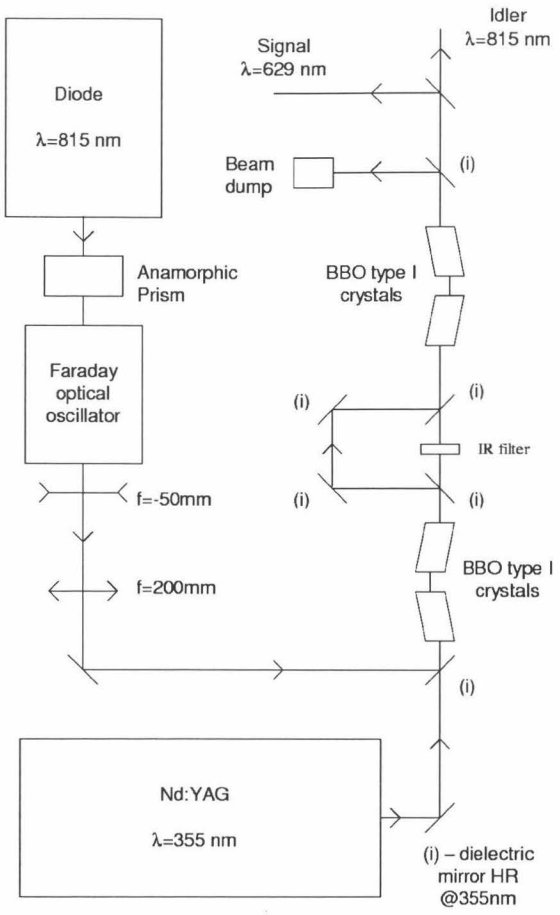

Figure 4.2: An outline of the diode laser injection-seeded ns-OPG/OPA. The pump steering mirrors are standard 355 nm dielectric Nd:YAG mirrors, and combine high reflectivity at the pump wavelength with good transmission of the signal and idler beams. The filter (Schott RG710) selectively absorbs only the signal radiation, leading to seeding of the OPA stage by the idler output of the OPG [12].

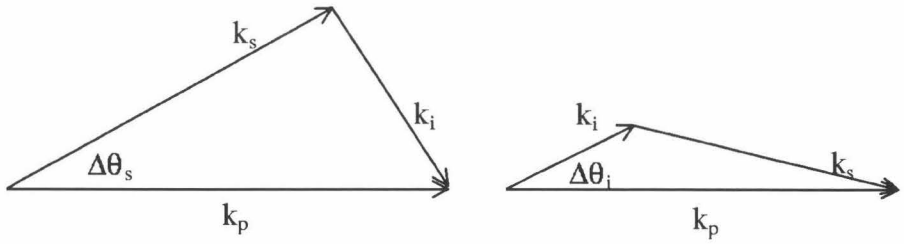

(a) (b)

Figure 4.3: (a) If the signal wave is used as the seed, a much larger divergence occurs for the idler, which in turns results in large beam divergence for the final signal output of the OPG. (b) Using idler as the seed provides a much smaller divergence for the signal ouput after amplification.

the long pass filter removed. The divergence was found to be nearly 6 mrad, showing that the output of the OPG/OPA was expanding rapidly. With the the long pass filter reinstalled, the signal beam angular divergence was reduced to roughly 2 mrad, much smaller than that without the filter. The efficiency of the OPG/OPA was nearly identical with or without the filter. This clearly demonstrates the importance of using only the idler as the seed for the amplifier stage, as is shown graphically in Figure 4.3. A type I BBO will have about the same angular acceptance at signal and idler wavelengths ranging from 410-2400 nm, and the angular divergence of the OPG output at both signal and idler wavelengths is dictated by this angular acceptance. Since the signal wave vector, k_s, is always larger than idler wave vector k_i, and since (k_s and k_i) emerge from the OPG stage with the same angular divergence, it is easy to understand that by using the idler as the seed for the OPA stage, signal beams with much smaller beam divergence will result. This same principle applies to OPO design as well, and is consistent with the discovery that resonating the idler part of the parametric output gives a much smaller OPO angular divergence than can be achieved by resonating the signal wavelength described in Chapter 3 [21].

The high efficiency of the OPG/OPA is a direct result of the characteristics of the pump laser. The Infinity 40-100 has a pulsewidth of only 2 ns, less than half of the pulse width of a typical flashlamp-pumped, Q-switched Nd:YAG lasers at 355 nm. The beam size is rather small and has a divergence only 1.5 times the diffraction limit. The Rayleigh distance is thus nearly two meters, resulting in peak power densities in excess of 200 MW/cm^2 at pump energies of roughly 100 mJ/pulse. This power density can be maintained over a long distance and approaches the operating conditions of many ps OPG/OPA systems [4], [5].

4.3.3 Seeding the free running *ns* OPG/OPA

Despite the high efficiency and excellent beam quality, the spectral output of ns-OPG/OPA is quite broad, especially at wavelengths near degeneracy. This is useless for most spectroscopy experiments. Injection seeding with a CW laser source was

tested to overcome this problem. A CW single longitudinal mode (SLM) diode laser (EOSI Model 2001, now part of the Newport Corportion product line) was used as the seed laser. When properly adjusted, the 810 nm diode laser is capable of SLM operation over a tuning range of over 10 nm without mode hops. The output of the diode laser passes through an anamorphic prism pair, an optical isolator, and a mode-matching telescope before being directed to the OPG/OPA. Once the wavelength of the diode laser is matched with the OPG/OPA operating wavelength seeding is easily achieved. The seeded OPG/OPA has a beam divergence of only 0.5 mrad, which is much smaller than that of the free-running device. This is attributed to the small angular divergence of the collimated diode laser beam.

We next measured the locking range of the OPG/OPA. The idler output was fixed at 815 nm, and the EOSI 2001 laser was scanned through the OPG/OPA wavelength. At the same time the seeded pulse energy was measured in the mid-field ($\approx$3 m after the final OPA crystal) with a 6 mm diameter iris placed in front of an average power thermopile. The results of this locking range test are presented in Figure 4.4, from which the continuous tuning of the diode laser wavelength is seen to be >20-30cm^{-1} at 815 nm (signal = 628 nm) without having to adjust the crystal orientation.

The CW power required in order to seed the OPG/OPA was also Measured by increasing the seeding power from zero while simultaneously measuring the seeded pulse energy with the arrangement described above. The results of the seeding power experiment are presented in Figure 4.5. Clearly, the OPG/OPA requires <6mW of CW seed input to operate at peak efficiency. In the current configuration, the polarization of the diode laser after leaving the isolator is rotated by 45 degrees from the OPG/OPA optical axis, leading to a 3 dB insertion loss. Similar results were obtained when the signal radiation is used to seed the OPG, for example with a HeNe laser at 632 nm. Thus, with the properly configured optics any external seed laser operating between 410 - 2400 nm with just a few mW of power will be able to seed the OPG/OPA robustly.

The bandwidth of the OPG/OPA output was measured with a pulsed spectrum analyzer (Burleigh PLSA 3500). The full width at half maximum (FWHM) of the

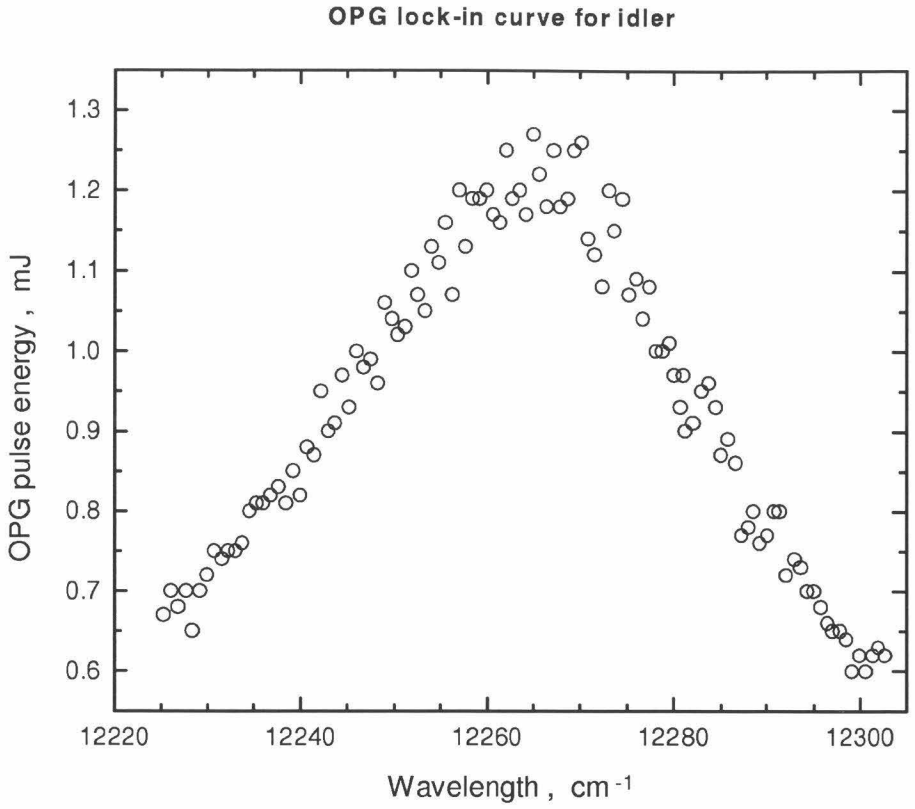

Figure 4.4: OPG/OPA output versus seed laser frequency for a fixed BBO crystal orientation. The FWHM of the pulse energy enhancement by the seeding field is approximately 20-30 cm^{-1}.

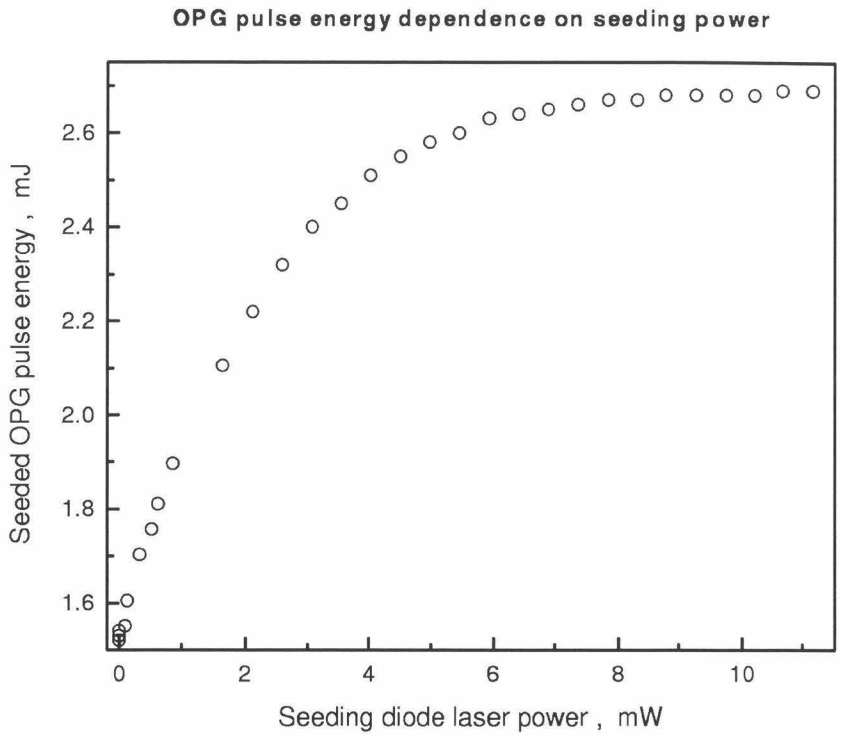

Figure 4.5: OPG/OPA Output versus CW seed power.

OPG/OPA is found to be 650150 MHz, as the spectrum in Figure 4.6 shows. The pump laser always operates under SLM conditions which has a bandwidth of roughly twice the transform limit, or <250 MHz, at 1064 nm. The pump laser therefore has a bandwidth (FWHM) of approximately 600 MHz at 355 nm. The pulsewidth of the OPG/OPA output is always shorter than the pump pulse, thus the bandwidth of the OPG/OPA will be somewhat larger than the pump bandwidth at 355 nm.

Finally, we have recorded a photoacoustic spectrum of the 3rd overtone of the OH stretch in water near 815 nm. This was done to demonstrate the continuous tunability of the OPG/OPA and to check its bandwidth. A portion of the photoacoustic spectra of water taken with the idler output is presented in Figure 4.7. The individual absorption features in this spectrum have a FWHM of 0.07 cm^{-1}, which is much larger than the measured bandwidth of the OPG/OPA output on the pulsed spectrum analyzer. The spectral linewidths are caused primarily by a combination of pressure and Doppler broadening. For the conditions under which the spectra were acquired (1 torr of water vapor in 500 torr of nitrogen), the intrinsic linewidth of the water absorption features is on the order of 0.05 cm^{-1}. Convolution of the molecular linewidth with the total observed linewidth yields an estimate of 600 MHz for the OPG/OPA linewidth, which is in agreement with the pulsed etalon measurements.

4.3.4 The signs of d_{eff} in the OPG/OPA design

In the above OPG/OPA design, two pairs of 2 type I BBO crystals arranged in a counter rotating fashion. Here, it is also instructive to investigate the sign of the d_{eff} as was done for the type II BBO OPO.

Figure 4.8 it can be seen that for a type I BBO crystal there is always a way to properly rotate the BBO crystal such that both counter rotation and a correct sign of d_{eff} can be achieved at the same time. This proper orientation of the two counter rotating BBO crystals is important in achieving high efficiency and stable beam pointing. With an incorrect orientation a 50% drop in efficiency is observed, and the laser beam pointing directions of the signal and idler are different. Indeed,

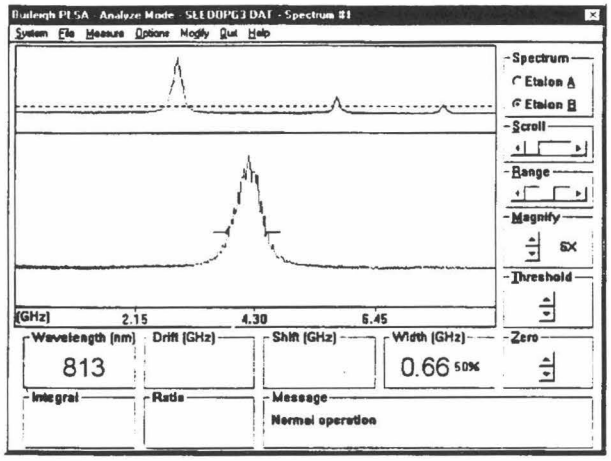

Figure 4.6: Spectral bandwidth of the seeded *ns*-OPG/OPA idler output as measured by a Burleigh PLSA 3500 pulsed spectrum analyzer.

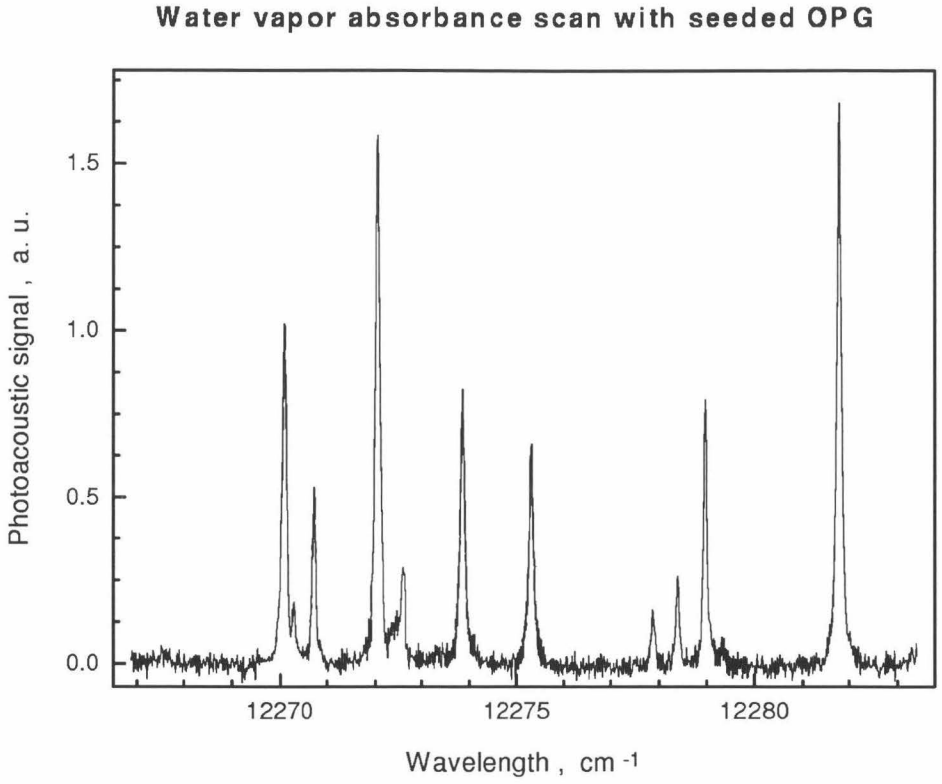

Figure 4.7: Photoacoustic absorption spectrum of the third O-H stretch overtone of water near 815 nm. The photo-acoustic cell contained 1 torr of water vapor in a 500 torr bath of dry nitrogen. The measured FWHM of the individual features is 0.07 cm^{-1}, and is dominated by a combination of pressure and Doppler broadening.

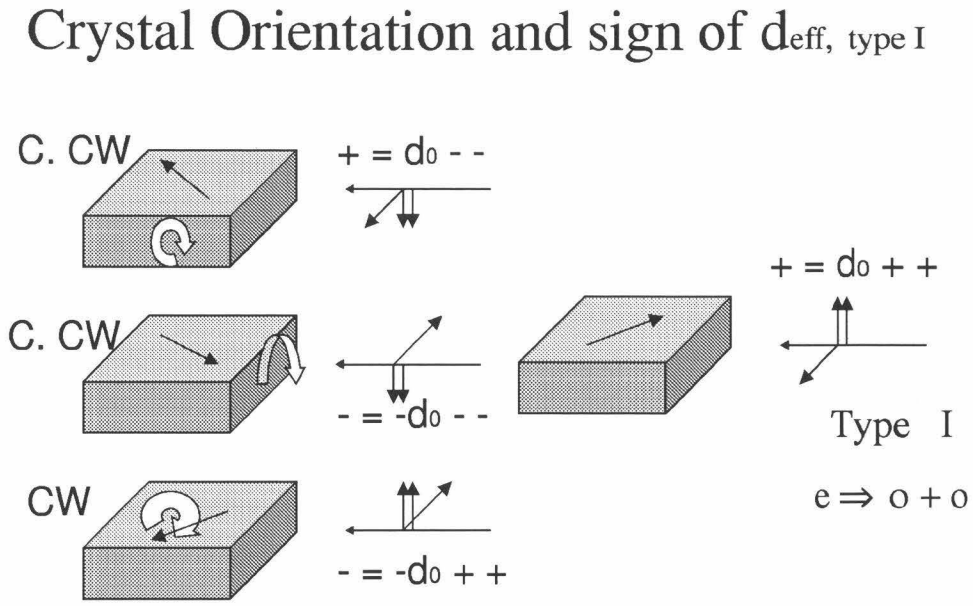

Figure 4.8: An illustration of how the sign of d_{eff} changes under different crystal orientations. The first orientation satisfies the counter rotation needs while providing the same sign in d_{eff} for type I phase matched BBO.The two short arrows stand for the two lower energy photons, *i.e.*, signal and idler; while the long arrow stands for the higher energy photon, *i.e.*, pump.

they are separated by 5 mrad in the insensitive direction, indicating the amplified signal is not collinearly phase matched with the pump beam.

4.4 Other similar devices

The above OPG/OPA design provides a very simple way of generating a very narrow linewidth laser. It is desirable to extend this design to other parametric systems. The following discusses the choice of pump laser and nonlinear optical materials that will yield reasonable conversion efficiencies.

The efficiency of an OPG/OPA device depends on the peak pump intensity and the nonlinear optical material length and d_{eff}. It is convenient to introduce a nonlinear drive parameter, η_0, as a characteristic value in judging these three factors, or

$$\eta_0 = C^2 L^2 I_p(0) \quad , \tag{4.1}$$

where

$$C^2 = \frac{8\pi^2 d_{eff}^2}{n_i n_s n_p \lambda_s \lambda_i c \varepsilon_0} \quad . \tag{4.2}$$

L is the crystal length, and s, i and p are signal, idler and pump waves, respectively.

There is an analytical solution for the three wave interaction for the OPG/OPA process using the small depletion approximation, which yields

$$I_s(l) = I_s(0)\cosh^2[\Gamma_0^2 - (\delta k/2)^2]^{1/2} l \tag{4.3}$$

$$I_i(l) = (\omega_i/\omega_s) I_s(0)\sinh^2[\Gamma_0^2 - (\delta k/2)^2]^{1/2} l \tag{4.4}$$

$$I_p(l) = I_p(0) \tag{4.5}$$

Given a small efficiency and $\Delta k = 0$, the intensity of the signal can be characterized as

$$\ln(I_s(l)/I_s(0)) \simeq \eta_0 = \frac{8\pi^2 l^2 I_s(0) I_p(0) d_{eff}^2}{n_i n_s n_p c \varepsilon_0} \tag{4.6}$$

If the OPG threshold is chosen to be a measurable amount of energy (for example, 0.001 mJ/pulse for ns pulses in beam size of 1 cm^2, or 1 kW/cm^2 peak power density) at the seeded wavelength and the initial CW seed power is of order 1 mW, then the nonlinear drive must be greater than $I_{s,i}(1)/I_{s,i}(0) = 10^6$.

With this requirement, certain crystal/pump laser combinations can be examined in order to determine if they can be used in efficient OPGs and OPAs. Note the peak power density of the pump cannot be arbitrarily increased by down collimating the pump laser beam size because the peak power density is limited by the damage threshold of the NLO material. In addition, the acceptance angle of the crystal will also limit the tolerable divergence of the pump beam.

One example of the usefulnes of this criteria is an analysis of a PPLN OPG system pumped by a high repetition rate, low pulse energy diode-pumped laser. The d_{eff} of PPLN is about 14 pm/V, which is nearly 7 times larger than that for type I BBO crystals (for which $d_{eff} = 1.7$pm/v at $\theta = 30$). The acceptance angle of PPLN is also very large, and is primarily limited by the Rayleigh distance of the beam. Together, these factors translate into a increase of nonlinear drive of $\approx$50 for unit power density and interaction length. PPLN wafers as long as 20 mm can easily be fabricated, and its damage threshold is about 100 MW/cm^2. Using these values, a power density of only 10 MW/cm^2 is needed to generate a 1% efficiency OPG with a 20 mm long PPLN crystal. Compared to PPLN, BBO pumped at 355 nm would need about 100 MW/cm^2 to start the OPG process. Typical diode-pumped high repetition rate, low pulse energy pump lasers can produce up to 100 μJ/pulse in a 10 ns pulse width, or peak powers of 10 kW if the beam is focused to a 100 μm spot size. Thus, the available 125 MW/cm^2 peak power density should be enough to operate the OPG, and in fact the pump energy would need to be lowered in order to avoid optical damage. An OPG based on a PPLN crystal with a diode-pumped high repetition rate, low pulse energy pump laser is therefore an excellent candidate to generate narrow bandwidth, high repetition pulses in the IR (1.5-4μm) region. In fact, a similar device based on bulk $LiNbO_3$ crystal has recently been reported, and the output power should be readily scalable [25].

Bibliography

[1] T.K. Minton, S.A. Reid, H.L. Kim, and J.D. McDonald, *Opt. Commun.*, 69 (1989), 289-293.

[2] B.C. Johnson, V.J. Newell, J.B. Clark, and E.S. McPhee, *J. Opt. Soc. Am. B*, 12 (1995), 21222-21227.

[3] J.E. Bjorkholm and H.G. Danielmeyer, *Appl. Phys. Lett.*, 15 (1969), 171-173.

[4] H.J. Krause and W. Daum, *Appl. Phys. B.*, 56 (1993) 8-13.

[5] J.Y. Zhang, J.Y. Huang, Y.R. Shen, and C.T. Chen, *J. Opt. Soc. Am. B*, 10 (1993), 1758-1764.

[6] D.C. Edelstein, E.S. Wachman, and C.L. Tang, *Appl. Phys. Lett.*, 54 (1989), 1728-1730.

[7] R. Laenen, H. Graener, and A. Laubereau, *Opt. Lett.*, 15 (1990), 971-973.

[8] O. Kittelmann, J. Ringling, G. Korn, A. Nazarkin, and I.V. Hertel, *Opt. Lett.*, 21 (1996), 1159-1161.

[9] R.L. Byer and S.E. Harris, *Phys. Rev.*, 168 (1968), 1064-1068.

[10] A. Yariv, *Quantum Electronics*, 3rd ed., New York, John Wiley & Sons, 1989.

[11] O. Votava, J.R. Fair, D.F. Plusquellic, E. Riedle, and D.J. Nesbitt, *J. Chem. Phys.*, 107 (1997), 8854-8865.

[12] S. Wu, V.A. Kapinus, and G.A. Blake, *Opt. Comm.*, 159 (1999), 74-79.

[13] D.C. Hovde, J.H. Timmermans, G. Scoles, and K.K. Lehmann, *Opt. Commun.*, 86 (1991), 294-300.

[14] M.J.T. Milton, T.D. Gardiner, G. Chourdakis, and P.T. Woods, *Opt. Lett.*, 19 (1994), 281-283.

[15] P. Bourdon, M. Pealat, V.I. Fabelinksy, T.D. Gardiner, G. Chourdakis, and P.T. Woods, *Opt. Lett.*, 20 (1995), 474-476.

[16] A. Fix, T. Schroder, J. Nolting, and R. Wallenstein, *Appl. Laser Spec., edited by W. Demtroder and M. Inguscico*, 101 (1990), Plenum, New York.

[17] C.L. Tang, W.R. Bosenberg, T. Ukachi, R.L. Lane, and L.K. Cheng, *Proc. IEEE.*, 80 (1992), 365-374.

[18] Y.X. Fan, R.C. Eckhardt, R.L. Byer, C. Chen, and A.D. Jiang, *IEEE J. Quantum Elec.*, 25 (1989), 1196-1199.

[19] D.E. Withers, G. Robertson, A.J. Henderson, T. Yan, C. Yong, W. Sibett, B.D. Sinclair, and M.H. Dunn, *J. Opt. Soc. Am. B*, 10 (1993), 1737-1743.

[20] *OSA Proc. ASSL, ed. B.H.T Chai adn S.A. Payne*, 24 (1995), 223-226.

[21] S. Wu, G.A. Blake, Z. Sun, and J. Ling, *Appl. Opt.*, 36 (1997), 5898-5901.

[22] A. Fix, T. Schroder, R. Wallenstein, J.G. Haub, M.J. Johnson, and B.J. Orr, *J. Opt. Soc. Am. B*, 10 (1993), 1744-1750.

[23] F. Huiksen, A. Kulcke, D. Voelkel, C. Lausch, and J.M. Lisy, *Appl. Phys. Lett.*, 62 (1993), 805-807.

[24] M. Tsunekane, M. Ihara, N. Taguchi, and H. Inaba, *IEEE J. Quan. Elec.*, 34 (1998), 1288-1296.

[25] M. Seiter and M.W. Sigrist, *Opt. Lett.*, 24, (1999), 110-112.

Chapter 5 Experimental Methods

5.1 Introduction

Experimental studies of small molecule - alkali metal neutral and cation clusters involve three general steps: producing the clusters, verifying the existence of the clusters, and, finally, acquiring spectra of the clusters. Each step is described more fully below. Briefly, the clusters were formed by crossing a supersonic jet expansion of the appropriate small molecule gases (*e.g.*, NH_3, H_2O and C_6H_6) with a plume of laser ablated alkali metal atoms. The existence of the alkali-containing clusters was verified by single photon threshold photoionization through the alkali atom chromophore in the source region of a time-of-flight mass spectrometer (TOFMS). Zero Electron Kinetic Energy-Pulsed Field Ionization (ZEKE-PFI) spectroscopy was also applied to clusters where the such signals could be observed. ZEKE-PFI spectroscopy can be used to determine the intermolecular vibrational modes of the ionized clusters, which are the spectroscopic features of most direct relevance to biological and geochemical processes. Since all three steps demand a vacuum environment, the clusters were formed and studied in a differentially-pumped vacuum apparatus comprised of three chambers. The cluster formation and detection schemes closely follow those of Rodham [1], and additional details concerning both ZEKE-PFI and REMPI approaches to the intermolecular force fields of alkali-small molecule clusters may be found therein.

5.2 Cluster formation and identification

5.2.1 Cluster formation

Due to their instability at room temperature, the weakly-bound clusters were formed in a supersonic jet expansion (SJE) [2, 3]. A SJE is created as a gas expands from a high pressure reservoir into vacuum through an nozzle having a diameter much larger than the mean free path of the gas molecules in the reservoir. Typically, the molecule of interest is seeded in a rare gas carrier such as argon or helium. As the gas expands, the molecules experience many collisions over a short distance from the nozzle orifice where internal molecular energy is converted to translational energy. Translational cooling is achieved because the molecules in the SJE have a very narrow velocity distribution once they reach the collisionless regime. Cooling of the molecular internal degrees of freedom enhances aggregation, and clusters which would be unstable at room temperature can be formed. Besides providing an intense cluster source, SJEs also offer an isolated, low-temperature environment in which molecular spectra are greatly simplified.

The SJE formed in the source chamber was skimmed by a 4 mm diameter skimmer (Beam Dynamics) 5-10 cm downstream of the nozzle, creating a collimated cluster beam in the probe chamber where the clusters were ionized. The ZEKE-PFI apparatus was contained in this chamber, to which was attached the third chamber, the flight tube of the TOF.

5.2.2 Cluster identification with the TOFMS

Laser-ionization TOF mass spectrometry was used to verify the existence of the clusters in the molecular beam. Single-photon ionization was used for the clusters. The TOFMS was also crucial in isolating the threshold ionization spectra of these clusters in a mass-specific fashion.

The TOFMS was a commercial angular reflectron [4, 5] instrument from R.M. Jordan Co. Two ion detectors are provided, the frist being a microchannel plate

(MCP) detector at the end of the 1.1 m flight tube for use as a standard TOFMS, the second being located at the secondary ion focus of the reflectron mode (which was typically not needed for the experiments reported here). A Wiley-McClaren ion source [6], located 30 cm from the pulsed nozzle, was used to achieve spatial and temporal focusing. A 4 mm x 1 mm skimmer (Beam Dynamics) placed just before the ion source created a narrow strip of clusters between the extraction grids and limited the amount of gas entering the TOF. The extraction field of 315 V/cm and the acceleration field of 3000 V/cm were obtained by holding the repeller plate at 4200 V and the extraction grid at 3800 V. The Einzel lens inside the ion source region optics was not used. The MCP detector was operated at a voltage of 1800 $\pm$ 300 V, depending on the signal strength.

A set of V(XY) deflector plates was used to compensate for the initial velocity of the cluster beam, which is orthogonal to the TOFMS beam path, to ensure the ions strike the MCP detector. For molecules traveling at molecular beam speeds, large ions with long flight times will travel farther along the molecular beam direction (perpendicular to the TOF in this case) while in the flight tube than will small ions and may therefore miss the detector. For the alkali metal - small molecule clusters in an argon expansion, V(XY) = 10-150 V worked best. The output signal from the detector was sent to an EG&G 9301 preamplifier ($\times$10 gain) and from there to a LeCroy 9400A 100 MHz digital storage oscilloscope (DSO).

5.2.3 Vacuum apparatus

Each chamber was pumped by a diffusion pump (DP), and all three diffusion pumps were backed by a single Edwards EM2-275 mechanical pump. The source chamber was pumped by a Varian VHS-10 DP with a water-cooled baffle, the probe chamber by an H_2O-baffled Varian VHS-6 DP, and the TOFMS by an unbaffled Edwards DIFFSTAK 100 DP. When the nozzle was operated at 30 Hz, the typical operating pressures in the source, probe, and TOF chambers were 5×10^{-5} Torr, 5×10^{-7} Torr, and 5×10^{-8} Torr, respectively. The roughing line was 4″ i.d. stainless steel pipe

which ran from the roughing pump to the 10″ DP, and 2″ PVC pipe was connected from that point to the other DP outlets. Pneumatic gate valves were placed between the chambers and their DPs. To protect the chambers, an interlock system was used to turn off the DPs and close the gate valves in the event of excessive pressure or loss of cooling water to the DPs, as described in [1].

5.3 Experimental methods used to study alkali metal cation - small molecule clusters

5.3.1 ZEKE-PFI spectroscopy

ZEKE-PFI spectroscopy was used to obtain the intermolecular vibrational frequencies of certain alkali metal cation (Na^+/K^+)- small molecule clusters. The ability of ZEKE-PFI spectroscopy to produce high resolution spectra of molecular and cluster ions is well documented [16, 17, 18, 19].

ZEKE-PFI spectroscopy, as it is understood today, is based on the unanticipated discovery that most neutral molecules under vacuum have extremely long lived Rydberg states at energies slightly below the corresponding ionization threshold [17]. Even more unexpected was the finding [15] that these long lived states persist high into the ion continuum, thereby forming "islands of stability" far above the ionization energy (IP) for each of the ion states to which the Rydberg series converge.

The physics behind ZEKE-PFI spectroscopy is beginning to be unravelled [20, 21], and a self consistent mechanism established [22]. It involves optical pumping to Rydberg states at very high prinipal quantum numbers (denoted n, where $n > 100$) but low electron angular mommenta (denoted l, with $l \approx 0$) in the presence of a small electric field. The inhomogeneous field, which can be externally supplied or generated by ions in the molecular beam, leads to l-mixing of the high-n states [23] to produce high-n, high-l states. Viewed semi-classically, the orbits of these high-(n,l) electrons cannot be accessed directly by photoexcitation since they are well removed from the ion core and "communicate" with it very poorly. This appears to be the origin of the

effect leading to the long-lived, but optically inaccessible, Rydberg states which have been termed ZEKE states.

After a delay of some 1-3 μs (or even longer in certain experiments) during which prompt electrons exit the extraction region, a small voltage is applied to one extraction plate, thus creating an electric field which ionizes the ZEKE states and accelerates the ZEKE-PFI electrons toward a MCP detector. When properly configured, the excitation/ZEKE pulse sequence gives nearly zero-background detection of the threshold photoelectrons.

In the actual experiment, the region where Rydberg state molecules/clusters are generated is always not field free, *i.e.*, there are stray fields present in the region where the excitation laser crosses the molecular beam. These stray fields immediately field ionize any high Rydberg state molecules/clusters, leaving them undetectable by subsequent PFI sequences. This creates a shift of the Ionization Potential (IP) between the real value (or field free value) and that actually measured. One way to correct for this shift is to vary the stray field, and measure the shift of IP at the same time. By plotting a curve of measured IP v.s. stray field, and by extending the stray field toward zero, an accurate, field free, IP can be obtained.

In the ZEKE-PFI experiments reported here, high-n Rydberg states of the alkali atoms in the clusters were populated by single-photon excitation using tunable UV light. Two-color excitation through a resonate intermediate state, with detection occurring either via Resonance Enhanced Multi-Photon Ionization (REMPI) or ZEKE-PFI can give access to states that are not reachable by single-photon excitation. In addition, REMPI offers the opportunity to prepare the clusters in a single specified quantum state, provided the intermediate state has a sufficiently long lifetime and that first excitation photon has a narrow enough bandwidth. The excitation of a single rovibrational level in the intermediate electronic state would permit detailed structural data (bond length, and dissociation energy, etc.) to be acquired not only for the ground and intermediate state of the neutral cluster, but also those of the cation cluster. The latter is not feasible for single photon ZEKE-PFI experiments on molecules similar to those of even the smallest cation clusters of interest

here due to their small rotational constants (the B rotational constant of $Na(NH_3)_1$ is $< 0.25cm^{-1}$, for example).

Multi-photon studies of this type were a major motivation for developing the single frequency CW diode laser seeded OPG/OPA system described in Chapter 4. While preliminary experiments on clusters composed of one Na atom and one small molecule, *e.g.*, $Na(NH_3)_1$, have produced spectra revealing some rotational structure, instabilities in the cluster source as we described below and freqeuncy drifts of the CW seed laser have prevented a complete rotational assignment at this time. Furthermore, REMPI studies of the $K(NH_3)_1$ cluster intermediate electronic states gave extremely complex spectra. It is known that for higher order clusters in $Na(NH_3)$ that internal cluster reactions of the excited electronic states are sub-ps in nature [26], and the K-containing clusters may be even more reactive. Thus, further improvements in the experimental technique are required, and various possibilities will be discussed later in this thesis.

5.3.2 The pick-up source

Since alkali metals are quite reactive and have low vapor pressures, they cannot be co-expanded with small molecules such as water or ammonia from the same reservoir. The clusters of alkali metal atom - small molecules were therefore formed in a "pick-up" source, a variant of that used by Hertel and coworkers [25, 26]. A SJE containing either pure NH_3, or H_2O or benzene seeded in Ar, was crossed by an plume of alkali metal atoms generated by laser ablation on an alkali metal sample holder. Collisions entrained the alkali atoms in the SJE, where a small fraction of them formed clusters. The alkali metal sample holder, which holds pressed alkali metal in an exposed area some 12 mm in diameter, was placed 5 mm below and 5 mm downstream of the orifice of the pulsed valve (General Valve, series 9, high temperature version, 0.8 mm nozzle diameter). A drawing of this source is shown in Figure 5.1. A solenoid valve (General Valve) was used instead of a piezoelectric valve often used by the group because heating of the valve, which is required for H_2O, caused it to perform poorly.

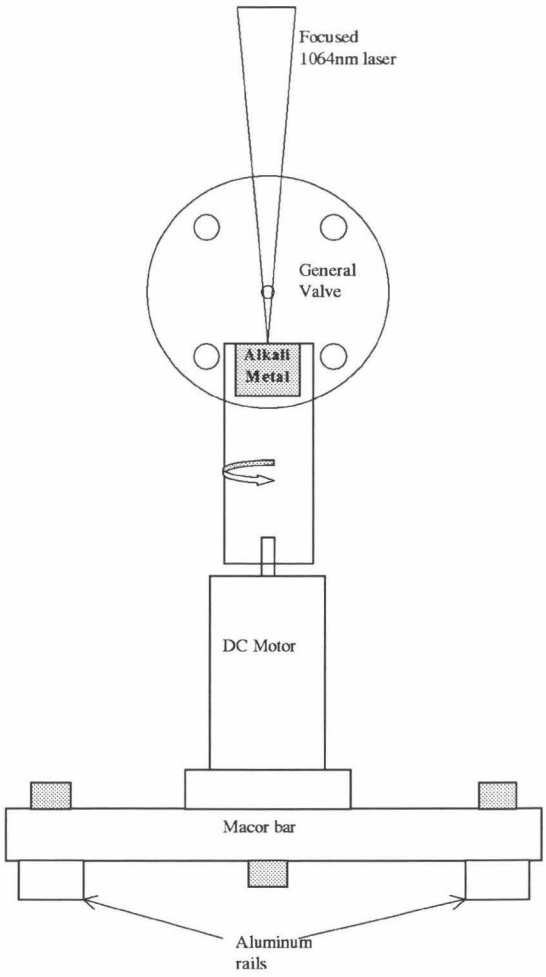

Figure 5.1: A schematic of the alkali cluster laser vaporization/pick-up source. The heating blocks are shown in a "cut away" fashion to expose the sodium oven and the cartridge heaters..

Clusters with water were formed by expanding ~1 atm. of water vapor (from a water reservoir held at 100° ± 10° C) with ~ 1.5 atm. of argon carrier gas, while clusters with ammonia were formed by expanding 3 atm. of ammonia neat. For these expansion gas mixtures, optimum cluster signal was obtained by minimizing the flow through the pulsed valve. This was done by keeping the voltage applied to the valve as low as possible. The number of 1:1 clusters ionized per laser shot was ~100.

As described in Rodham [1], for clusters with water, the argon carrier gas was passed through a water reservoir behind the General Valve. The reservoir and valve were independently heated, with the valve being kept hotter than the reservoir. The temperatures were maintained by Omega Engineering temperature controllers (model CN76133). The cartridge heater for each heating block was connected to a controller via an electrical feedthrough, and a chromel-alumel thermocouple was attached to the block, with its wires connected to the temperature controller via a thermocouple feedthrough. The cycle of the controller should be set to be as short as possible, and the temperature climb rate should be limited (the default value is infinity) to prevent overheating. Overheating the water will result in water droplets directly entering the chamber, and these droplets will either react with the alkali metal or increase the backing pressure of the chamber to untolerable values. The carrier gas tubing leading into the reservoir was Teflon, which thermally isolated the reservoir from the chamber.

5.3.3 The alkali metal source

The alkali metal source is a variant of the metal vaporization source used by many groups [24]. The sample holder is a 3/4″ diameter cylindrical Al rod, with a counter hole (~0.5″ diameter, ~1/4″ deep) in the center. The sample holder is mounted onto a DC motor via a set screw at its bottom. Chunks of alkali metal (in this case, Na and K) are pressed into the counter hole. By adjusting the voltages on the DC motor, constant rotation speeds can be obtained for the sample holder.

The ablation laser is a *ns* Q-switched Nd:YAG laser (Continuum YG 681) that

provides approximately 100-500 mJ 1064 nm pulses at 30 Hz. The vaporization laser beam is directed into the chamber and focused by a f=150 mm convex lens some 150 mm above the sample holder surface. For both Na and K, a soft focus the ablation laser beam was found to be the optimum focusing condition to generate the maximum amount of clusters over a relatively long period ($\sim$ 30 minutes). Tightly focused laser beams quickly generated a plasma of alkali metal, and is believed to deplete the neutral clusters; since as the laser beam was tighly focussed, a colorful plume of plasma was observed along with an increase in the background ion noise, and a decrease of the neutral cluster photoioinization TOFMS signal. The vaporization pulse energy must be chosen with great care so as to maximize the TOFMS signal of the clusters, while at the same time keeping the signal stablized for as long as possible. The best ablation conditions are those for which the TOFMS signal is strong, but no colorful plasma is observed.

The advantages of using such a laser ablation alkali metal source instead of the heated oven nozzle developed previously by the group [1] are

- The heated oven nozzle usually requires the temperature to be as high as 360° C. At this high temperate the oven must operate continuously, which quickly depletes the sample inside, making the window for the experiment very short. The large amount of evaporated alkali metal also react with the diffusion pump oil, resulting in rapid degradation of the pump efficiency and frequent oil changes.

- The high temperature oven also radiates so much heat that the internal temperates of the clusters formed atop the oven cannot be effectively cooled.

- The setup time for the heat oven is also quite long. Typically it takes at least ten minutes to get the sample into the oven reservoir, seal the oven, install it into the chamber, and start the evacuation. During this time, some of the alkali metal, *e.g.*, K, will be oxidized and become unavailable for later experiments. As a result, clusters involving K could not be generated by the previous heated oven set up.

- The vaporization source is applicable to refractory and "volatile" metals alike, and so a much wider range of interactions can be studied with this system than was possible with the heated oven pick up source.

The present design of the laser ablation source suffers from one major disadvantage, however — stability. The TOFMS signal of certain clusters could vary by as much as $\pm 50\%$ over a period of several minutes even under the most optimized conditions. This proved to be the major obstacle in preventing the collection of high resolution REMPI electronic spectra of such clusters.

Other conditions were therefore tested in order to improve the stability. For example, instead of rotating the sample holder, the K sample was heated to 80° C to keep it in a molten state, in order to refresh the surface. Even this small amount of heating drove rapid evaporation, however. Thus, the sample lasted only a short time, and the stability of the cluster signal was not improved. Further work continues toward generating a more stable cluster source, but in the end it will likely be necessary to incorporate multi-beam ionization schemes that can be used to normalize the ion yield on a shot-to-shot basis. Such set ups are not applicable to single photon experiments, but should be of great utility in REMPI or multi-photon ZEKE-PFI studies [27].

5.3.4 The ZEKE-PFI apparatus

The heart of the ZEKE-PFI apparatus, a drawing of which is shown in Figure 5.2, consisted of extraction grids, a μ-metal flight tube, and an MCP detector. The extraction grids were the same as those used in the TOFMS, but the electrons were extracted in the direction opposite to the TOFMS. A third grid was placed 3 mm outside the extraction region to provide additional acceleration for the electrons. A μ-metal flight tube was attached to the ion source to provide shielding against magnetic fields. Finally, the MCP detector was placed on a flange attached to the probe chamber, directly opposite the TOFMS.

Grid B was held at ground, while grid A was connected to the voltage pulse circuit.

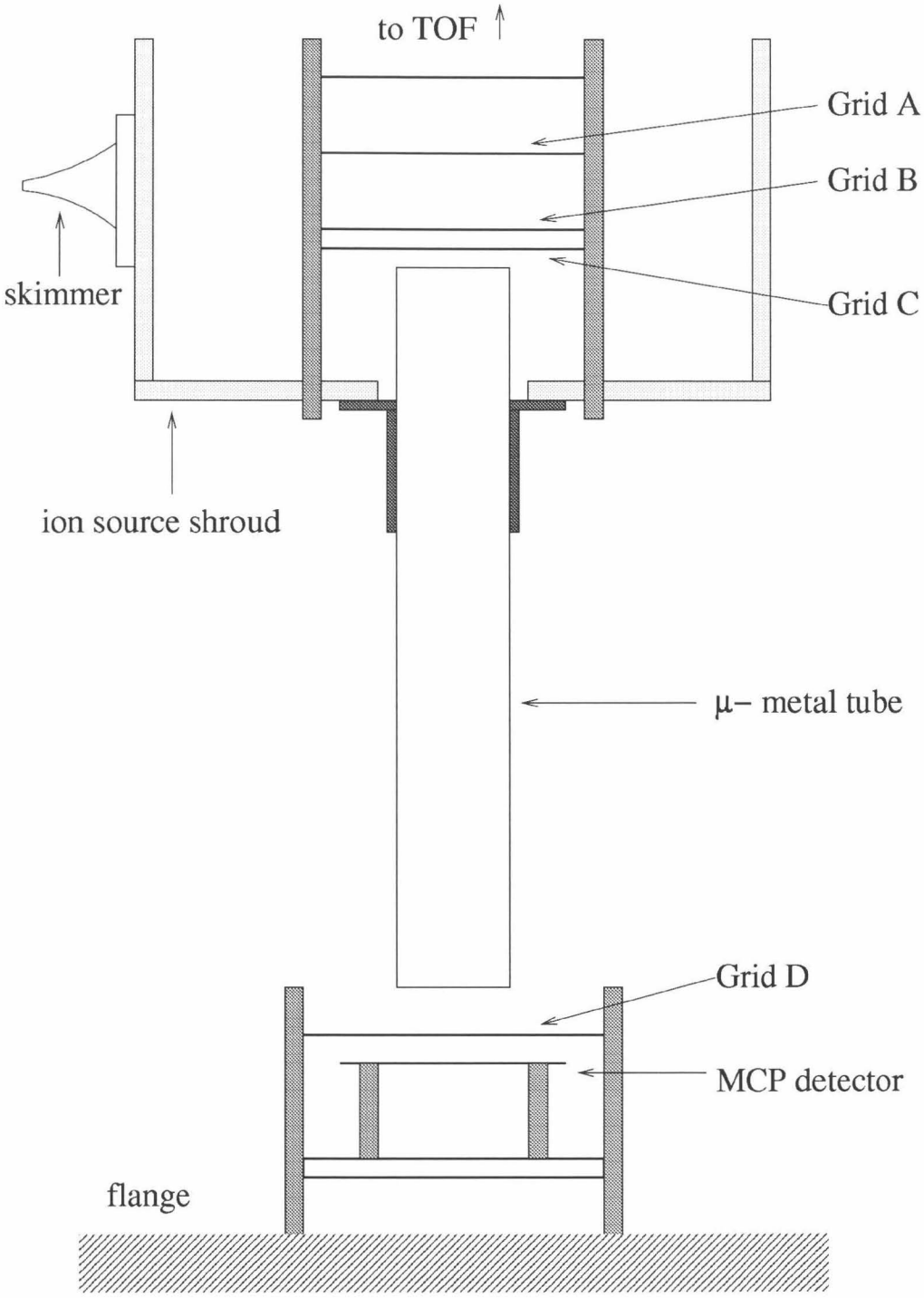

Figure 5.2: ZEKE-PFI apparatus.

Figure 5.3: Energy levels involved in the generation of ZEKE-PFI signal. The top of each shaded area represents an ionization limit of the molecule when no electric field is applied, while the bottom of each shaded area represents the lowered ionization limit in the pulsed electric field. With no field applied, laser radiation populates the ZEKE states within the shaded areas. After a delay of 1-3 μs, the electric field is pulsed on, ionizing the molecules and generating ZEKE-PFI electrons, which are detected by a MCP .

The pulse circuit, a schematic of which is in Reference [1], was an inverting amplifier containing a CLC 400 op amp. Typically, a -4 V output pulse 10 μs long and having a risetime of $\sim$80 ns was used in the experiments, but by selecting different resistors for the circuit, smaller pulses were generated.

The offset null of the op amp was used to keep the grid as close to ground as possible when no pulse was applied. Grid C, 3 mm from grid B, was held at a potential of 9 V (provided by batteries) to give the electrons additional acceleration. The μ-metal flight tube was held at this same potential. Grid D, just in front of the detector, was floated because this increased the signal by a factor of $\sim$2. Initially, a set of deflector plates was attached where grid C is, to ensure that the electrons hit the detector. This was later found to be unnecessary. While reasonble S/N ratios could be achieved with the present arrangement, they could be improved by using either deflector plates or voltage pulses on grid C to eliminate interference from kinetic electrons.

High voltage for the dual MCP detector was provided by a Stanford Research Systems PS 325 power supply. The output of the supply, typically 1800-2000 V, was connected to a voltage divider circuit so the appropriate potential difference would be placed across each MCP (details of the ZEKE-PFI circuits may be found in [1]). The maximum input voltage is 2400 V, at which the voltage across each MCP is 1000 V, the highest allowed value, and the current is 400 μA. The potential difference of 400 V between grid D and the first MCP gives the ZEKE-PFI electrons sufficient energy to generate secondary electrons when they strike the MCP. As it is important that the resistors in the circuit be rated for the voltages across them, high-voltage resistors from Caddock were used. Finally, the voltage should be applied to the MCPs slowly (100 V steps) so as not to damage them.

The anode was held at a potential 200-300 V higher than the last MCP to ensure that the secondary electrons would hit it. This was done by connecting the anode via a low-pass filter to the VR1 output of the Jordan Co. TOFMS power supply and applying the correct voltage. Since this voltage is too high to connect to the oscilloscope, a high-pass filter was employed so only the ac signal would reach the

processing electronics. Mica capacitors, rated for 3000 V, were used because they perform well at high frequency.

When the operating voltages are applied to the ZEKE-PFI apparatus, ZEKE-PFI electrons, or immediate electrons, for that matter, are not initially observable because of stray charge build-up on the apparatus, especially after operating the TOFMS. The procedure for removing the stray charge is given in Appendix B. After following this procedure, the signal, an oscilloscope trace of which is shown in Figure 5.4, is stable, but the S/N ratio sometimes improves after a few hours of use.

Figure 5.5 shows the ZEKE spectra of K atom, which has a resolution of about 7 cm^{-1}, along with the threshold photoionization efficiency spectrum of K taken with the TOFMS. The large redshift of the latter spectrum is caused by the several hundred V/cm electric field of the positive ion extraction optics.

5.3.5 Lasers and optics

In the ZEKE-PFI experiments presented in Chapter 6, the third harmonic of a Nd:YAG laser (Infinity 40-100 from Coherent) pumped one tunable parametric source at a time, being either the type II BBO OPO described in Chapter 3 or the OPG/OPA described in Chapter 4. The type II BBO OPO was used most of the time. In the experiments where a second higher energy photon was required to ionize the cluster, a 355 nm high reflector dichroic mirror was used to combine a 355 nm photon with the tunable output of the OPO or OPG/OPA. The 355 nm beam was provided by the residual 355 nm pump radiation leaking out of the OPO/OPG, which is about 1-2 mJ/pulse. To generate tunable UV photons in the 280 nm to 420 nm region for single color photoionization experiments, the BBO doubling system described in Chapter 3 was used. The ionizing laser beam entered through a fused silica window at the top of the chamber, and its beam waist was located at the ionization region of the TOFMS system. The wavelengths of the OPO and OPG/OPA lasers were calibrated with a commercial wavemeter (Burleigh WA-4500A) and corrected to their vacuum values. Peak heights were not corrected for the variations of OPO power

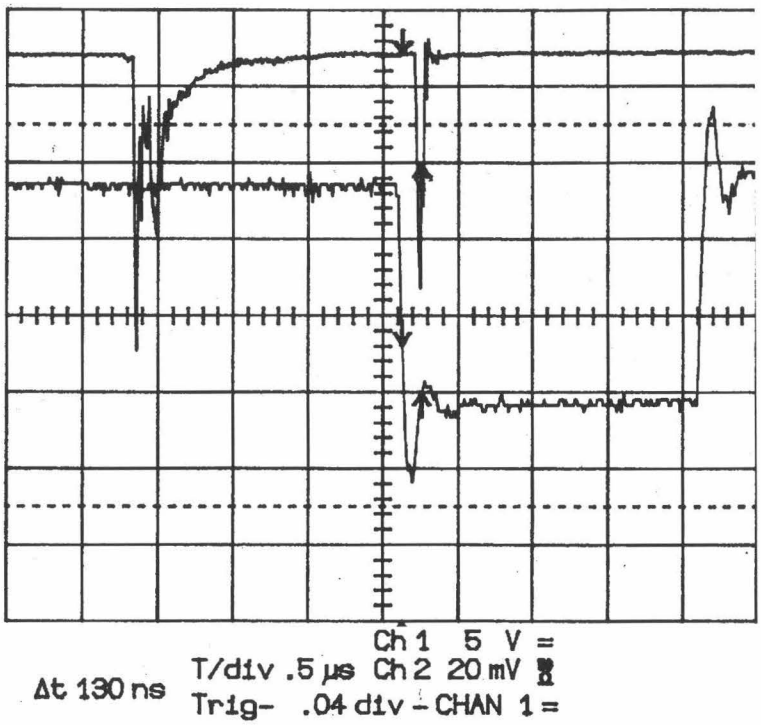

Figure 5.4: DSO traces of (upper trace) the ZEKE-PFI signal from K atoms and (lower trace) the leading edge of the voltage pulse used to extract the high-n Rydberg electrons.

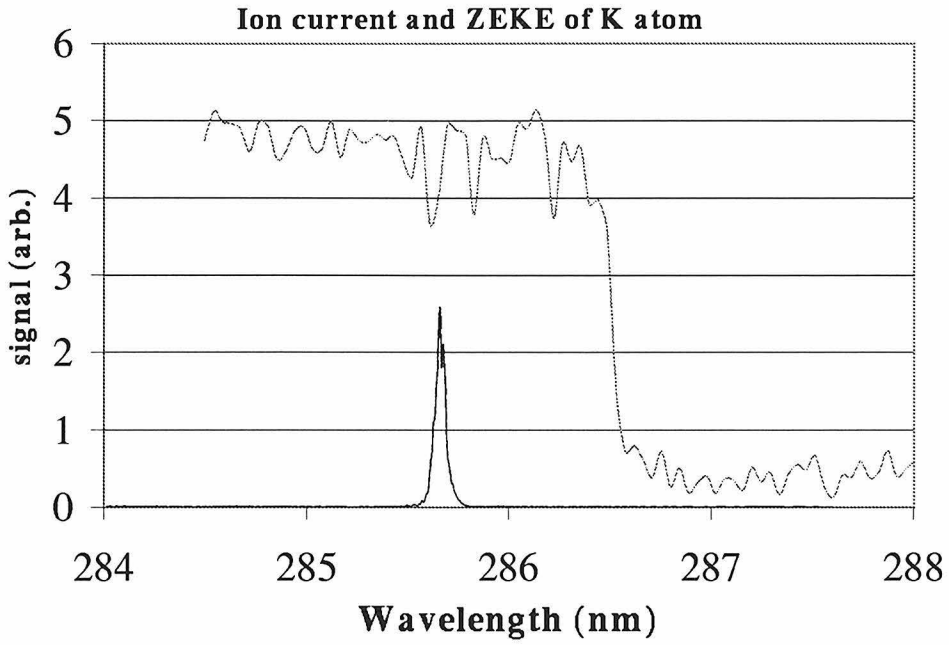

Figure 5.5: The ion yield and ZEKE-PFI spectra of K atoms. The ZEKE-PFI spectra gives a resolution of about 7 cm^{-1}under a PFI voltage of 5 volts

with wavelength, which were sometimes large. A schematic of the entire ZEKE-PFI experimental apparatus is shown in Figure 5.6

5.4 Data acquisition and laser scanning

The data collection procedure involved stepping the tunable OPO's frequency, averaging the ion or electron signal from a few hundred laser shots with the DSO, and transferring the data to a personal computer for further processing. The OPO scanning and oscilloscope were controlled by the PC, with communication between PC and DSO conducted over a GPIB bus (National Instruments). The data collection software is contained in Appendix B. The method by which the laser frequency, doubling crystal position, and Pellin-Broca prisms were scanned under computer control is described in Chapters 3 and 4.

The amplified signal was connected to the oscilloscope with a 50 Ω termination and digitized at 10 ns intervals. The oscilloscope was triggered by the signal from a photodiode in mass spectrometry experiments, and by the ionization voltage pulse in ZEKE-PFI experiments. The signal was averaged in function E or F on the oscilloscope. Data processing on the PC involved adding the points in the signal peak and subtracting the background. In mass spectrometry experiments, the program located and processed the peaks for any desired number of masses, while in ZEKE-PFI experiments or REMPI studies in which only one time (mass) was of interest, this single peak alone was processed. The processed data were stored in a file on the PC's hard drive.

A digital delay generator (SRS DG-535) served to synchronize the ablation laser pulse, the ionization laser pulses, and the molecular beam pulses. This was straightforward in the ion yield measurement experiments, since the DG-535 has five independent channels. The four channels are used the following sequence: channel T_0 charges the ablation laser; channel A switches 27 ms after T_0 and fires the ablation laser (for which the internal Q-switch fires about 0.5 μs after the DG-535 pulse); channel B opens the pulsed valve, which could either lead or lag behind the ablation laser

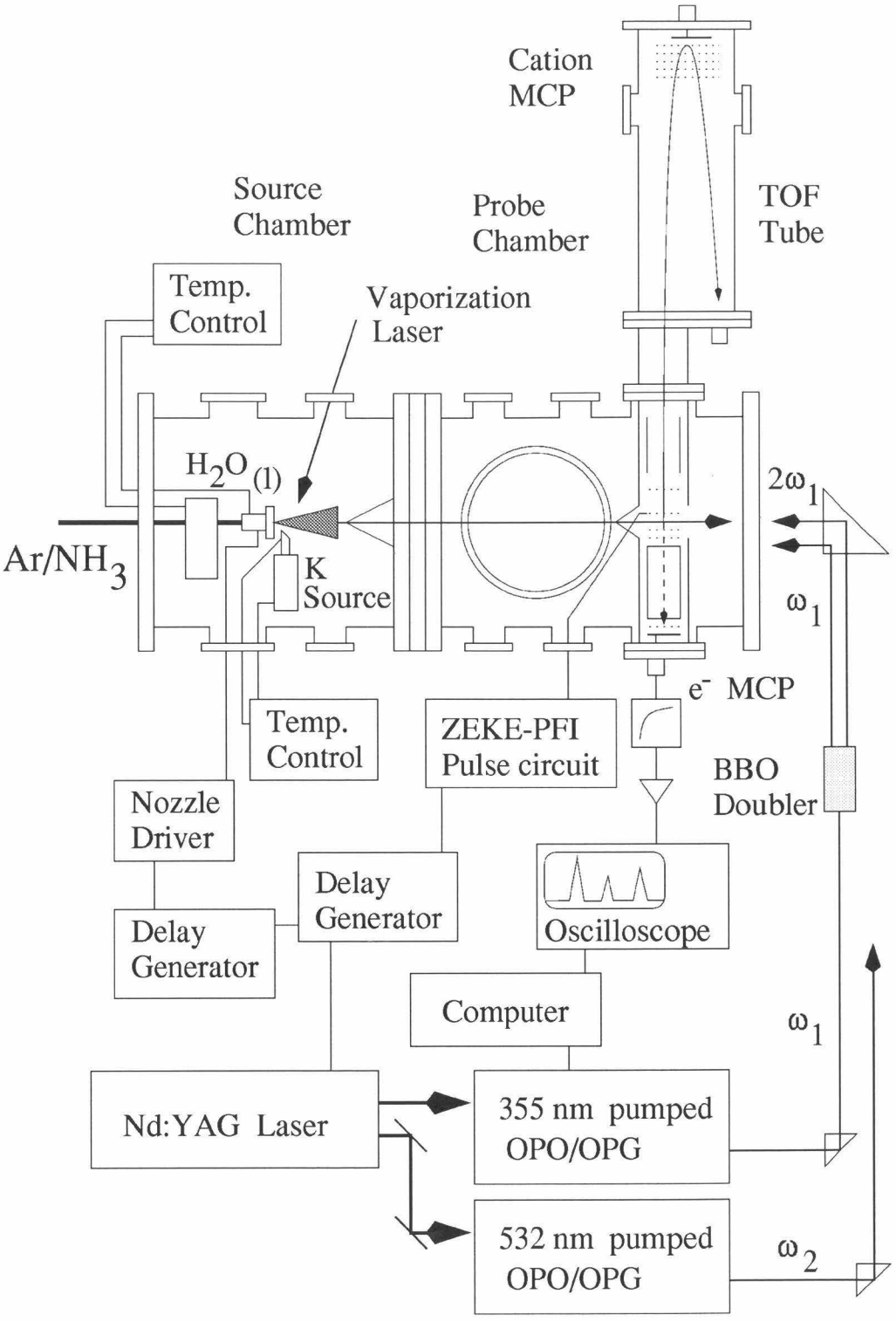

Figure 5.6: Schematic of the complete experimental apparatus used in ZEKE-PFI experiments on alkali metal - small molecule clusters.

pulse from channel A; channel C triggers the Infinity Nd:YAG pump laser (the actual laser pulse occurs about 0.5 μs later). Temporal synchronization of the ZEKE-PFI experiments was more involved and required two DG-535 delay generators. The first DG-535 is triggered as bfore, while the second DG-535 is triggered *by* the Infinity Nd:YAG laser and itself triggers the ZEKE-PFI pulse circuit along with the digital oscilloscope.

Bibliography

[1] D.A. Rodham, *Ph.D. Thesis*, Caltech:159, 1997.

[2] R.E. Smalley, L. Wharton, and D.H. Levy, *Acc. Chem. Res.*, 10:139, 1977.

[3] R.E. Smalley, D.H. Levy, and L. Wharton, *J. Chem. Phys.*, 64:3266, 1976.

[4] V.I. Karataev, B.A. Mamyrin, and D.V. Shmikk, *Sov. Phys.-Tech. Phys.*, 16:1177, 1972.

[5] B.A. Mamyrin, V.I. Karataev, D.V. Shmikk, and V.A. Zagulin, *Sov. Phys.-JETP*, 37:45, 1973.

[6] W.C. Wiley and I.H. McLaren, *Rev. Sci. Instrum.*, 26:1150, 1955.

[7] J.H. Callomon, T.M. Dunn, and I.M. Mills, *Phil. Trans. R. Soc. Lond.*, 259:499, 1966.

[8] E. Riedle, Th. Knittel, Th. Weber, and H.J. Neusser, *J. Chem. Phys.*, 91:4555, 1989.

[9] L.A. Chewter, M. Sander, K. Müller-Dethlefs, and E.W. Schlag, *J. Chem. Phys.*, 86:4737, 1987.

[10] K.G. Spears and S.A. Rice, *J. Chem. Phys.*, 55:5561, 1971.

[11] D. Proch and T. Trikl, *Rev. Sci. Instrum.*, 60:713, 1989.

[12] Matthew S. Johnson, *Spectroscopy of Reactive Molecules and Clusters*, Ph.D. thesis, California Institute of Technology, 1996.

[13] R.E. Bumgarner and G.A. Blake, *Chem. Phys. Letters*, 161:308, 1989.

[14] R.D. Suenram F.J. Lovas, G.T. Fraser, J.Z. Gillies, C.W. Gillies, and M. Onda, *J. Molec. Spectrosc.*, 137:127, 1989.

[15] W. Kong, D. Rodgers and J.W. Hepburn, *Chem. Phys. Lett.*, 203 (1993), 497-502.

[16] K. Müller-Dethlefs, M. Sander, and E.W. Schlag, *Z. Naturforsch.*, A39:1089, 1984.

[17] G. Reiser, W. Habenicht, K. Müller-Dethlefs, and E.W. Schlag, *Chem. Phys. Letters*, 152:119, 1988.

[18] K. Müller-Dethlefs and E.W. Schlag, *Ann. Rev. Phys. Chem.*, 42:109, 1991.

[19] R. Lindner, H.J. Dietrich and K. Müller-Dethlefs, *Chem. Phys. Letters*, 228:417, 1994.

[20] W.A. Chupka, *J. Chem. Phys.*, 99 (1993), 5800-5806.

[21] W.A. Chupka, *J. Chem. Phys.*, 98 (1993), 4520-4530.

[22] A. Held; U. Aigner; L.Ya. Baranov; H.L. Selzle and E.W.Schlag, *Chem. Phys. Lett.*, 299 (1992), 110-114.

[23] E. Rabani, L.Ya. Baranov, R.D. Levine and U. Even, *Chem. Phys. Lett.*, 221 (1994), 473-481.

[24] M.A. Duncan, *Ann. Rev. Phys. Chem.*, 48 (1997) 69-93.

[25] C.P. Schulz, R. Haugstätter, H.U. Tittes and I.V. Hertel, *Phys. Rev. Letters*, 57:1703, 1986.

[26] C. Nitsch, C.P. Schulz, A. Gerber, W. Zimmermann-Edling and I.V. Hertel, *Z. Physik D*, 22:651, 1992.

[27] J.R. Carney, F.C. Hagemeister and T.S. Zwier, *J. Chem. Phys.*, 108:3379, 1998.

Chapter 6 Ionization spectroscopy of the alkali metal - small molecules clusters

6.1 Introduction

As described in Chapter 1, alkali metal ions solvated by water and other small molecules have received considerable attention [1, 2, 4, 5, 6] due to their importance in many chemical, biological and geological systems, the central nervous system being a prime biochemical example. An accurate description of the manner in which the alkali ion-solvent and solvent-solvent interactions change within the solvation shells surrounding different cations is required to explain phenomena such as ion selectivity in membrane channels [7], but adequately detailed information is difficult to obtain from condensed phase measurements. Consequently, many researchers have studied gas phase clusters comprised of a metal ion attached to a few solvent molecules, since they form more accessible models of solution behavior [8].

Most of the experimental thermodynamic information available on the clusters of interest (*e.g.*, $A(H_2O)_n$, $A(NH_3)_n$ and $A(C_6H_6)_n$, for which A = Na, Na^+, K, K^+ ...) has been obtained via high pressure mass spectrometry. Specifically, by measuring the equilibrium constants for the reactions $A^+(M)_n \leftrightarrow A^+(M)_{n-1} + M$, where M = water, ammonia, benzene, etc, the Kebarle and Castleman groups have determined the binding energies of various molecules to the clusters as a function of n [9, 10]. As expected, the intermolecular potential wells are deeper than those of the neutral hydrogen-bonded clusters due to the ion-dipole character of the forces involved. The experimental binding energies also agree well with the results of numerous theoretical studies [11, 12, 13] for the range of n for which theoretical work has been done, namely $n \leq 6$. However, in the case of $Na^+(NH_3)_n$ clusters there is some disagreement on the number of solvent molecules required to fill the first solvation shell. The equilibrium

constant data indicate that five molecules fill the shell [10], but the theoretical work of Hashimoto and Morokuma suggests that only four molecules occupy the shell [13].

Further complicating the picture are mass spectrometric experiments recently performed by the Lisy group which suggest that six NH_3 molecules actually fill the first solvation shell in gas phase sodium-ammonia clusters [14]. In these experiments, infrared photons from a CO_2 laser are used to pump the ammonia "umbrella" vibrational mode in the clusters, with mass spectrometry serving to detect any predissociation products. Only clusters with more than six ammonia molecules fragmented, suggesting that the first six ammonia molecules are more strongly bound and form the first solvation shell. More recently, the same group compared the IR dissociation processes of $A^+(C_6H_6)_n(H_2O)_m$ (A= Na or K) hybrid clusters. For hybrid clusters with K cation, the benzene molecules tend to form the inner core with K^+, while for Na cation, four H_2O molecules form the first hydration cell and cannot be displaced by benzene. In short, benzene is capable of dehydrating K^+, while Na^+ is resistant to any disruption of its first hydration sphere by benzene. Although this method is somewhat indirect, no other spectroscopic information on the structures of these clusters has yet been obtained.

Indeed, while quantitative intermolecular potential energy surfaces (IPESs) can be obtained from high resolution spectra of the cluster intermolecular vibrational modes, as has been demonstrated in the case of hydrogen-bonded dimers [17], the absence of such data has thus far prevented the determination of the IPESs of alkali metal - solvent clusters. The elegant single- or multi-photon IR dissociation experiments outlined above are only able to access the high frequency, *intramolecular* modes of the clusters. For the softest modes supported only by the ion-solvent interactions themselves, there are only incomplete spectra available at present. In previous experiments done in the Blake group [15, 16] on $Na(H_2O)$ and $Na(NH_3)$, for example, their structures and binding energies were examined by measuring the intermolecular vibrational frequencies of the sodium cation-molecules' bending and stretching modes. Due to the limitations imposed by the setup time of the alkali metal evaporation source, only clusters of Na were investigated by these authors.

Neutral clusters composed of an alkali metal atom and solvent molecules are also of interest in their own right because of their utility in the study of electron solvation [23, 24, 25, 26, 27]. In this context, it is interesting to note that the ionization energies (IP) of clusters with n≤20 determined from PIE spectra reveal that while the $Na(NH_3)_n$ or $Cs(NH_3)_n$ IPs decreased monotonically with n, those for $Na(H_2O)_n$ or $Cs(H_2O)_n$ decreased until n = 4, whereupon they reached the bulk value and remained essentially constant [28, 30]. Interestingly, similar research has not been performed with K atoms, and this forms the major motivation for the work presented here.

Theoretical studies have offered two possible explanations for the different IP behavior of sodium-water and sodium-ammonia clusters. Using local spin density functional theory, Barnett and Landman [31] found that the Na atoms in $Na(H_2O)_n$ clusters with $n \geq 4$ are surrounded by H_2O molecules and that the Na 3s electron is partially removed from the atom and delocalized in a "surface Rydberg-like state." Delocalization is not found to occur to the same extent in $Na(NH_3)_n$ clusters with $n \leq 30$, and that the cluster IPs change until this size is reached. In an *ab initio* MO study, Hashimoto and Morokuma [12, 13] found that the Na atom is surrounded by NH_3 molecules and that the 3s electron is partially delocalized in large clusters, much as for the large $Na(H_2O)_n$ clusters. The MO calculations, however, predict the Na atom is attached to the surface of a water cluster with the 3s electron located outside the water cluster such that the IP is largely unaffected by the addition of water molecules. Similar calculations are not yet available for larger clusters involving heavier alkali metals such as K or Cs. Furthermore, no direct structural evidence for either the neutral or ionized clusters has been obtained, and much more vibration-rotation data is needed to characterize their IPESs.

As a step toward a more complete description of alkali metal-solvent interactions, this study of gas phase clusters of K with water, ammonia or benzene has been conducted using one color photoionization spectroscopy and ZEKE-PFI photoelectron spectroscopy. It is well documented that the IPs of neutral clusters and the rovibrational energy levels of the ionized clusters can be measured more accurately with ZEKE-PFI spectroscopy than with energy resolved photoelectron or PIE spec-

troscopies [32, 33, 34, 35], but that PIE spectra are easier to access and form an excellent starting point for more complex investigations.

6.2 Photo-Ionization Efficiency (PIE) spectra of alkali metal - small molecule clusters

While photoionization spectra of clusters formed by K and small molecules have not been investigated before, the rough location of these features can be estimated from similar studies of Na - containing clusters and the ionization potentials of the bare alkali atoms (Figure 6.1). Photoionization mass spectra showing that $K(NH_3)_n$, $K(H_2O)_n$, and $K(C_6H_6)_n$ clusters are indeed formed in the pick-up source and reach the ionization region of the TOFMS/ZEKE-PFI apparatus are presented in Figures 6.2,6.4,6.5. Laser radiation between 300 - 355 nm was used to ionize the netural K in the clusters. The peak at 8.81 μs is due to bare K^+.

In Figure 6.2, the clusters were ionized by photons at ~300 nm, and all cluster sizes with $n \geq 1$ were observed. A more detailed view of the TOFMS spectrum is presented in Figure 6.3, and shows that the features of each cluster with size $n > 1$ are split into multiplets with a mass separation of unity. These multiplets indicate that some dissociation of the clusters occurs upon ionization.

In Figure 6.4, the $K(H_2O)_n$ clusters were ionized by a 355 nm photon, whose energy is below the IP of the $K(H_2O)$ cluster. Therefore, only clusters with $n > 1$ are observed. We also attempted to collect the TOFMS spectra of potassium-water clusters with photon of wavelength 400 nm. No cluster features were observed, indicating that all have IPs with λ <400 nm. This observance is in agreement with the known IP values of Na-$(H_2O)_n$ and Cs-$(H_2O)_n$ clusters

In Figure 6.5, a series clusters of with $K_m(C_6H_6)_n$ up to $n = 5$, m=1 or possibly $n = 2$, m=2, are generated by single photon ionization. The correct combination of n or m is uncertain at present due to the mass degeneracy between C_6H_6 (mass=78) and two K atoms (also mass=78), but can be resolved in the future by a comparison

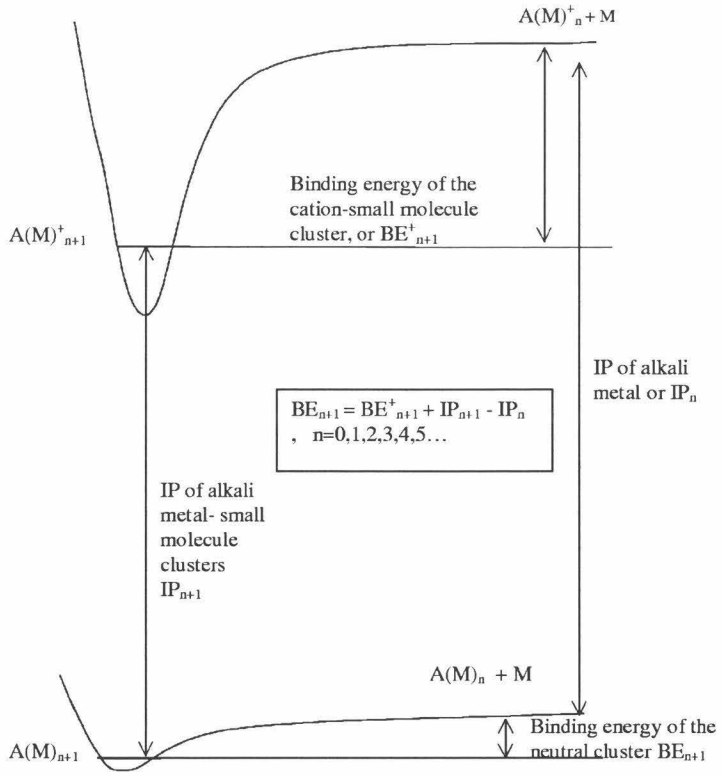

Figure 6.1: A schematic diagram of the potential energy surfaces of neutral and cationic of alkali metal - small molecules clusters. The binding energy of the neutral cluster is weak compared to that of the charge-(induced) dipole bound cation.

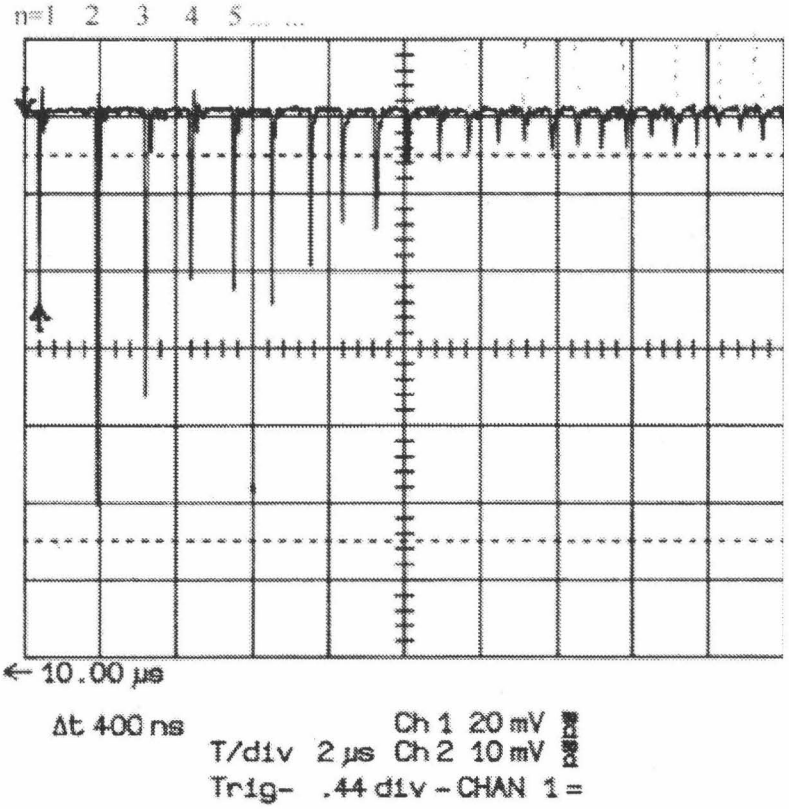

Figure 6.2: TOF-MS spectra of $K(NH_3)_n$, n=1,2,3...

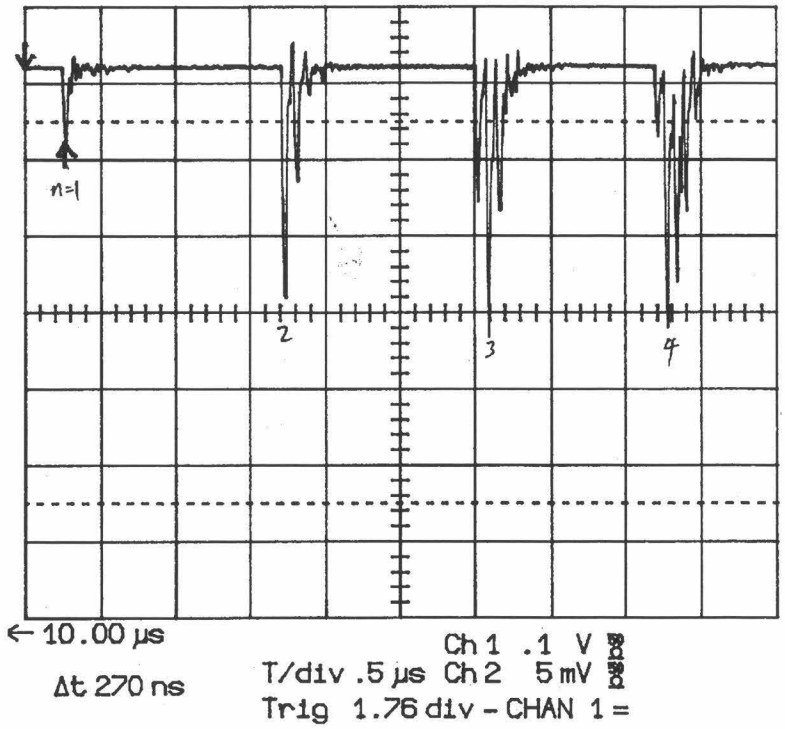

Figure 6.3: Expanded view of the TOFMS spectrum of $K(NH_3)_n, n = 1, 2, 3...$, which reveals dissociation within the clusters upon ionization.

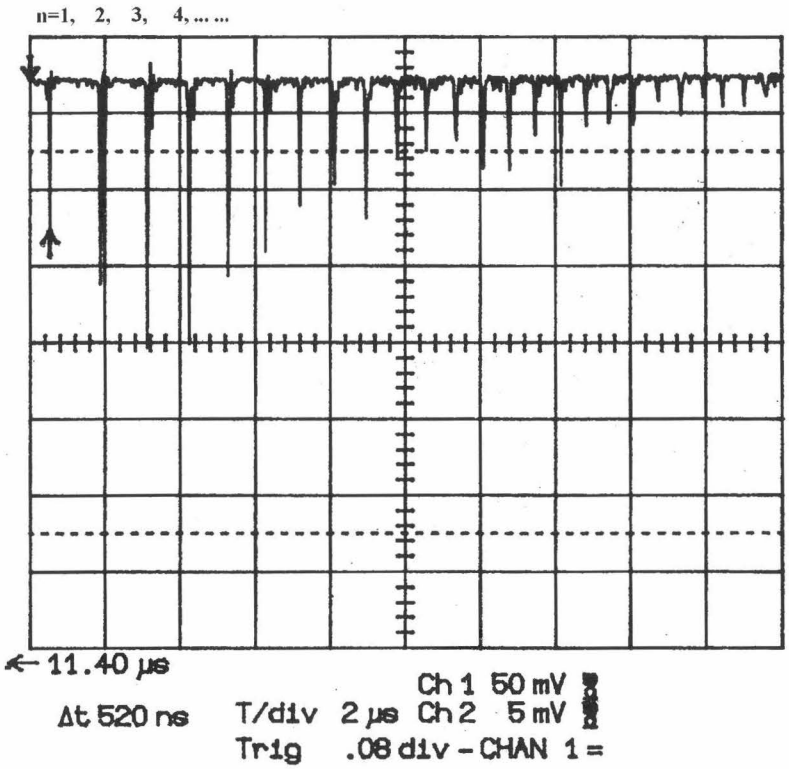

Figure 6.4: TOF-MS spectra of $K(H_2O)_n$, n=1,2,3...

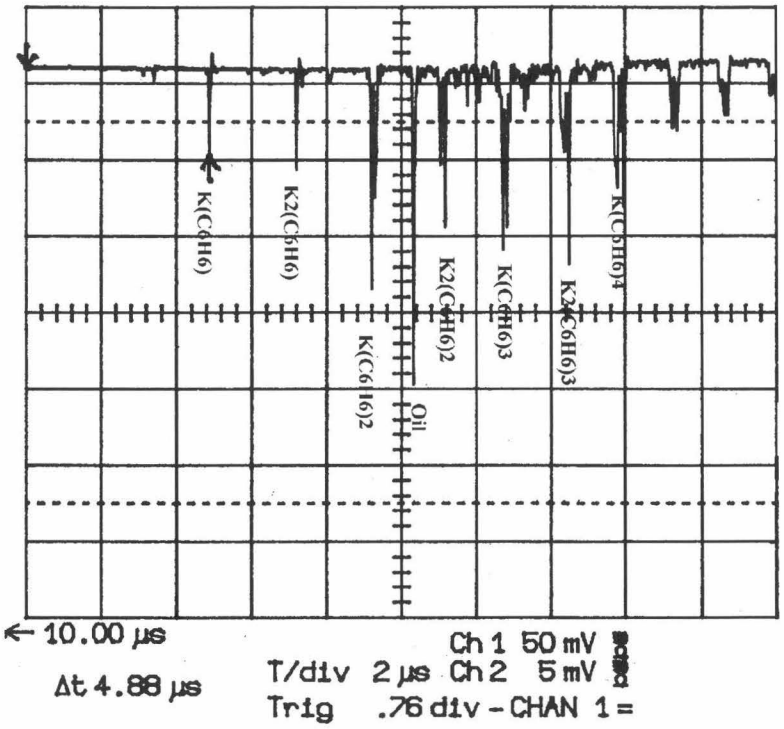

Figure 6.5: TOF-MS spectra of $K(C_6H_6)_n$, n=1,2,3...

of the experimental isotopic patterns versus those expected from different numbers of K and/or benzene in the cluster. The assignment in Figure 6.5 hinges on the first two mass peaks. For single photon ionization at 355 nm, the clusters must contain at least one potassium atom, and the only plausible assignments of these peaks are $K(C_6H_6)$ and $K_2(C_6H_6)$. Given their nearly equal intensities, the suggested peak assignments follow directly. Very recently, results have appeared which shows that benzene molecules can form a sandwich structure with transition metal cations [3], and so there is great interest in identifying the exact structures of the clusters shown in Figure 6.5. The threshold PIE spectra of isolated potassium atoms versus potassium dimers should be rather distinct, and could be used to infer generalities of the bonding patterns once they are available. Interestingly, the $K_m(C_6H_6)_n$ TOFMS spectrum is quite different from that of $Na_m(C_6H_6)_n$ where only clusters with m=1 are observed.

After the IPs of the various clusters were bracketed, their photo-ionization efficiency (PIE) spectra were then measured. The PIE spectrum of $K(NH_3)$ and $K(ND_3)$ are shown in Figure 6.6, for which the upper traces depict the PIE spectra while the lower traces present the ZEKE-PFI spectra to be discussed in the next section. Sharp steps in the ion yield are seen at the ionization potential of $K(NH_3)$, and also at the frequency of the pseudo-diatomic K-(NH_3) intermolecular stretching vibration some 187 cm^{-1} to the blue of the IP.

The PIE spectrum of $K(H_2O)$ is shown in Figure 6.8. Here, the sharp steps present in the $K(NH_3)$ PIE spectrum are not observed. This washing out of the structure in the PIE curve mostly likely results from a larger geometry change from the neutral to ionic forms of the cluster such that longer progressions in the intermolecular vibrations result, with correspondingly reduced relative Frank-Condon factors for adiabatic ionization. The PIE spectrum of $K(H_2O)$ is also different from the PIE spectrum of $Na(H_2O)$, which does possess a relatively sharp step at the IP and another rise at the Na-(H_2O) streching frequency [20]. Due to these factors the ZEKE-PFI spectrum of $K(H_2O)$ has not yet been recorded despite considerable searching.

Shown in Figure 6.7 are the PIE spectrum of the $K(NH_3)_n$ clusters values of n

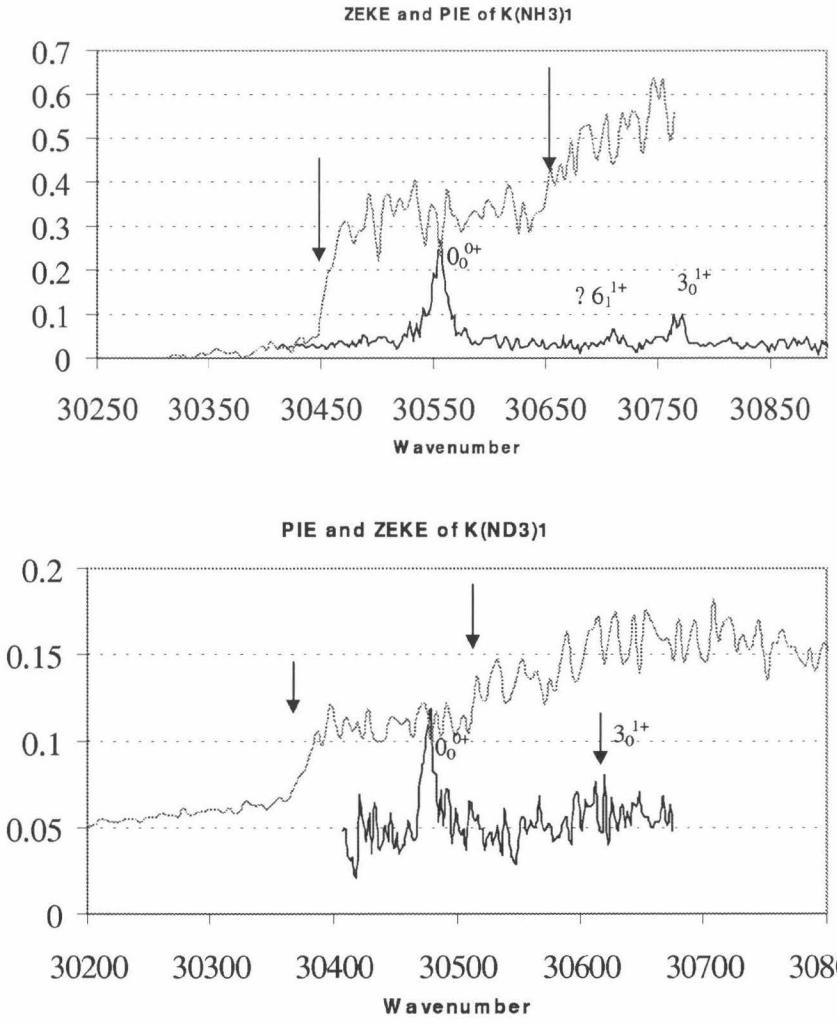

Figure 6.6: ZEKE and PIE spectra of $K(NH_3)$ and $K(ND_3)$.

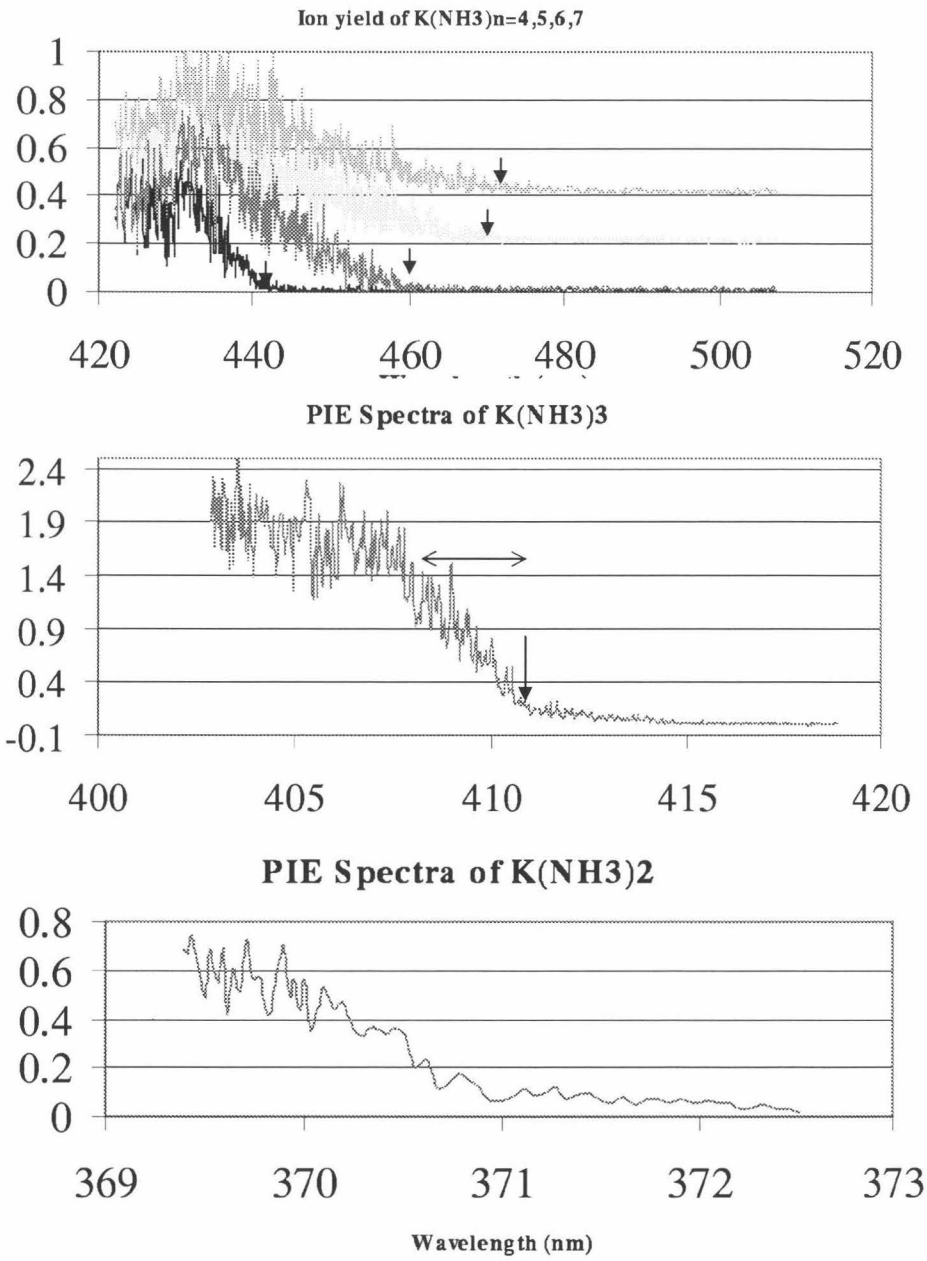

Figure 6.7: PIE spectra of $K(NH_3)_n, n = 2, 3, 4, 5, 6, 7$.

from n=2 $\rightarrow$ 7. The IP for each cluster is assigned to the onset of the PIE curve, which clearly is a subjective measure. A typical example of the uncertainties inherent in this approach is given in the Figure by the arrow, with the error being proportional to the slope of the PIE curve.

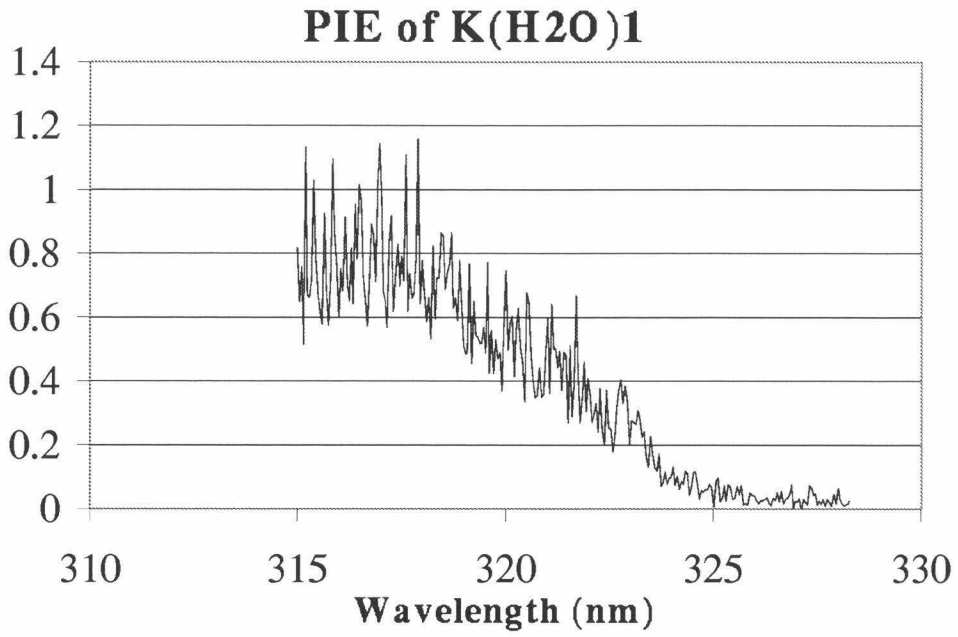

Figure 6.8: PIE spectra of $K(H_2O)$, where, unlike the case for $K(NH_3)$, no sharp step at the IP is seen.

Similarly, Figure 6.8 shows the PIE spectrum of $K(H_2O)$, which indicates that the IP of $K(H_2O)$ is about 3.823eV. The ion source setup was unstable during these measurement, and so insufficient signal-to-noise was available for studies of the $K(H_2O)_n, n > 1$ PIE curves. As noted above, coarse scans have shown that all larger clusters have IPs of less than 3.49 ev (or a photon energy of 355 nm), but larger

than 3.20 ev (or a photon energy of 390 nm).

Finaly, the PIE spectrum of the $K(C_6H_6)_n$ (n=1,2) clusters have also been obtained. They are shown along with the PIE spectrum of $Na(C_6H_6)_n$, $n = 1, 2$ in Figure 6.9. For completeness, the IPs of $Na(C_6H_6)$ and $Na(C_6H_6)_2$ were also measured via their PIE spectra (which are are presented in Figure 6.9) to be 4.32 eV and 4.17 eV, respectively. The IPs for all of the clusters studied with the PIE technique are listed Table 6.1. Clearly, the range of values is considerable, and the wide tunability and simplicity of the type II BBO OPO greatly simplified these studies compared to the great many dye changes that would be required with traditional laser sources.

The trends in the IP data for K-small molecule clusters are similar to those observed for lithium-, sodium- and cesium-containing systems. For example, Figure 6.10 plots the IPs of $K(NH_3)_n$ vs. $n^{1/3}$. From this figure it is clear that for $K(NH_3)_n$ clusters, the IPs show a decreasing tendency with increasing cluster size and can be extrapolated to a bulk value of about 1.5 eV. This value is in good agreement with the bulk value of the electron affinity of $(NH_3)_n^-$, which is approximately 1.48 eV [29]. Although the values are not as accurate for $K(H_2O)_n$, the IPs also seem to approach the bulk value of 3.2 eV for the electron affinity of water, as is seen in clusters containing Li, Na, or Cs atoms [56, 57, 58]. For the ammonia clusters, the $n^{1/3}$ dependence can be equated to a dependence on the radius of the cluster, as would be expected for a screening model in which the alkali$^+$ core is screened by the dielectric environment provided by the various solvation shells of the NH_3 molecules.

From the measured IP values, the differences in the binding energies between the alkali metal atom or the cation and the small molecules are determined directly (figure 6.1). These values are given in Tables 6.2,6.3,6.4,6.5,6.6,6.7 as the IP shifts (in kcal/mole). From the measured IP shifts and the binding energies of the cations determined from high pressure mass spectrometry thermochemistry experiments, it is possible to estimate independently the binding energies of the neutral and cationic clusters for the alkali metals Na and K. The errors on the individual binding energies are dominated by uncertainties in the thermochemistry determinations, and are sufficiently large at present that it is not yet possible to use them to examine effects

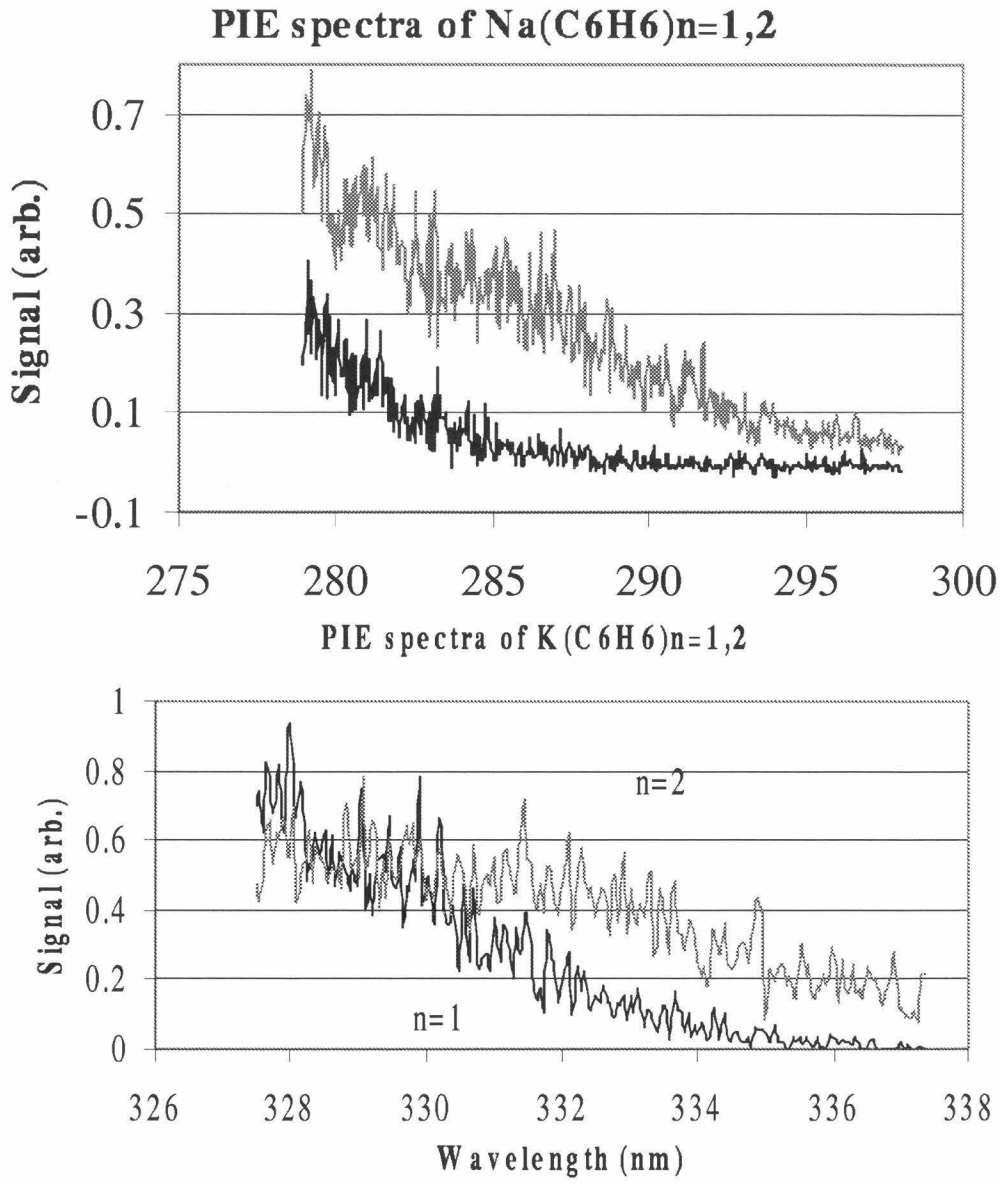

Figure 6.9: The PIE spectra of $K(C_6H_6)_n, n = 1, 2$ and $Na(C_6H_6)_n, n = 1, 2$.

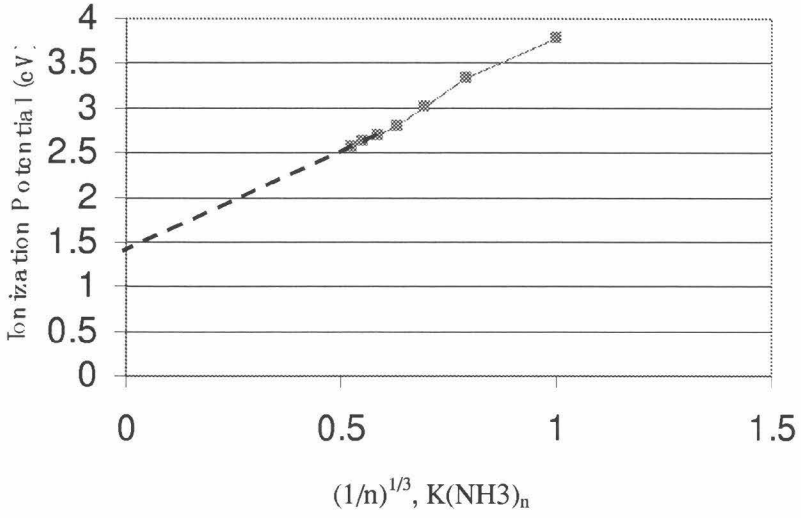

Figure 6.10: The IPs of $K(NH_3)_n, n = 1, 2, 3, 4, 5, 6, 7$ are plotted against $n^{1/3}$ which shows a bulk limit value of 1.48 eV.

Table 6.1: Ionization potentials of $K(H_2O)_n$ and $K(NH_3)_n$

Cluster size n	$K(H_2O)_n$	$K(NH_3)_n$	$K(C_6H_6)_n$
K only	4.34066±0.000001 eV	4.34066 ±0.000001 eV	4.34066 ±0.000001 eV
n=1	3.823 eV	3.7886 ±0.002eV*	3.70±0.1 eV
n=2	>3.20 eV <3.49 eV	3.343 ±0.02 eV	3.59 eV ±0.2 eV
n=3	>3.20 eV <3.49 eV	3.018 ±0.02 eV	-
n=4	>3.20 eV <3.49 eV	2.806 ±0.04 eV	-
n=5	>3.20 eV <3.49 eV	2.696 ±0.05 eV	-
n=6	>3.20 eV <3.49 ev	2.627 ±0.1 eV	-
n=7	>3.20 eV <3.49 eV	2.594 ±0.1 eV	-

Note: Error reflects the slope of the PIE spectrum.

Table 6.2: Binding energies of $K(NH_3)_n$, kcal/mole

	IP shift	Cation Binding Energy[a]	Neutral Binding Energy
1	12.72	20.1	7.4
2	22.99	16.2	5.9
3	30.48	13.6	6.1
4	35.36	11.5	6.6
5	37.90	10.2	7.7
6	39.49	9.2	7.6
7	40.50	-	-

[a] Reference [50]

such as solvent shell closings, but a number of interesting features do emerge.

For example, it appears that the binding energy of $K^+(C_6H_6)$ is very close to that of $K^+(H_2O)$ — the difference is only 0.4 kcal/mole. In contrast, the binding energy of $Na^+(C_6H_6)$ is nearly 4.0 kcal/mole higher than $Na^+(H_2O)$. Furthermore, the relative binding energy differences of the neutrals versus cations are most extreme for the benzene-containing clusters, illustrating the important role of charge in the cation-π interaction. Interestingly, the dimer binding energy differences do not support the theory proposed by Lisy group [8] that K^+ is more likely to bind to an aromatic complex, while Na^+ tends to remain hydrated in aqueous solution. This illustrates that many body effects are likely to be extremely important in determining the outcome of the closely balanced forces operating in selective nature of ion transport proteins, as has been concluded from theoretical analyses by the Dougherty group, and reinforces

Table 6.3: Binding energies of $K(H_2O)_n$, kcal/mole

	IP shift	Cation Binding Energy[b]	Neutral Binding Energy
1	11.91	17.9	5.99
2	$\leq$20.84	16.0	$\geq$7.1
3	$\leq$20.84	12.9	$\geq$12.8
4	$\leq$20.84	11.1	$\geq$11.1
5	$\leq$20.84	9.6	$\geq$9.6
6	$\leq$20.84	8.4	$\geq$8.4

[b] Reference [53]

Table 6.4: Binding energies of $K(C_6H_6)_n$, kcal/mole

	IP shift	Cation Binding Energy[c]	Neutral Binding Energy
1	14.75	18.3	3.55
2	17.29	17.0	14.5

[c] Reference [54]

Table 6.5: Binding energies of $Na(NH_3)_n$, kcal/mole

	IP shift [e,f]	Cation Binding Energy [g]	Neutral Binding Energy
1	20.02	29.1	9.1
2	35.92	22.9	7.0
3	45.96	17.1	7.1
4	50.94	14.7	9.7
5	53.41	10.7	8.2
6	55.04	9.7	8.1
7	58.27	-	-

[e] Reference [21, 15], [g] Reference [51]

Table 6.6: Binding energies of $Na(H_2O)_n$, kcal/mole

	IP shift[h]	Cation Binding Energy[b]	Neutral Binding Energy
1	17.51	24.0	6.5
2	30.85	19.8	6.5
3	38.22	15.8	8.4
4	44.67	13.8	7.3
5	44.67	12.3	12.3
6	44.67	10.7	10.7
7	44.67	-	-

[h] Reference [19, 15],[b] Reference [53]

Table 6.7: Binding energies of $Na(C_6H_6)_n$, kcal/mole

	IP shift	Cation Binding Energy[i]	Neutral Binding Energy
1	18.87	28.0	9.1
2	22.33	-	-

[i] Reference [52]

the need to acquire accurate data on larger clusters.

6.3 ZEKE-PFI spectra of alkali metal - small molecule clusters

Given the coarseness of the PIE ion yield curves, a higher resolution spectroscopic approach is necessary to characterize the structures, binding energies, and intermolecular vibrational modes of the clusters formed by the alkali metal - small molecule pick up source. The best such technique currently available is that of ZEKE-PFI spectroscopy, which can provide very precise measurement of IPs and vibrational spectra of the cation clusters as long as the Frank-Condon overlap is sufficiently good between the neutral and the cation near the ionization threshold.

Due to the sharp structure in their PIE surve, the initial single photon ZEKE-PFI experiments have been carried out on the $K(NH_3)$ and $K(ND_3)$ clusters, and the results are shown in Figure 6.6. Here, the first – and most intense – peak in each spectrum is assigned to the Δv=0 transition from the neutral cluster's vibronic ground state to the vibronic ground state of the cation. This transition is denoted with the notation 0_0^{0+}, $\nu_{v''}^{v'}$ is such that the leading number refers to the intermolecular vibrational mode involved in the transition, with the subscript and superscript denoting the vibrational quantum number in the lower and upper state, respectively. Quantum numbers of cationic states are followed by a plus symbol. The vibronic ground state wavefunctions of the neutral and ionized clusters are predicted to have A_1 symmetry in the C_{3v} point group [36].

Adiabatic ionization energies of 30451$\pm$ 15cm^{-1}for $K(NH_3)$ and and 30554$\pm$ 15cm^{-1}for $K(ND_3)$ are derived from the spectra. While ZEKE-PFI spectroscopy can give more

accurate IPs, the uncertainties of these values are large because of as yet unresolved rotational structure in the peaks and because no correction has been made for the lowering of the IP by the existing stray field. The stray field-induced shift of the IP is dennoted by ΔE and is given in $cm^{-1}$by $\Delta E = aF^{1/2}$ where F is the stray electric field (or field before the PFI pulse) in V/cm and a is a constant that generally falls between 2 and 6 [35]. a can be determined by careful control of the stray external field while measuring the IP shifts, and from the plot of the IP shift vs. external stray field the value of a can be fit. This has not yet proved feasible in these studies due to equipment limitations. Nevertheless, the adiabatic IPs for $K(NH_3)$ and $K(ND_3)$ are in excellent agreement with the values obtained from the PIE spectra, with all the major ZEKE-PFI features being shifted by about 120 $cm^{-1}$from the sharp steps of the PIE spectra due to the strong electric field present in the ion source when positive ions are extracted into the TOFMS. The adiabatic IPs of the deuterated clusters are shifted $\sim$70 cm^{-1} to lower frequency because of the changes in their zero point vibrational energies.

The $K(NH_3)$ and $K(ND_3)$ clusters each have three vibrational modes of a_1 symmetry and three vibrational modes of e symmetry [37]. The K-NH_3stretching mode is the lowest frequency mode of a_1 symmetry and is denoted by ν_3, while the doubly degenerate bending mode is the lowest frequency mode of e symmetry and is denoted by ν_6. Following the 0_0^{0+} peak, each spectrum shows a short progression in ν_3. The frequencies of ν_3 are found to be 205 $cm^{-1}$for $K^+(NH_3)$ and 188 $cm^{-1}$for $K^+(ND_3)$. The $K^+(NH_3)$ stretching feature has good a signal-to-noise ratio, and the assignment is coincident with the second sharp step in the PIE spectra of $K^+(NH_3)$. The $K^+(ND_3)$ stretching feature has poorer a signal-to-noise ratio, but, similar to $K^+(NH_3)$, a coincidence is observed between a sharp step in its PIE spectra and the admittedly weak ZEKE-PFI signature.

The assignment of the second largest peak to the intermolecular stretch is based both on the isotopic shift upon deuteration and the similarity of the observed spectrum to the well characterized ZEKE-PFI states of $Na^+(NH_3)$ [15]. According to [38], the frequency shift of $K(NH_3)$ to $K(ND_3)$ in the pseudo-diatomic limit should

be given by

$$F(a_1) = \frac{\nu_1\nu_2\nu_3}{\nu_1'\nu_2'\nu_3'} = \frac{m_D}{m_H}\sqrt{\frac{M}{M'}} = 1.948, \tag{6.1}$$

$$F(e) = \frac{\nu_4\nu_5\nu_6}{\nu_4'\nu_5'\nu_6'} = \sqrt{(\frac{m_D}{m_H})^3\frac{M}{M'}\frac{I}{I'}} \simeq 2.7 \tag{6.2}$$

where the prime quantities stand the values associated with the deuterated species. Clearly, the stretching mode of a_1 symmetry has a much smaller predicted shift than that of the bending mode of e symmetry because the stretching mode reduced mass change is rather small while the bending moment of inertia is essentially that of ammonia in the cluster, and so is greatly affected by the $NH_3 \rightarrow ND_3$ substitution. Longer progressions of the cationic stretch in the ZEKE-PFI spectra [but seen in $Na(NH_3)$] were not measurable due to the poor signal-to-noise ratio.

While the strongest peaks in the spectra are most likely produced by the ionization of neutral clusters in their vibronic ground states, this is another, weaker, peak that may plausibly be attributed to the ionization of vibrationally excited neutral clusters (the vibrational temperature is estimated to be ~100 K). This peak, located on the lower frequency side of the ν_3 feature, is tentatively assigned to be the hot band of the intermolecular ν_6 bending mode. Without additional data on various isotopomeric species, a definite spectroscopic assignment is not yet possible. It should be noted, however, that it is unlikely the weak feature arises from the hot band of the stretching ν_3 mode for the following reason. Regardless of its assignment, the relative frequency of the weak peak to the IP is the energy difference of the ν_3 or ν_6 mode in the neutral and in the cation, and is about 160 cm^{-1}. Based on this shift, the possibility of this peak being the hot band of ν_3 is low, since the required frequency of the stretching mode in the neutral would be only 45 cm^{-1}, which is below that predicted by nearly a factor of five. Large differences in the bending frequency are predicted theoretically [55], and the observed change in the neutral/cation bending frequency for the more strongly bound sodium-ammonia cluster is somewhat larger, as expected, at 190 cm^{-1}. The possible energy levels involved are outlined in Figure 6.11.

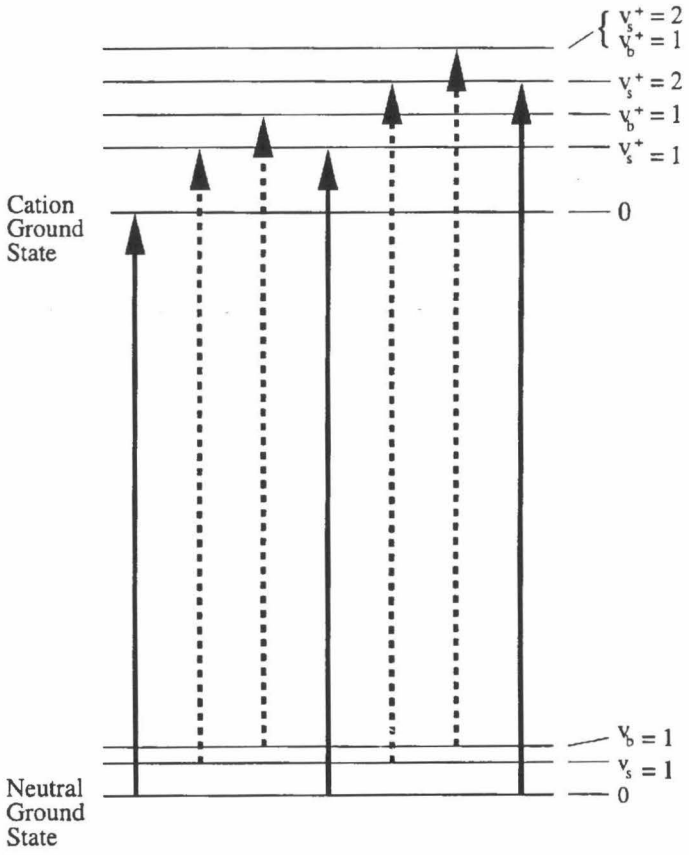

Figure 6.11: An illustration of the possible transitions in the ZEKE-PFI experiments on the $K(NH_3)$ dimer.

From single photon experiments such as these, it is not possible to isolate the frequency of the bending mode ν_6 because the bending and the stretching mode have different symmetries. Therefore, it is not possible to directly access the 6^{1+} state through the ground vibronic state of the neutral. In order to more completely determine the intermolecular vibrational frequencies, and thereby the intermolecular force field, it is necessary to access the bending modes through an intermediate state, such as has been performed for the $Na(NH_3)$ cluster. Resonance Enhanced Multi-Photon Ionization (REMPI) experiments were therefore carried out on $K(NH_3)$, and the spectrum obtained is given in Figure 6.12.

At present, no assignment has yet been made for this very congested spectrum. The reason for this complexity is not yet clear. The denser nature of the potassium electronic state manifold may lead to greater state mixing and coupling, but increased potential for the reactivity of $K(NH_3)$ clusters upon excitation may also play a role. Some dissociation of the cluster ions is observed in the detailed TOFMS spectra of $K(NH_3)_n$ clusters, and excitation to the first excited A state does open up reactive channels that are not available to the ground state. Interestingly, even though reactions involving the $Na(NH_3)$ are energetically feasible, they are not observed. For example, a comparison of the REMPI spectra of $K(NH_3)$ with that of $Na(NH_3)$ is presented in Figure 6.13. It is obvious that even at the higher lying 3s - 4s electronic state, the $Na(NH_3)$ REMPI spectra are simple, even to the extent of yielding clearly discernable rotational structure. Extending these multi-photon studies to longer wavelengths involving the O–H and N–H stretches may alleviate this problem somewhat.

6.4 Conclusions

In this Chatper, the photoionization spectroscopy of the neutral and cationic states of alkali metal-small molecules clusters were examined with the widely tunable parametric lasers described in earlier Chapters. The IPs of the $K(H_2O)_n$, $K(NH_3)_n$, and $K(C_6H_6)_n$ cluster series have been acquired. These IP data are used to examine

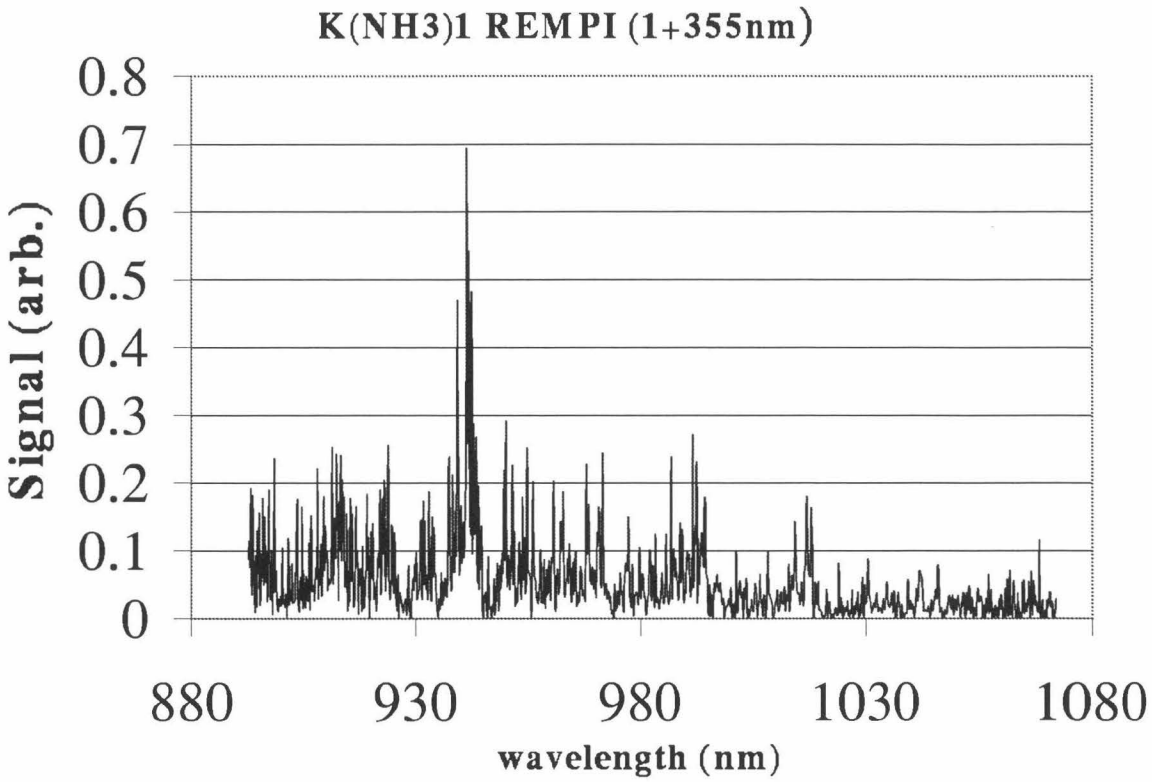

Figure 6.12: Resonance enhanced multi-photon ionization spectra of $K(NH_3)$ cluster. the second photon is a fixed photon at 355 nm.

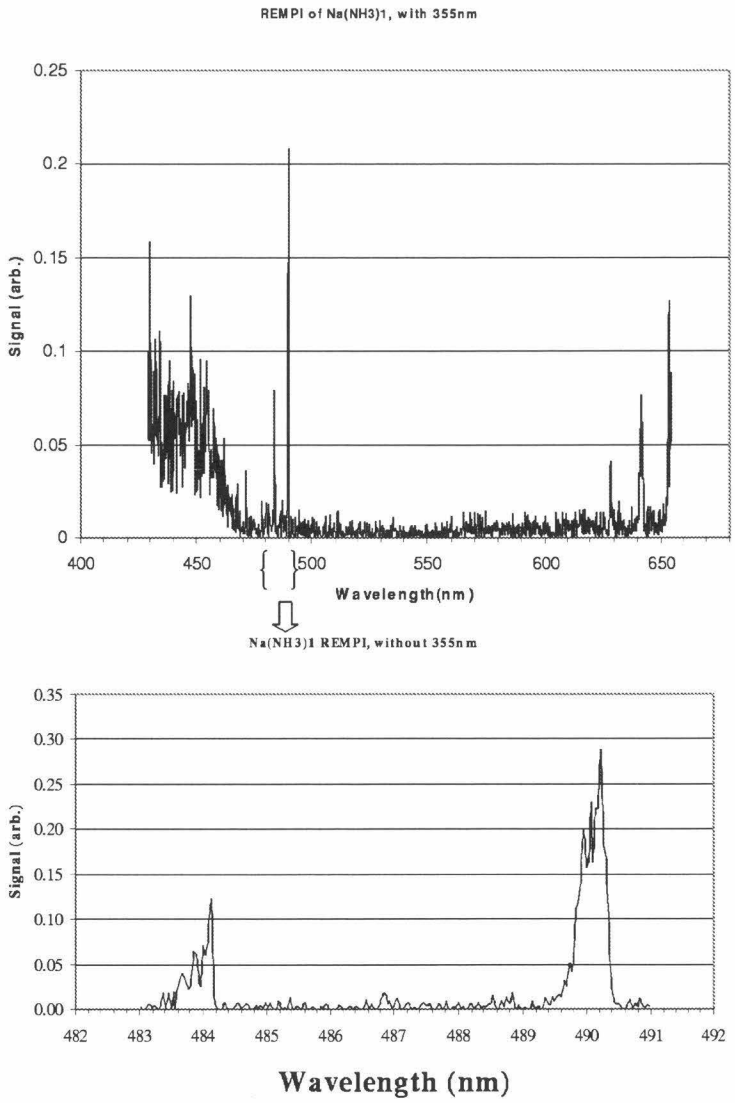

Figure 6.13: REMPI of $Na(NH_3)$ cluster, the lower part is a blow-up of the 3s-4s electronic transition.

the binding energies of the neutral and charged clusters, and the results reveal that studies of large and mixed clusters will be essential to model studies of important biological process such as selective ion recognition and transport. The ZEKE-PFI spectra of $K(NH_3)$ and $K(ND_3)$ have been collected, and give the frequency of the ν_3 intermolecular stretchomg mode of the cation, and reveal that the angular anisotropy in the intermolecular potential is greatly increased by the charge-dipole nature of the cation force field.

Bibliography

[1] W. Rudolph, M.H. Brooker, and C.C. Pye, *J. Phys. Chem.*, 99:3793, 1995.

[2] J.C. Polanyi, and J. Wang, *J. Phys. Chem.*, 99:13691, 1995.

[3] P. Weis, P.R. Kemper, and M.T. Bowers, *J.Phys. Chem. A*, 101 (1997), 8207-8213

[4] E.D. Glendening, *J. Am. Chem. Soc.*, 118:2473, 1996.

[5] J.E. Combariza and N.R. Kestner, *J. Phys. Chem.*, 99:2717, 1995.

[6] F.F. Abraham, M.R. Mruzik and G.M. Pound, *Faraday Discuss. Chem. Soc.*, 61:34, 1976.

[7] M.D. Toney, E. Hohenester, S.W. Cowan, and J.N. Jansonius, *Science*, 261:756, 1993.

[8] O.M. Cabarcos, C.J. Weinheimer, and J.M. Lisy, *J. Chem. Phys.* , 110 (1999), 8429-8435

[9] I. Džidić and P. Kebarle, *J. Phys. Chem.*, 74:1466, 1970.

[10] A.W. Castleman, Jr., P.M. Holland, D.M. Lindsay and K.I. Peterson, *J. Am. Chem. Soc.*, 100:6039, 1978.

[11] C.W. Bauschlicher, Jr., S.R. Langhoff, H. Partridge, J.E. Rice and A. Komornicki, *J. Chem. Phys.*, 95:5142, 1991.

[12] K. Hashimoto and K. Morokuma, *J. Am. Chem. Soc.*, 116:11436, 1994.

[13] K. Hashimoto and K. Morokuma, *J. Am. Chem. Soc.*, 117:4151, 1995.

[14] T.J. Selegue and J.M. Lisy, *J. Phys. Chem.*, 96:4143, 1992.

[15] D.A. Rodham, G.A. Blake, *Chem. Phys. Lett.*, 264 (1997), 522-530.

[16] K.H. Wang, D.A. Rodham, G.A. Blake and V Mckoy *J. Chem. Phys.*, 108 (1998), 4817-4827.

[17] R.J. Saykally and G.A. Blake, *Science*, 259:1570, 1993.

[18] C.P. Schulz, R. Haugstätter, H.U. Tittes and I.V. Hertel, *Phys. Rev. Letters*, 57:1703, 1986.

[19] C.P. Schulz, R. Haugstätter, H.U. Tittes and I.V. Hertel, *Z. Physik D*, 10:279, 1988.

[20] C.P. Schulz, A. Gerber, C. Nitsch and I.V. Hertel, *Z. Physik D*, 20:65, 1992.

[21] C. Nitsch, C.P. Schulz, A. Gerber, W. Zimmermann-Edling and I.V. Hertel, *Z. Physik D*, 22:651, 1992.

[22] C.P. Schulz, C. Nitsch, *J. Chem. Phys.*, 107:9794, 1997.

[23] L. Manceron, A. Loutellier and J.P Perchard, *Chem. Phys.*, 92:75, 1985.

[24] P.F. Meier, R.H. Hauge and J.L. Margrave, *J. Am. Chem. Soc.*, 100:2108, 1978.

[25] L.A. Curtiss and J.A. Pople, *J. Chem. Phys.*, 82:4230, 1985.

[26] J. Bentley and I. Carmichael, *J. Phys. Chem.*, 85:3821, 1981.

[27] M. Trenary, H.F. Schaefer III and P. Kollman, *J. Chem. Phys.*, 68:4047, 1978.

[28] I.V. Hertel, C. Hüglin, C. Nitsch and C.P. Schulz, *Phys. Rev. Letters*, 67:1767, 1991.

[29] G.H. Lee, S.T. Arbold, J.G. Eaton, H.W. Sarkas, K.H. Bowen, C. Ludewigt, H. Haberland, *Z. Phys. D*, 20(1991), 9-12.

[30] F. Misaizu, K. Tsukamoto, M. Sanekata and K. Fuke, *Chem. Phys. Letters*, 188:241, 1992.

[31] R. N. Barnett and U. Landman, *Phys. Rev. Letters*, 70:1775, 1993.

[32] K. Müller-Dethlefs, M. Sander, and E.W. Schlag, *Z. Naturforsch.*, A39:1089, 1984.

[33] G. Reiser, W. Habenicht, K. Müller-Dethlefs, and E.W. Schlag, *Chem. Phys. Letters*, 152:119, 1988.

[34] K. Müller-Dethlefs and E.W. Schlag, *Ann. Rev. Phys. Chem.*, 42:109, 1991.

[35] R. Lindner, H.J. Dietrich and K. Müller-Dethlefs, *Chem. Phys. Letters*, 228:417, 1994.

[36] J.C. Greer, C. Hüglin, I.V. Hertel and R. Ahlrichs, *Z. Physik D*, 30:69, 1994.

[37] C. Nitsch, C. Hüglin, I.V. Hertel and C.P. Schulz, *J. Chem. Phys.*, 101:6559, 1994.

[38] G. Herzberg, *Molecular Spectra and Molecular Structure*, Vol. 3 (Van Nostrand, Princeton, NJ, 1966).

[39] G. Herzberg and E. Teller, *Z. Phys. Chem.*, 21:410, 1933.

[40] R.S. Mulliken and E. Teller, *Phys. Rev.*, 61:283, 1942.

[41] X. Song, C.W. Wilkerson, J. Lucia, S. Pauls, and J.P. Reilly, *Chem. Phys. Letters*, 174:377, 1990.

[42] J. Flügge and P. Botschwina, in *Structures and Dynamics of Clusters*, Universal Academy Press, 1996.

[43] A. Loutellier, L. Manceron, and J.P. Perchard, *Chem. Phys.*, 146:179, 1990.

[44] G. Reiser, D. Rieger, T.G. Wright, K. Müller-Dethlefs, and E.W. Schlag, *J. Phys. Chem.*, 97:4335, 1993.

[45] M.C.R. Cockett, H. Ozeki, K. Okuyama, and K. Kimura, *J. Chem. Phys.*, 98:7763, 1993.

[46] C.T. Scurlock, S.H. Pullins, J.E. Reddic, and M.A. Duncan, *J. Chem. Phys.*, 104:4591, 1996.

[47] K. Müller-Dethlefs, *J. Chem. Phys.*, 95:4821, 1991.

[48] F. Merkt, H.H. Fielding, and T.P. Softly, *Chem. Phys. Letters*, 202:153, 1993.

[49] F. Merkt and T.P. Softly, *Phys. Rev. A*, 46:302, 1992.

[50] A.W. Castleman, jr, *Chem. Phys. Lett.*, 53:560, 1978

[51] A.W. Castleman, Jr., P.M. Holland, D.M. Lindsay and K.I. Peterson, *J. Am. Chem. Soc.*, 100:6039, 1978.

[52] B.C. Guo, J.W. Purnell, A.W. Castleman, jr, *Chem. Phys. Lett.*, 168:155, 1990

[53] I. Dzidic and P. Kebarle, *J. Phys. Chem.*, 74:1466, 1970

[54] J. Sunner, K. Nishizawa, and P. Kebarle, *J. Phys. Chem.*, 85:1815, 1981

[55] Y.-W. Hsiao, K.-M. Chang, and T.-M. Su, *Chem. Phys.*, 162(1992), 335-348.

[56] R. Takasu, F. Misaizu, K. Hashimoto, and K. Fuke, *J. Phys. Chem.*, 101 (1997), 3078.

[57] F. Misaizu, K. Tsukamoto, M. Sanekata, and K. Fuke, *Chem. Phys. Lett.*, 188 (1992), 241.

[58] I.V. Hertel, C. Hüglin, C. Nitsch, and C.P. Schultz, *Phys. Rev. Lett.*, 67 (1991), 1767.

Chapter 7 Unresolved questions and future directions

There is still much to be learned about the intermolecular interactions in alkali metal - small molecule clusters. Indeed, the research reported here is but the first step in a suite of increasingly complex and detailed investigations that will be needed to adequately characterize these model systems in terms of their relevance to biological and geological processes. Among the immediate steps that could be taken to improve the experimental sensitivity and capabilities, the most important would be to:

- Upgrade the ion source assembly. The ion source now is nearly a decade old, and is contaminated with a variety of materials. As a result, the TOFMS sensitivity is dramatically reduced from that under optimal conditions. In addition, the extraction and MCP detector voltages are somewhat low by present standards, resulting in lowered sensitivities for larger clusters that impact the MCPs with low velocities. Increasing the TOFMS voltages and improving the ion optics would make it possible to collect the PIE and/or REMPI spectra of $K(H_2O)_n, n > 1$ and $K(C_6H_6)_n$ clusters to much larger values of n than is presently possible. Such studies would provide a far more complete overview of the thermochemical data necessary to examine the solvation of alkali metal atoms at the molecular level.

- Improve the ZEKE-PFI collection efficiency. The current ZEKE-PFI photoelectron apparatus likely suffers from stray magnetic and electric fields, leading to significant instabilities in the signal levels. Improvements in the sensitivity of ZEKE-PFI spectrometer would enable the group to unambiguously assign the intermolecular vibrational frequencies of not only the cationic clusters, but those of the neutral as well. Such studies would require the collection and assignment

of both single- and multi-photon REMPI and ZEKE-PFI spectra, such as those that have been acquired for the $Na(NH_3)$ dimer, and would thus demand that a second tunable parametric laser be available.

- Improve the efficiency of the current OPOs. The output of the current Infinity-pumped type II BBO OPO is somewhat low for certain depletion-based ionization experiments that will be outlined below, particularly the 3^{rd} harmonic pumped cavity in the 630 nm to 820 nm region near degeneracy where the IPs of $K(H_2O)_n, n > 1$ clusters are located. The installation of two BBO crystals with new cut angles to provide both walk off compensation and the same sign of d_{eff} would be very helpful in this regard, and would improve the signal-to-noise ratios of both the TOFMS and ZEKE-PFI spectra. Alternatively, a KTA OPO cavity pumped by the Infinity 2^{nd} harmonic at 532 nm could be constructed. This cavity would provide tunability on the signal branch from 630 $\rightarrow$ 1064 nm with good efficiency and line widths similar to the type II BBO OPO. The idler branch would tune well beyond 4 μm, and thus the KTA OPO would be an important part of the group's effort to extend the coverage of parametric laser sources, as is described below.

In addition to the current techniques presently in use by the group to investigate the thermochemistry, structures, and intermolecular forces in alkali metal - small molecule clusters, there are a number of approaches developed by other groups that would provide new windows into the solvation processes in such clusters and their cations. The Hertel [1] group, for example, has investigated the multi-photon deletion spectroscopy of $Na(NH_3)_n$ neutral clusters. This approach enables very complex and short-lived intermediate states to be investigated even with nanosecond lasers, and has allowed them to map out both the ($3s$-$3p$) electronic levels and N–H stretching overtones, which appear to be strongly coupled to each other in the larger clusters. Similar experiments have been performed on mass selected cation clusters by the Lisy [2] group, who were able to assign the characteristic intramolecular vibrational frequencies of the cluster cations via near-IR multi-photon dissociation spectroscopy.

From this work, possible structures that are consistent with the vibrational spectra were deduced. Such studies are only possible in the near-IR where the photon energies are comparable to the binding energies. At longer wavelengths, additional features appear that provide considerable insight into the hydrogen bonding and other intermolecular properties of the alkali metal - small molecule clusters, but they are bound states and cannot be accessed by single color multi-photon dissociation studies. The structure in the PIE curves presented in Chapter 6 is sufficiently sharp, however, that it should be possible to collect two-color depletion spectra out to states with energies of only several hundred cm^{-1}. Spectroscopies of this type will require the development of tunable laser sources that can tune from 5000 cm^{-1} to 500 cm^{-1} without gaps. A possible multi-stage approach to such tunability is outlined next.

Scanning across the entire near- to mid-IR region with optical parametric devices has always been a difficult challenge because the optical damage threshold of the available crystals, such as $LiNbO_3$ or $ZnGeP_2$, is very low, and their regions of high transmission limited. Thanks to the development of periodically polled $LiNbO_3$ (PPLN), the oscillation threshold of parametric devices based on PPLN is nearly 100 times lower than that of bulk unpoled $LiNbO_3$. It is therefore quite straightforward to construct optical parametric devices based on PPLN materials, but only for small cross sectional area devices since the available PPLN wafers are very thin. The pulse energy is thus limited in PPLN devices. For this reason they are used primarily with high repetition rate pump lasers. The molecular beam source in the lab runs at < 100 Hz due to pumping speed restrictions, and with photoionization studies the necessary pulse energy is of order 1 mJ. Thus, PPLN-based OPOs and OPGs are not suitable for ionization-based spectroscopies, but should be of great utility in direct absorption measurements or cavity ring down spectroscopic probes of cluster vibrations. The recent availability of KTA in large, high quality crystals offers much better performance in the region of interest , as the transmission curves in Figure 7.1 attest.

Parametric devices based on KTA have recently provided exciting results, especially in terms of their high conversion efficiency and wide tunability [3]. For example, tests carried out by D. Richter at ITT with the type II cavity design presented in

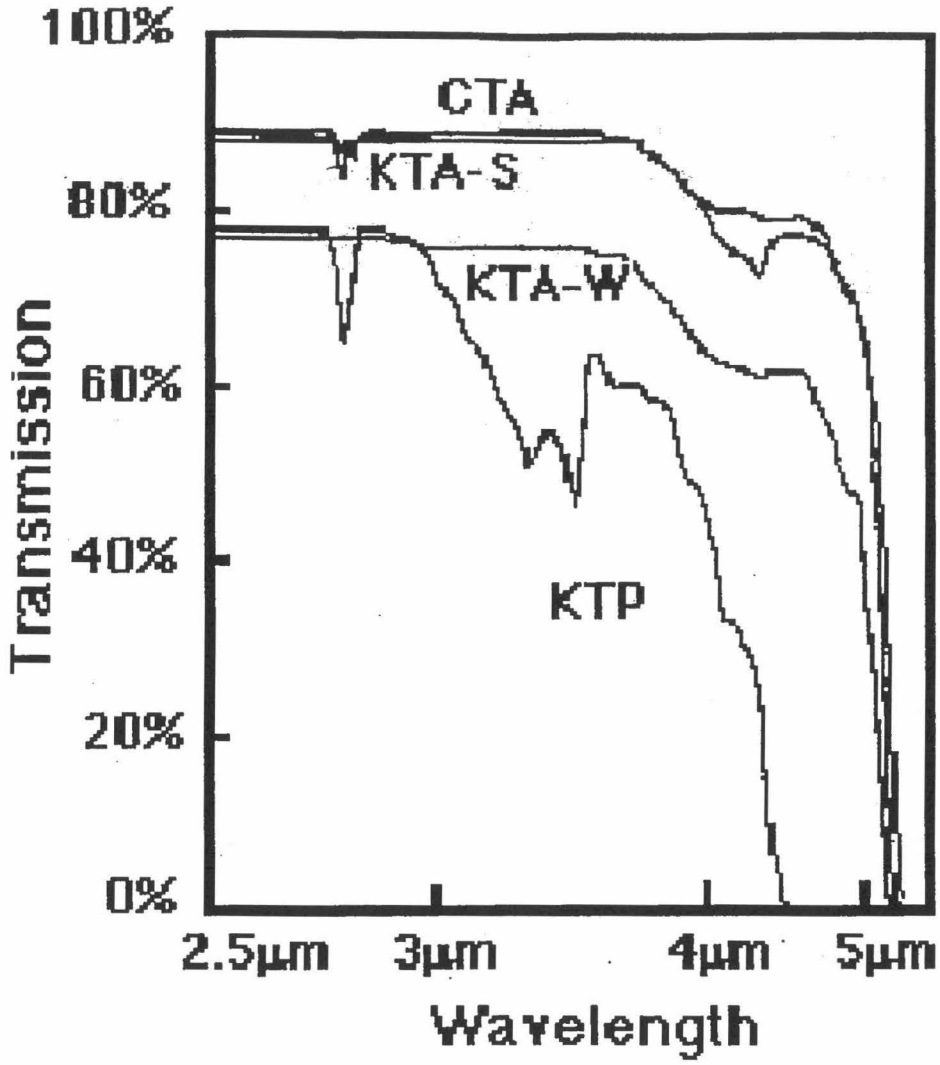

Figure 7.1: The transmission spectra of KTA and related materials in the 3.3 μm to 4 μm region.

Chapter 3, but pumped at 1064 or 532 nm and using KTA as the NLO material, have shown quite promising results by changing only the dichroic mirrors. Complete coverage of the transparency range of KTA is possible, with conversion efficiencies on the signal branch of up to 60-70% depending on the pump pulse energy and duration.

In addition, the recent improvement of crystal growth technologies for $ZnGeP_2$ (ZGP), $AgGaSe_2$ (AGS), and GaSe have fueled a resurgence of interest in OPO designs that operate well beyond 4 μm. Optical parametric devices using ZGP are usually pumped at 2.13 μm, which can be generated by a 1064 nm pumped KTA/KTP OPO operating at degeneracy [4]. The signal branch in such designs covers the 2.5 - 4.2 μm region; while the idler extends beyond 10 μm. AGS OPOs have most often been pumped by the 1.57 μm oputput from NCPM KTP 1064 nm-pumped OPOs, and can generate radiation in the $> 5\mu$m region as well, though not to wavelengths as long as can be obtained in ZGP [5]. Finally, difference frequency mixing of the KTA or KTP output near 2 μm in GaSe can be used to cover the 10 - 20 μm range. ZGP, AGS, and GaSe all have very large values of d_{eff}, and are therefore suitable for the single pass OPG/OPA design described in Chapter 4. In a cascaded design, where a 1064 nm-pumped KTA device pumps additional ZGP and GaSe stages, only one side of the degeneracy point must be seeded in the initial OPG/OPA. Thus, a single CW external cavity diode laser can provide up to 1000 cm^{-1} of coverage. With only two diodes, such a system would provide continuously tunable, ~transform-limited pulses from 2 - 20 μm.

Although these crystals are transparent in the IR region, they still have ~10%/cm absorption losses, and therefore thermally induced phase mismatch will again be a factor that limits the conversion efficiency at high pulse energies and high average powers. The computer simulation programs that have been developed to model the thermal effects in high power 266 nm UV generation will again be important in understanding and optimize the crystal lengths and cuts to be used in the near- and mid-IR. Once completed, however, the *ns* solid state sources in the laboratory will tune over the 200 nm $\rightarrow$ 20 μm range without gaps, and with line widths that range from 1-2 cm^{-1} down to the transform limit. Rotationally resolved spectra will

then be obtainable for a wide variety of clusters, and the new light sources should therefore lead to a tremendous improvement in our microscopic understanding of the processes associated with ion recognition and selectivity, and in the wide variety of other applications to which they no doubt will be put to use.

Bibliography

[1] P. Brockhaus, I.V. Hertel, and C.P. Schulz, *J. Chem. Phys.*, 110:393, 1999.

[2] O.M. Cabarcos, C.J. Weinheimer, and J.M. Lisy, *J. Chem. Phys.* , 110 (1999), 8429-8435

[3] Private communication with Dale Richter at ITT Industries.

[4] E. Cheung, S. Palese, H. Injeyan, C. Heofer, R. Hilyard, H. Komine, J. Berg and W. Bosenberg, *Adv. Sol. Sta. Lasers* 358, 1999

[5] T. Allik, J.L. Ahl, S. Chandra, J.A. Hutchinson, W.W. Hovis, J. Fox and L. Newman, *Adv. Sol. Sta. Lasers*,21, 1999

Appendix A Mathematical model for second order Nonlinear optical conversions

A.1 Calculation of the phase matching angle inside nonlinear optical crystals

Equations given in reference [3] could be used to calculate the phase matching angle inside nonlinear optical crystals. Although, the equations give one a straightforward solution, but sometimes there is no phase matching angle for a certain crystal and wavelength combination, then, these equations can not give meaningful value for the phase matching angle. Also, for so many different types of phase matching combinations, it is cumbersome to use so many formulas. I have found out that it is best to find the phase matching angle using *Lagrange* formula instead of using these analytical method.

A.2 Calculation of the angular, temperature, spectral acceptance bandwidth inside nonlinear optical crystals

Please see the tables below.

Table A.1: Equations for calculating the SHG internal angular bandwidth for the different of phase matching interactions.

Type interaction	Internal angular bandwidth for SHG ($\omega_1 + \omega_2 = \omega_3$)
I, ooe	$\Delta\theta = \frac{0.443\lambda_1[1+(n_{o2}/n_{e2})^2\tan^2\theta]}{L\tan\theta\lvert 1-(n_{o2}/n_{e2})^2\rvert n_2^e(\theta)}$
II, eoe & oee	$\Delta\theta = \frac{0.886}{L\tan\theta}\lvert\frac{n_1^e(\theta)[1-(n_{o1}/n_{e1})^2]}{\lambda_1[1+(n_{o1}/n_{e1})^2\tan^2\theta]} - \frac{n_2^e(\theta)[1-(n_{o2}/n_{e2})^2]}{\lambda_2[1+(n_{o2}/n_{e2})^2\tan^2\theta]}\rvert^{-1}$
I, eeo	$\Delta\theta = \frac{0.443\lambda_1[1+(n_{o1}/n_{e1})^2\tan^2\theta]}{L\tan\theta\lvert 1-(n_{o1}/n_{e1})^2\rvert n_1^e(\theta)}$
II, eoo & oeo	$\Delta\theta = \frac{0.443\lambda_1[1+(n_{o2}/n_{e2})^2\tan^2\theta]}{L\tan\theta\lvert 1-(n_{o2}/n_{e2})^2\rvert n_2^e(\theta)}$

Table A.2: Equations for calculating the SHG internal angular bandwidth for the different types of phase matching interactions.

Type of interaction	Internal angular bandwidth for SFG ($\omega_1 + \omega_2 = \omega_3$)
I, ooe	$\Delta\theta = \frac{0.443\lambda_3[1+(n_{o3}/n_{e3})^2\tan^2\theta]}{L\tan\theta\lvert 1-(n_{o3}/n_{e3})^2\rvert n_3^e(\theta)}$
II, eoe	$\Delta\theta = \frac{0.886}{L\tan\theta}\lvert\frac{n_1^e(\theta)[1-(n_{o1}/n_{e1})^2]}{\lambda_1[1+(n_{o1}/n_{e1})^2\tan^2\theta]} - \frac{n_3^e(\theta)[1-(n_{o3}/n_{e3})^2]}{\lambda_3[1+(n_{o3}/n_{e3})^2\tan^2\theta]}\rvert^{-1}$
III, oee	$\Delta\theta = \frac{0.886}{L\tan\theta}\lvert\frac{n_2^e(\theta)[1-(n_{o2}/n_{e2})^2]}{\lambda_2[1+(n_{o2}/n_{e2})^2\tan^2\theta]} - \frac{n_3^e(\theta)[1-(n_{o3}/n_{e3})^2]}{\lambda_3[1+(n_{o3}/n_{e3})^2\tan^2\theta]}\rvert^{-1}$
I, eeo	$\Delta\theta = \frac{0.886}{L\tan\theta}\{\frac{n_1^e(\theta)[1-(n_{o1}/n_{e1})^2]}{\lambda_1[1+(n_{o1}/n_{e1})^2\tan^2\theta]} + \frac{n_2^e(\theta)[1-(n_{o2}/n_{e2})^2]}{\lambda_2[1+(n_{o2}/n_{e2})^2\tan^2\theta]}\}^{-1}$
II, eoo	$\Delta\theta = \frac{0.886\lambda_1[1+(n_{o1}/n_{e1})^2\tan^2\theta]}{L\tan\theta\lvert 1-(n_{o1}/n_{e1})^2\rvert n_1^e(\theta)}$
II, oeo	$\Delta\theta = \frac{0.886\lambda_2[1+(n_{o2}/n_{e2})^2\tan^2\theta]}{L\tan\theta\lvert 1-(n_{o2}/n_{e2})^2\rvert n_2^e(\theta)}$

Table A.3: Equations for calculating the SHG temperature bandwidth for the different types of phase matching interactions.

Type of interaction	Temperature bandwidth for SHG ($\omega_1 + \omega_1 = \omega_2$)
I, ooe	$\Delta T = \frac{0.443\lambda_1}{L}\lvert\frac{\partial n_{o1}}{\partial T} - \frac{\partial n_2^e(\theta)}{\partial T}\rvert^{-1}$
II & III, eoe & oee	$\Delta T = \frac{0.886\lambda_1}{L}\lvert\frac{\partial n_1^e(\theta)}{\partial T} + \frac{\partial n_{o1}}{\partial T} - \frac{2\partial n_2^e(\theta)}{\partial T}\rvert^{-1}$
I, eeo	$\Delta T = \frac{0.443\lambda_1}{L}\lvert\frac{\partial n_{o2}}{\partial T} - \frac{\partial n_1^e(\theta)}{\partial T}\rvert^{-1}$
II & III, eoo & oeo	$\Delta T = \frac{0.886\lambda_1}{L}\lvert\frac{\partial n_1^e(\theta)}{\partial T} + \frac{\partial n_{o1}}{\partial T} - \frac{2\partial n_{o2}}{\partial T}\rvert^{-1}$

Table A.4: Equations for calculating the SFG temperature bandwidth for the different types of phase matching interactions.

Type of interaction	Temperature bandwidth for SFG ($\omega_1 + \omega_2 = \omega_3$)
I, ooe	$\Delta T = \frac{0.886}{L}\lvert\frac{\partial n_{o1}}{\lambda_1\partial T} + \frac{\partial n_{o2}}{\lambda_2\partial T} - \frac{\partial n_3^e(\theta)}{\lambda_3\partial T}\rvert^{-1}$
II, eoe	$\Delta T = \frac{0.886}{L}\lvert\frac{\partial n_1^e(\theta)}{\lambda_1\partial T} + \frac{\partial n_{o2}}{\lambda_2\partial T} - \frac{\partial n_3^e(\theta)}{\lambda_3\partial T}\rvert^{-1}$
III, oee	$\Delta T = \frac{0.886}{L}\lvert\frac{\partial n_{o1}}{\lambda_1\partial T} + \frac{\partial n_2^e(\theta)}{\lambda_2\partial T} - \frac{\partial n_3^e(\theta)}{\lambda_3\partial T}\rvert^{-1}$
I, eeo	$\Delta T = \frac{0.886}{L}\lvert\frac{\partial n_1^e(\theta)}{\lambda_1\partial T} + \frac{\partial n_1^e(\theta)}{\lambda_2\partial T} - \frac{\partial n_{o3}}{\lambda_3\partial T}\rvert^{-1}$
II, eoo	$\Delta T = \frac{0.886}{L}\lvert\frac{\partial n_1^e(\theta)}{\lambda_1\partial T} + \frac{\partial n_{o2}}{\lambda_2\partial T} - \frac{\partial n_{o3}}{\lambda_3\partial T}\rvert^{-1}$
II, oeo	$\Delta T = \frac{0.886}{L}\lvert\frac{\partial n_{o1}}{\lambda_1\partial T} + \frac{\partial n_2^e(\theta)}{\lambda_2\partial T} - \frac{\partial n_{o3}}{\lambda_3\partial T}\rvert^{-1}$

Table A.5: Equations for calculating the SHG spectral bandwidth for the different types of phase matching interactions.

Type of interaction	Spectral bandwidth for SHG ($\omega_1 + \omega_1 = \omega_2$)
I, ooe	$\Delta\nu_1 = \frac{0.443\lambda_1}{L}\lvert\frac{\partial n_{o1}}{\partial\lambda_1} - \frac{\partial n_2^e(\theta)}{\partial\lambda_2}\rvert^{-1}$
II & III, eoe & oee	$\Delta\nu_2 = \frac{0.886\lambda_1}{L}\lvert\frac{\partial n_1^e(\theta)}{\partial\lambda_1} + \frac{\partial n_{o1}}{\partial\lambda_1} - \frac{2\partial n_2^e(\theta)}{\partial\lambda_2}\rvert^{-1}$
I, eeo	$\Delta\nu_1 = \frac{0.443\lambda_1}{L}\lvert\frac{\partial n_{o2}}{\partial\lambda_2} - \frac{\partial n_1^e(\theta)}{\partial\lambda_1}\rvert^{-1}$
II & III, eoo & oeo	$\Delta\nu_1 = \frac{0.886\lambda_1}{L}\lvert\frac{\partial n_1^e(\theta)}{\partial\lambda_1} + \frac{\partial n_{o1}}{\partial\lambda_1} - \frac{2\partial n_{o2}}{\partial\lambda_2}\rvert^{-1}$

Table A.6: Equations for calculating the SFG spectral bandwidth when the higher frequency wave has a wideband spectrum

Type of interaction	Spectral bandwidth for SFG ($\omega_1 + \omega_2 = \omega_3$), λ_1 : $fixedwavelength, \lambda_2 : widebandspectrum$)
I, ooe	$\Delta\nu_2 = \frac{0.886}{L}\lvert n_{o2} - n_3^e(\theta) - \frac{\lambda_2\partial n_{o2}}{\partial\lambda_2} + \frac{\lambda_3\partial n_3^e(\theta)}{\partial\lambda_3}\rvert^{-1}$
II, eoe	$\Delta\nu_2 = \frac{0.886}{L}\lvert n_2^e(\theta) - n_3^e(\theta) - \frac{\lambda_2\partial n_2^e(\theta)}{\partial\lambda_2} + \frac{\lambda_3\partial n_3^e(\theta)}{\partial\lambda_3}\rvert^{-1}$
III, oee	$\Delta\nu_1 = \frac{0.886}{L}\lvert n_2^e(\theta) - n_3^e(\theta) - \frac{\lambda_2\partial n_2^e(\theta)}{\partial\lambda_2} + \frac{\lambda_3\partial n_3^e(\theta)}{\partial\lambda_3}\rvert^{-1}$
I, eeo	$\Delta\nu_2 = \frac{0.886}{L}\lvert n_2^e(\theta) - n_{o3} - \frac{\lambda_2\partial n_2^e(\theta)}{\partial\lambda_2} + \frac{\lambda_3\partial n_{o3}}{\partial\lambda_3}\rvert^{-1}$
II, eoo	$\Delta\nu_2 = \frac{0.886}{L}\lvert n_2^e(\theta) - n_{o3} - \frac{\lambda_2\partial n_{o2}}{\partial\lambda_2} + \frac{\lambda_3\partial n_{o3}}{\partial\lambda_3}\rvert^{-1}$
II, oeo	$\Delta\nu_2 = \frac{0.886}{L}\lvert n_2^e(\theta) - n_{o3} - \frac{\lambda_2\partial n_2^e(\theta)}{\partial\lambda_2} + \frac{\lambda_3\partial n_{o3}}{\partial\lambda_3}\rvert^{-1}$

A.3 Software using Runga-Kutta method to solve energy flow differential equations 2.17, 2.18 and 2.19

Please see the code at the end of this thesis.

Appendix B Experimental details

First, the timing of the ionizing voltage pulse should be adjusted so that the laser fires during the pulse. Electrons generated by the laser will be accelerated toward the detector. Grounding plugs should be inserted into the SHV feedthroughs for the post-extraction grid and the μ-metal tube, and then removed. It should be noted if the initial signal from electrons striking the detector appears strong on the oscilloscope when the plugs are removed, but then fades away. If so, the grid and tube should again be grounded momentarily, and the signal reobserved. The process of grounding the grid and tube when the signal fades should be repeated several times over a period of $\sim$15 minutes. The signal should decay rapidly at first, and more slowly after several cycles. When the signal persists for several minutes, the grid and tube should be connected to the 9 V battery, whereupon the signal level should remain constant. If the timing of the ZEKE-PFI ionization pulse is now set to a value appropriate for ZEKE-PFI experiments, ZEKE-PFI signal should be observed when the OPO is tuned to an appropriate wavelength.

B.1 The General Valve

The driver circuit described in D.A. Rodham's thesis now accepts external triggers. A varistor has also been inserted to clamp voltage spikes over 350 Volts. Occasionally, power failures in the lab have damaged the driver circuit. Inspecting the pulse shape with a x100 probe on the DSO can be used to see if the circuit is functioning properly. Another note of caution regarding the General Valve is that the valve itself will fail after use at temperatures of 170° C or above.

B.2 Data collection software

The core code for performing the dynamic regression on the calibration table used in the type II BBO OPO was written in Microsoft VisualBasic 5.0, and is presented below. Please see the comments in the code for additional details.

```
Private Sub CONVER()
'C********************************************************** 'C 'C
The program for conversion efficiency of plane wave 'C 'C
Written by Sheng Wu, April 1999 'C
'C**********************************************************


      Static R1, R2, R3, H, TE1, Q, F

If FileChange = True Then
      ResultFile = ResultF.TEXT
      ParaFile = ResultFile + "P"
      ResultFileA = ResultF.TEXT + "A"
      ResultFile2 = ResultF.TEXT + "_3"
      ResultFile = ResultFile + ".txt"
      ParaFile = ParaFile + ".txt"
      ResultFileA = ResultFileA + ".txt"
      ResultFile2 = ResultFile2 + ".txt"

      Open ResultFile For Output As #11
      Open ResultFileA For Output As #13
      Open ResultFile2 For Output As #14
      Open ParaFile For Output As #12
            Print #12, "INPUT POWER:"
          For i = 1 To 3
            Print #12, "Wave"; i, POWER(i), "MW/cm2", PHASE(i), "RAD"
          Next i
          Print #12, "Divergence of laser:  ", DIVERG, "RAD"
          Print #12, "Crystal length:       ", TE, "mm"
          Print #12, "Increment:            ", HHH, "mm"
```

```
          Print #12, "UTD1          ", UNIT_TD1
          Print #12, "UTD2          ", UNIT_TD2
 Close #12
      Print #11, "Xtl (mm)"; ","; "Effi.%"
      PF = 1
      For P = 1 To PF

      R1 = POWER(1) * P / PF: R2 = POWER(2) * P / PF
      'R1 = POWER(1)
      'R2 = POWER(2)
      R3 = POWER(3)

      TDIVERG = 0: RRR30 = 0
      H = HHH
      TE1 = TE
      B(1, 1) = 0#
      H1 = 1# * TE1
      For i = 1 To 3
        RN3(i) = RR(i)
        WL(i) = WW(i)
      Next i

'C---- Initial value of input density (MW/cm2)
      Q = Sqr(R1 + R2 + R3)
      B(1, 1) = 0#
      B(1, 2) = (Sqr(R1) / Q) * Cos(PHASE(1))
      B(1, 3) = (Sqr(R1) / Q) * Sin(PHASE(1))
      B(1, 4) = (Sqr(R2) / Q) * Cos(PHASE(2))
      B(1, 5) = (Sqr(R2) / Q) * Sin(PHASE(2))
      B(1, 6) = (Sqr(R3) / Q) * Cos(PHASE(3))
```

```
      B(1, 7) = (Sqr(R3) / Q) * Sin(PHASE(3))
'C
      QZ = 0.01724723 * Sqr(Q * Q * DE * DE / (RN3(1) * RN3(2) * RN3(3)))
'C



      DK = 0.6283185 * (TDIVERG + DIVERG) / (DA * QZ)

      ' TDIVERG is the divergence introduced by thermal effect
      'DK = 0.6283185 * DIVERG / (DA * QZ)



'C---- T: Crystal thickness; H: increment of thickness (in mm)
      B(1, 1) = B(1, 1) * QZ
      H = H * QZ
      H1 = H1 * QZ
      TE1 = TE1 * QZ
      For i = 1 To 3
          DEFF2(i) = 1# / WL(i)
      Next i
      k = 1  ' counting the K th plate
     ' CPT = H1
'C 'C---- Solution of differential equation 'C
      Call RK3(H, 1)

15    Call RK3(H, 4)
      RRR1 = (B(1, 2) * B(1, 2) + B(1, 3) * B(1, 3)) * Q * Q
      RRR2 = (B(1, 4) * B(1, 4) + B(1, 5) * B(1, 5)) * Q * Q
      RRR3 = (B(1, 6) * B(1, 6) + B(1, 7) * B(1, 7)) * Q * Q
TDIVERG = UNIT_TD1 * (RRR3 - RRR30) + UNIT_TD2 * (RRR3 - RRR30) *
```

```
(RRR3 - RRR30) DK = 0.6283185 * (TDIVERG + DIVERG) / (DA * QZ)


If P = PF Then Print #11, B(1, 1) / QZ; ",", RRR3 / (RRR1 + RRR2 +
RRR3) End If

Print #14, 2 * P / PF * POWER(1); ","; B(1, 1) / QZ; ",", RRR3 /
(RRR1 + RRR2 + RRR3)

If NPlateYN Then
 If Abs((B(1, 1) / QZ / HHH) - Int(SPlate(k) / HHH)) < 0.000000001 Then
       If k < 10 Then k = k + 1
      TDIVERG = 0
      RRR30 = RRR3
 End If
End If
      If (B(1, 1) < TE1 - 0.0000000001) Then GoTo 15
      T1 = B(1, 1) / QZ
      RRR1 = (B(1, 2) * B(1, 2) + B(1, 3) * B(1, 3)) * Q * Q
      RRR2 = (B(1, 4) * B(1, 4) + B(1, 5) * B(1, 5)) * Q * Q
      RRR3 = (B(1, 6) * B(1, 6) + B(1, 7) * B(1, 7)) * Q * Q

      Print #10, "OUTPUT:"
      Print #10, WW(1); "um", RRR1, "   MW/cm2    "
      Print #10, WW(2); "um", RRR2, "   MW/cm2    "
      Print #10, WW(3); "um", RRR3, "   MW/cm2    "

      POWEROUT(1) = RRR1
      POWEROUT(2) = RRR2
      POWEROUT(3) = RRR3
```

```
Print #13, P; ",", RRR3 / (RRR1 + RRR2 + RRR3)
    'Next TEO
    Next P
    Close #11
    Close #13
    Close #14
Else
    MsgBox ("change the file name,please")
End If End Sub


Private Sub RK3(H, LLL)
      Static RK3D(5)
      RK3D(3) = H
      RK3D(4) = H
      RK3D(1) = H / 2#
      RK3D(2) = RK3D(1)
      RK3D(5) = RK3D(1)
      For k = 1 To LLL
        For i = 1 To 7
            If ((LLL < 3) Or (LLL = 3)) Then GoTo 3
            B(1, i) = B(1, i) + RK3D(k + 1) * B(4, i) / 3#
            If (k <> LLL) Then GoTo 4
3           B(2, i) = B(1, i)
            B(3, i) = B(1, i)
            GoTo 2
4           B(3, i) = B(2, i) + RK3D(k) * B(4, i) 2        Next i
1       Call RK3F(B())
      Next k
```

```
End Sub

Private Sub RK3F(C())

      Static X0, Y0


''C
      X0 = Cos(DK * C(3, 1))
      Y0 = Sin(DK * C(3, 1))
      C(4, 1) = 1
      C(4, 3) = DEFF2(1) * ((C(3, 4) * C(3, 6) + C(3, 5) * C(3, 7)) * X0 -
      (C(3, 4) * C(3, 7) - C(3, 5) * C(3, 6)) * Y0)
      C(4, 2) = -DEFF2(1) * ((C(3, 4) * C(3, 7) - C(3, 5) * C(3, 6)) * X0 +
      (C(3, 4) * C(3, 6) + C(3, 5) * C(3, 7)) * Y0)
      C(4, 5) = DEFF2(2) * ((C(3, 2) * C(3, 6) + C(3, 3) * C(3, 7)) * X0 -
      (C(3, 2) * C(3, 7) - C(3, 3) * C(3, 6)) * Y0)
      C(4, 4) = -DEFF2(2) * ((C(3, 2) * C(3, 7) - C(3, 3) * C(3, 6)) * X0 +
      (C(3, 2) * C(3, 6) + C(3, 3) * C(3, 7)) * Y0)
      C(4, 7) = DEFF2(3) * ((C(3, 4) * C(3, 2) - C(3, 5) * C(3, 3)) * X0 +
      (C(3, 4) * C(3, 3) + C(3, 5) * C(3, 2)) * Y0)
      C(4, 6) = -DEFF2(3) * ((C(3, 4) * C(3, 3) + C(3, 5) * C(3, 2)) * X0 -
      (C(3, 4) * C(3, 2) - C(3, 5) * C(3, 3)) * Y0)


End Sub
```

```
*****************************************************************
The program below is the programs for scanning the OPO controlled
by digital acuators , only the core part is included.
*****************************************************************

Sub SecondRegPos1X(NuAxisPos As Long, NuAxisPosN, N%, OK)

' this subroutine calculates the #N (N=2,3, ...) Axis
' Position (NuAxisPos2) from a given axis position (NuAxisPos)
' AvrgNPos# is the average of the #N crystal position
' AvrgNPos2# is the average of the square of the #N crystal position
' AvrgXtl# is the average of the #1 crystal position
' AvrgXtl2# is the average of the square of the #1 crystal position

' N: Axis number,
' NumReg%: number of points used for regression


If NumReg%(N%) > 0 Then
If Numcal > NumReg%(N%) Then

' NumReg%(N%)must be an even number
If CalibPos(1, 1) < CalibPos(1, Numcal) Then
    MidNum% = 1
    For i = 1 To Numcal
        If CalibPos(1, i) > NuAxisPos Then
         MidNum% = i
        i = Numcal
        End If
    Next i
```

```
Else
    MidNum% = Numcal
    For i = 1 To Numcal
       If CalibPos(1, i) < NuAxisPos Then
        MidNum% = i
        i = Numcal
    End If
    Next i
End If

AvrgNPos# = 0
If MidNum% < NumReg%(N%) / 2 Then
  For t% = 1 To NumReg%(N%)
  AvrgNPos# = CalibPos(N%, t%) + AvrgNPos#
  Next t%
Else
 If MidNum% + NumReg%(N%) / 2 > Numcal Then
  For t% = Numcal - NumReg%(N%) + 1 To Numcal
  AvrgNPos# = CalibPos(N%, t%) + AvrgNPos#
  Next t%
 Else
  For t% = -NumReg%(N%) / 2 + 1 To NumReg%(N%) / 2
   AvrgNPos# = CalibPos(N%, t% + MidNum%) + AvrgNPos#
  Next t%
 End If
End If
AvrgNPos# = AvrgNPos# / NumReg%(N%)

AvrgXtl# = 0
If MidNum% < NumReg%(N%) / 2 Then
```

```
  For t% = 1 To NumReg%(N%)
  AvrgXtl# = CalibPos(1, t%) + AvrgXtl#
  Next t%
Else
 If MidNum% + NumReg%(N%) / 2 > Numcal Then
  For t% = Numcal - NumReg%(N%) + 1 To Numcal
  AvrgXtl# = CalibPos(1, t%) + AvrgXtl#
  Next t%
 Else
  For t% = -NumReg%(N%) / 2 + 1 To NumReg%(N%) / 2
   AvrgXtl# = CalibPos(1, t% + MidNum%) + AvrgXtl#
  Next t%
 End If
End If
AvrgXtl# = AvrgXtl# / NumReg%(N%)

AvrgNPos2# = 0
If MidNum% < NumReg%(N%) / 2 Then
  For t% = 1 To NumReg%(N%)
  AvrgNPos2# = CalibPos(N%, t%) ^ 2 + AvrgNPos2#
  Next t%
Else
 If MidNum% + NumReg%(N%) / 2 > Numcal Then
  For t% = Numcal - NumReg%(N%) + 1 To Numcal
     AvrgNPos2# = CalibPos(N%, t%) ^ 2 + AvrgNPos2#
  Next t%
 Else
  For t% = -NumReg%(N%) / 2 + 1 To NumReg%(N%) / 2
   AvrgNPos2# = CalibPos(N%, t% + MidNum%) ^ 2 + AvrgNPos2#
  Next t%
```

```
 End If
End If
AvrgNPos2# = AvrgNPos2# / NumReg%(N%)

AvrgXtl2# = 0
If MidNum% < NumReg%(N%) / 2 Then
  For t% = 1 To NumReg%(N%)
  AvrgXtl2# = CalibPos(1, t%) ^ 2 + AvrgXtl2#
  Next t%
Else
 If MidNum% + NumReg%(N%) / 2 > Numcal Then
  For t% = Numcal - NumReg%(N%) + 1 To Numcal
    AvrgXtl2# = CalibPos(1, t%) ^ 2 + AvrgXtl2#
  Next t%
 Else
  For t% = -NumReg%(N%) / 2 + 1 To NumReg%(N%) / 2
   AvrgXtl2# = CalibPos(1, t% + MidNum%) ^ 2 + AvrgXtl2#
  Next t%
 End If
End If
AvrgXtl2# = AvrgXtl2# / NumReg%(N%)


F1# = 0
If MidNum% < NumReg%(N%) / 2 Then
  For t% = 1 To NumReg%(N%)
  F1# = (CalibPos(N%, t%) - AvrgNPos#) *
  (CalibPos(1, t%) - AvrgXtl#) + F1#
  Next t%
Else
```

```
 If MidNum% + NumReg%(N%) / 2 > Numcal Then
  For t% = Numcal - NumReg%(N%) + 1 To Numcal
  F1# = (CalibPos(N%, t%) - AvrgNPos#) *
  (CalibPos(1, t%) - AvrgXtl#) + F1#
  Next t%
 Else
  For t% = -NumReg%(N%) / 2 + 1 To NumReg%(N%) / 2
   F1# = (CalibPos(N%, t% + MidNum%) - AvrgNPos#) *
   (CalibPos(1, t% + MidNum%)
   - AvrgXtl#) + F1#
  Next t%
 End If
End If



F2# = 0
If MidNum% < NumReg%(N%) / 2 Then
  For t% = 1 To NumReg%(N%)
  F2# = (CalibPos(1, t%) ^ 2 - AvrgXtl2#) ^ 2 + F2#
  Next t%
Else
 If MidNum% + NumReg%(N%) / 2 > Numcal Then
  For t% = Numcal - NumReg%(N%) + 1 To Numcal
  F2# = (CalibPos(1, t%) ^ 2 - AvrgXtl2#) ^ 2 + F2#
  Next t%
 Else
  For t% = -NumReg%(N%) / 2 + 1 To NumReg%(N%) / 2
   F2# = (CalibPos(1, t% + MidNum%) ^ 2 - AvrgXtl2#) ^ 2 + F2#
  Next t%
```

```
 End If
End If


F3# = 0
If MidNum% < NumReg%(N%) / 2 Then
  For t% = 1 To NumReg%(N%)
  F3# = (CalibPos(1, t%) ^ 2 - AvrgXtl2#) *
  (CalibPos(N%, t%) - AvrgNPos#) + F3#
  Next t%
Else
 If MidNum% + NumReg%(N%) / 2 > Numcal Then
  For t% = Numcal - NumReg%(N%) + 1 To Numcal
  F3# = (CalibPos(1, t%) ^ 2 - AvrgXtl2#) *
  (CalibPos(N%, t%) - AvrgNPos#) + F3#
  Next t%
 Else
  For t% = -NumReg%(N%) / 2 + 1 To NumReg%(N%) / 2
   F3# = (CalibPos(1, t% + MidNum%) ^ 2 - AvrgXtl2#)
   (CalibPos(N%, t% + MidNum%)
   - AvrgNPos#) + F3#
  Next t%
 End If
End If


F4# = 0
If MidNum% < NumReg%(N%) / 2 Then
  For t% = 1 To NumReg%(N%)
  F4# = (CalibPos(1, t%) ^ 2 - AvrgXtl2#) *
```

```
  (CalibPos(1, t%) - AvrgXtl#) + F4#
  Next t%
Else
 If MidNum% + NumReg%(N%) / 2 > Numcal Then
  For t% = Numcal - NumReg%(N%) + 1 To Numcal
  F4# = (CalibPos(1, t%) ^ 2 - AvrgXtl2#) *
  (CalibPos(1, t%) - AvrgXtl#) + F4#
  Next t%
 Else
  For t% = -NumReg%(N%) / 2 + 1 To NumReg%(N%) / 2
   F4# = (CalibPos(1, t% + MidNum%) ^ 2 - AvrgXtl2#) *
   (CalibPos(1, t% + MidNum%)
   - AvrgXtl#) + F4#
  Next t%
 End If
End If


F5# = 0
If MidNum% < NumReg%(N%) / 2 Then
  For t% = 1 To NumReg%(N%)
  F5# = (CalibPos(1, t%) - AvrgXtl#) ^ 2 + F5#
  Next t%
Else
 If MidNum% + NumReg%(N%) / 2 > Numcal Then
  For t% = Numcal - NumReg%(N%) + 1 To Numcal
  F5# = (CalibPos(1, t%) - AvrgXtl#) ^ 2 + F5#
  Next t%
 Else
  For t% = -NumReg%(N%) / 2 + 1 To NumReg%(N%) / 2
```

```
   F5# = (CalibPos(1, t% + MidNum%) - AvrgXtl#) ^ 2 + F5#
  Next t%
 End If
End If


beta2# = (F1# * F2# - F3# * F4#) / (F5# * F2# - F4# * F4#)
beta3# = (F3# * F5# - F1# * F4#) / (F5# * F2# - F4# * F4#)
beta1# = AvrgNPos# - beta2# * AvrgXtl# - beta3# * AvrgXtl2#

NuAxisPosN = beta1# + beta2# * NuAxisPos + beta3# * NuAxisPos ^ 2

OK = True
Else  ' less than 9 calibration points
MsgBox ("Need more calibration points, Axis#" + Str$(N%))
Beep
OK = False
End
End If
Else  ' regression number not set
Beep
MsgBox ("Need set regression numbers for Axis#" + Str$(N%))
OK = False
End
End If
End Sub

Sub SecondRegPos(WaveSignal, NuAxisPos As Long, OK)
' this subroutine calculates New AxisPosition (NuAxisPos)
' from a given Wavelength (WaveSignal)
```

```
If Numcal > NumReg%(1) Then

'NumReg%(1)must be an even number

        MidNum% = 1
         For i = 1 To Numcal
            If CalibWave(i) > WaveSignal Then
            MidNum% = i
            i = Numcal
            End If
         Next i

AvrgWav# = 0
If MidNum% < NumReg%(1) / 2 Then
  For t% = 1 To NumReg%(1)
  AvrgWav# = CalibWave(t%) + AvrgWav#
  Next t%
Else
 If MidNum% + NumReg%(1) / 2 > Numcal Then
  For t% = Numcal - NumReg%(1) + 1 To Numcal
  AvrgWav# = CalibWave(t%) + AvrgWav#
  Next t%
 Else
  For t% = -NumReg%(1) / 2 + 1 To NumReg%(1) / 2
   AvrgWav# = CalibWave(t% + MidNum%) + AvrgWav#
  Next t%
 End If
End If
```

```
AvrgWav# = AvrgWav# / NumReg%(1)

AvrgXtl# = 0
If MidNum% < NumReg%(1) / 2 Then
  For t% = 1 To NumReg%(1)
  AvrgXtl# = CalibPos(1, t%) + AvrgXtl#
  Next t%
Else
 If MidNum% + NumReg%(1) / 2 > Numcal Then
  For t% = Numcal - NumReg%(1) + 1 To Numcal
  AvrgXtl# = CalibPos(1, t%) + AvrgXtl#
  Next t%
 Else
  For t% = -NumReg%(1) / 2 + 1 To NumReg%(1) / 2
   AvrgXtl# = CalibPos(1, t% + MidNum%) + AvrgXtl#
  Next t%
 End If
End If
AvrgXtl# = AvrgXtl# / NumReg%(1)

AvrgWav2# = 0
If MidNum% < NumReg%(1) / 2 Then
  For t% = 1 To NumReg%(1)
  AvrgWav2# = CalibWave(t%) ^ 2 + AvrgWav2#
  Next t%
Else
 If MidNum% + NumReg%(1) / 2 > Numcal Then
  For t% = Numcal - NumReg%(1) + 1 To Numcal
     AvrgWav2# = CalibWave(t%) ^ 2 + AvrgWav2#
  Next t%
```

```
 Else
  For t% = -NumReg%(1) / 2 + 1 To NumReg%(1) / 2
   AvrgWav2# = CalibWave(t% + MidNum%) ^ 2 + AvrgWav2#
  Next t%
 End If
End If
AvrgWav2# = AvrgWav2# / NumReg%(1)

AvrgXtl2# = 0
If MidNum% < NumReg%(1) / 2 Then
  For t% = 1 To NumReg%(1)
  AvrgXtl2# = CalibPos(1, t%) ^ 2 + AvrgXtl2#
  Next t%
Else
 If MidNum% + NumReg%(1) / 2 > Numcal Then
  For t% = Numcal - NumReg%(1) + 1 To Numcal
    AvrgXtl2# = CalibPos(1, t%) ^ 2 + AvrgXtl2#
  Next t%
 Else
  For t% = -NumReg%(1) / 2 + 1 To NumReg%(1) / 2
   AvrgXtl2# = CalibPos(1, t% + MidNum%) ^ 2 + AvrgXtl2#
  Next t%
 End If
End If
AvrgXtl2# = AvrgXtl2# / NumReg%(1)

F1# = 0
If MidNum% < NumReg%(1) / 2 Then
  For t% = 1 To NumReg%(1)
  F1# = (CalibWave(t%) - AvrgWav#) *
```

```
  (CalibPos(1, t%) - AvrgXtl#) + F1#
  Next t%
Else
 If MidNum% + NumReg%(1) / 2 > Numcal Then
  For t% = Numcal - NumReg%(1) + 1 To Numcal
  F1# = (CalibWave(t%) - AvrgWav#) *
  (CalibPos(1, t%) - AvrgXtl#) + F1#
  Next t%
 Else
  For t% = -NumReg%(1) / 2 + 1 To NumReg%(1) / 2
   F1# = (CalibWave(t% + MidNum%) - AvrgWav#) *
   (CalibPos(1, t% + MidNum%)
    - AvrgXtl#) + F1#
  Next t%
 End If
End If


F2# = 0
If MidNum% < NumReg%(1) / 2 Then
  For t% = 1 To NumReg%(1)
  F2# = (CalibWave(t%) ^ 2 - AvrgWav2#) ^ 2 + F2#
  Next t%
Else
 If MidNum% + NumReg%(1) / 2 > Numcal Then
  For t% = Numcal - NumReg%(1) + 1 To Numcal
  F2# = (CalibWave(t%) ^ 2 - AvrgWav2#) ^ 2 + F2#
  Next t%
 Else
    For t% = -NumReg%(1) / 2 + 1 To NumReg%(1) / 2
```

```
    F2# = (CalibWave(t% + MidNum%) ^ 2 - AvrgWav2#) ^ 2 + F2#
    Next t%
 End If
End If


F3# = 0
If MidNum% < NumReg%(1) / 2 Then
  For t% = 1 To NumReg%(1)
  F3# = (CalibWave(t%) ^ 2 - AvrgWav2#) *
  (CalibPos(1, t%) - AvrgXtl#) + F3#
  Next t%
Else
 If MidNum% + NumReg%(1) / 2 > Numcal Then
  For t% = Numcal - NumReg%(1) + 1 To Numcal
  F3# = (CalibWave(t%) ^ 2 - AvrgWav2#) *
  (CalibPos(1, t%) - AvrgXtl#) + F3#
  Next t%
 Else
  For t% = -NumReg%(1) / 2 + 1 To NumReg%(1) / 2
   F3# = (CalibWave(t% + MidNum%) ^ 2 - AvrgWav2#) *
   (CalibPos(1, t% + MidNum%)
    - AvrgXtl#) + F3#
  Next t%
 End If
End If


F4# = 0
If MidNum% < NumReg%(1) / 2 Then
```

```
  For t% = 1 To NumReg%(1)
  F4# = (CalibWave(t%) ^ 2 - AvrgWav2#) *
  (CalibWave(t%) - AvrgWav#) + F4#
  Next t%
Else
 If MidNum% + NumReg%(1) / 2 > Numcal Then
  For t% = Numcal - NumReg%(1) + 1 To Numcal
  F4# = (CalibWave(t%) ^ 2 - AvrgWav2#) *
  (CalibWave(t%) - AvrgWav#) + F4#
  Next t%
 Else
  For t% = -NumReg%(1) / 2 + 1 To NumReg%(1) / 2
   F4# = (CalibWave(t% + MidNum%) ^ 2 - AvrgWav2#)
   (CalibWave(t% + MidNum%)
   - AvrgWav#) + F4#
  Next t%
 End If
End If


F5# = 0
If MidNum% < NumReg%(1) / 2 Then
  For t% = 1 To NumReg%(1)
  F5# = (CalibWave(t%) - AvrgWav#) ^ 2 + F5#
  Next t%
Else
 If MidNum% + NumReg%(1) / 2 > Numcal Then
  For t% = Numcal - NumReg%(1) + 1 To Numcal
  F5# = (CalibWave(t%) - AvrgWav#) ^ 2 + F5#
  Next t%
```

```
 Else
  For t% = -NumReg%(1) / 2 + 1 To NumReg%(1) / 2
   F5# = (CalibWave(t% + MidNum%) - AvrgWav#) ^ 2 + F5#
  Next t%
 End If
End If


beta2# = (F1# * F2# - F3# * F4#) / (F5# * F2# - F4# * F4#)
beta3# = (F3# * F5# - F1# * F4#) / (F5# * F2# - F4# * F4#)
beta1# = AvrgXtl# - beta2# * AvrgWav# - beta3# * AvrgWav2#

NuAxisPos = beta1# + beta2# * WaveSignal + beta3# * WaveSignal ^ 2

OK = True

Else ' if less than 9 calibration points

OK = False
End If

End Sub

Sub SecondRegPos2(NuAxisPos As Long, NuAxisPos2, OK)
' this subroutine calculates the #2 Axis Position
' (NuAxisPos2) from a given axis position (NuAxisPos)
' Avrg2Pos# is the average of the #2 crystal position
' Avrg2Pos2# is the average of the square of the #2 crystal position
' AvrgXtl# is the average of the #1 crystal position
' AvrgXtl2# is the average of the square of the #1 crystal position
```

```
Static NumReg%

If Numcal > 8 Then

'must be an even number
NumReg% = 8
'must be an even number

        MidNum% = 1
         For i = 1 To Numcal
            If CalibPos(1, i) > NuAxisPos Then
            MidNum% = i
            i = Numcal
            End If
         Next i

Avrg2Pos# = 0
If MidNum% < NumReg% / 2 Then
  For t% = 1 To NumReg%
  Avrg2Pos# = CalibPos(2, t%) + Avrg2Pos#
  Next t%
Else
 If MidNum% + NumReg% / 2 > Numcal Then
  For t% = Numcal - NumReg% + 1 To Numcal
  Avrg2Pos# = CalibPos(2, t%) + Avrg2Pos#
  Next t%
 Else
  For t% = -NumReg% / 2 + 1 To NumReg% / 2
   Avrg2Pos# = CalibPos(2, t% + MidNum%) + Avrg2Pos#
```

```
  Next t%
 End If
End If
Avrg2Pos# = Avrg2Pos# / NumReg%

AvrgXtl# = 0
If MidNum% < NumReg% / 2 Then
  For t% = 1 To NumReg%
  AvrgXtl# = CalibPos(1, t%) + AvrgXtl#
  Next t%
Else
 If MidNum% + NumReg% / 2 > Numcal Then
  For t% = Numcal - NumReg% + 1 To Numcal
  AvrgXtl# = CalibPos(1, t%) + AvrgXtl#
  Next t%
 Else
  For t% = -NumReg% / 2 + 1 To NumReg% / 2
   AvrgXtl# = CalibPos(1, t% + MidNum%) + AvrgXtl#
  Next t%
 End If
End If
AvrgXtl# = AvrgXtl# / NumReg%

Avrg2Pos2# = 0
If MidNum% < NumReg% / 2 Then
  For t% = 1 To NumReg%
  Avrg2Pos2# = CalibPos(2, t%) ^ 2 + Avrg2Pos2#
  Next t%
Else
 If MidNum% + NumReg% / 2 > Numcal Then
```

```
  For t% = Numcal - NumReg% + 1 To Numcal
     Avrg2Pos2# = CalibPos(2, t%) ^ 2 + Avrg2Pos2#
  Next t%
 Else
  For t% = -NumReg% / 2 + 1 To NumReg% / 2
   Avrg2Pos2# = CalibPos(2, t% + MidNum%) ^ 2 + Avrg2Pos2#
  Next t%
 End If
End If
Avrg2Pos2# = Avrg2Pos2# / NumReg%

AvrgXtl2# = 0
If MidNum% < NumReg% / 2 Then
  For t% = 1 To NumReg%
  AvrgXtl2# = CalibPos(1, t%) ^ 2 + AvrgXtl2#
  Next t%
Else
 If MidNum% + NumReg% / 2 > Numcal Then
  For t% = Numcal - NumReg% + 1 To Numcal
    AvrgXtl2# = CalibPos(1, t%) ^ 2 + AvrgXtl2#
  Next t%
 Else
  For t% = -NumReg% / 2 + 1 To NumReg% / 2
   AvrgXtl2# = CalibPos(1, t% + MidNum%) ^ 2 + AvrgXtl2#
  Next t%
 End If
End If
AvrgXtl2# = AvrgXtl2# / NumReg%
```

```
F1# = 0
If MidNum% < NumReg% / 2 Then
  For t% = 1 To NumReg%
  F1# = (CalibPos(2, t%) - Avrg2Pos#) *
  (CalibPos(1, t%) - AvrgXtl#) + F1#
  Next t%
Else
 If MidNum% + NumReg% / 2 > Numcal Then
  For t% = Numcal - NumReg% + 1 To Numcal
  F1# = (CalibPos(2, t%) - Avrg2Pos#) * (CalibPos(1, t%) - AvrgXtl#) + F1#
  Next t%
 Else
  For t% = -NumReg% / 2 + 1 To NumReg% / 2
   F1# = (CalibPos(2, t% + MidNum%) - Avrg2Pos#) *
   (CalibPos(1, t% + MidNum%)
   - AvrgXtl#) + F1#
  Next t%
 End If
End If



F2# = 0
If MidNum% < NumReg% / 2 Then
  For t% = 1 To NumReg%
  F2# = (CalibPos(1, t%) ^ 2 - AvrgXtl2#) ^ 2 + F2#
  Next t%
Else
 If MidNum% + NumReg% / 2 > Numcal Then
  For t% = Numcal - NumReg% + 1 To Numcal
```

```
  F2# = (CalibPos(1, t%) ^ 2 - AvrgXtl2#) ^ 2 + F2#
  Next t%
 Else
  For t% = -NumReg% / 2 + 1 To NumReg% / 2
   F2# = (CalibPos(1, t% + MidNum%) ^ 2 - AvrgXtl2#) ^ 2 + F2#
  Next t%
 End If
End If


F3# = 0
If MidNum% < NumReg% / 2 Then
  For t% = 1 To NumReg%
  F3# = (CalibPos(1, t%) ^ 2 - AvrgXtl2#) *
  (CalibPos(2, t%) - Avrg2Pos#) + F3#
  Next t%
Else
 If MidNum% + NumReg% / 2 > Numcal Then
  For t% = Numcal - NumReg% + 1 To Numcal
  F3# = (CalibPos(1, t%) ^ 2 - AvrgXtl2#) *
  (CalibPos(2, t%) - Avrg2Pos#) + F3#
  Next t%
 Else
  For t% = -NumReg% / 2 + 1 To NumReg% / 2
   F3# = (CalibPos(1, t% + MidNum%) ^ 2 - AvrgXtl2#) *
   (CalibPos(2, t% + MidNum%)
    - Avrg2Pos#) + F3#
  Next t%
 End If
End If
```

```
F4# = 0
If MidNum% < NumReg% / 2 Then
  For t% = 1 To NumReg%
  F4# = (CalibPos(1, t%) ^ 2 - AvrgXtl2#) *
  (CalibPos(1, t%) - AvrgXtl#) + F4#
  Next t%
Else
 If MidNum% + NumReg% / 2 > Numcal Then
  For t% = Numcal - NumReg% + 1 To Numcal
  F4# = (CalibPos(1, t%) ^ 2 - AvrgXtl2#) *
  (CalibPos(1, t%) - AvrgXtl#) + F4#
  Next t%
 Else
  For t% = -NumReg% / 2 + 1 To NumReg% / 2
   F4# = (CalibPos(1, t% + MidNum%) ^ 2 - AvrgXtl2#) *
   (CalibPos(1, t% + MidNum%)
   - AvrgXtl#) + F4#
  Next t%
 End If
End If


F5# = 0
If MidNum% < NumReg% / 2 Then
  For t% = 1 To NumReg%
  F5# = (CalibPos(1, t%) - AvrgXtl#) ^ 2 + F5#
  Next t%
Else
```

```
 If MidNum% + NumReg% / 2 > Numcal Then
  For t% = Numcal - NumReg% + 1 To Numcal
  F5# = (CalibPos(1, t%) - AvrgXtl#) ^ 2 + F5#
  Next t%
 Else
  For t% = -NumReg% / 2 + 1 To NumReg% / 2
   F5# = (CalibPos(1, t% + MidNum%) - AvrgXtl#) ^ 2 + F5#
  Next t%
 End If
End If


beta2# = (F1# * F2# - F3# * F4#) / (F5# * F2# - F4# * F4#)
beta3# = (F3# * F5# - F1# * F4#) / (F5# * F2# - F4# * F4#)
beta1# = Avrg2Pos# - beta2# * AvrgXtl# - beta3# * AvrgXtl2#

NuAxisPos2 = beta1# + beta2# * NuAxisPos + beta3# * NuAxisPos ^ 2

OK = True
Else  ' less than 9 calibration points

OK = False
End If


End Sub

Sub SecondRegPos3(NuAxisPos As Long, NuAxisPos3, OK)
' this subroutine calculates the #3 Axis Position
' (NuAxisPos2) from a given axis position (NuAxisPos)
```

```
' Avrg3Pos# is the average of the #3 crystal position
' Avrg3Pos2# is the average of the square of the #3 crystal position
' AvrgXtl# is the average of the #1 crystal position
' AvrgXtl2# is the average of the square of the #1 crystal position


Static NumReg%

If Numcal > 4 Then

'must be an even number
NumReg% = 4
'must be an even number

        MidNum% = 1
         For i = 1 To Numcal
            If CalibPos(1, i) > NuAxisPos Then
            MidNum% = i
            i = Numcal
            End If
         Next i

Avrg3Pos# = 0
If MidNum% < NumReg% / 2 Then
  For t% = 1 To NumReg%
  Avrg3Pos# = CalibPos(3, t%) + Avrg3Pos#
  Next t%
Else
 If MidNum% + NumReg% / 2 > Numcal Then
  For t% = Numcal - NumReg% + 1 To Numcal
```

```
  Avrg3Pos# = CalibPos(3, t%) + Avrg3Pos#
  Next t%
 Else
  For t% = -NumReg% / 2 + 1 To NumReg% / 2
   Avrg3Pos# = CalibPos(3, t% + MidNum%) + Avrg3Pos#
  Next t%
 End If
End If
Avrg3Pos# = Avrg3Pos# / NumReg%

AvrgXtl# = 0
If MidNum% < NumReg% / 2 Then
  For t% = 1 To NumReg%
  AvrgXtl# = CalibPos(1, t%) + AvrgXtl#
  Next t%
Else
 If MidNum% + NumReg% / 2 > Numcal Then
  For t% = Numcal - NumReg% + 1 To Numcal
  AvrgXtl# = CalibPos(1, t%) + AvrgXtl#
  Next t%
 Else
  For t% = -NumReg% / 2 + 1 To NumReg% / 2
   AvrgXtl# = CalibPos(1, t% + MidNum%) + AvrgXtl#
  Next t%
 End If
End If
AvrgXtl# = AvrgXtl# / NumReg%

Avrg3Pos2# = 0
If MidNum% < NumReg% / 2 Then
```

```
  For t% = 1 To NumReg%
  Avrg3Pos2# = CalibPos(3, t%) ^ 2 + Avrg3Pos2#
  Next t%
Else
 If MidNum% + NumReg% / 2 > Numcal Then
  For t% = Numcal - NumReg% + 1 To Numcal
     Avrg3Pos2# = CalibPos(3, t%) ^ 2 + Avrg3Pos2#
  Next t%
 Else
  For t% = -NumReg% / 2 + 1 To NumReg% / 2
   Avrg3Pos2# = CalibPos(3, t% + MidNum%) ^ 2 + Avrg3Pos2#
  Next t%
 End If
End If
Avrg3Pos2# = Avrg3Pos2# / NumReg%

AvrgXtl2# = 0
If MidNum% < NumReg% / 2 Then
  For t% = 1 To NumReg%
  AvrgXtl2# = CalibPos(1, t%) ^ 2 + AvrgXtl2#
  Next t%
Else
 If MidNum% + NumReg% / 2 > Numcal Then
  For t% = Numcal - NumReg% + 1 To Numcal
    AvrgXtl2# = CalibPos(1, t%) ^ 2 + AvrgXtl2#
  Next t%
 Else
  For t% = -NumReg% / 2 + 1 To NumReg% / 2
   AvrgXtl2# = CalibPos(1, t% + MidNum%) ^ 2 + AvrgXtl2#
  Next t%
```

```
 End If
End If
AvrgXtl2# = AvrgXtl2# / NumReg%


F1# = 0
If MidNum% < NumReg% / 2 Then
  For t% = 1 To NumReg%
  F1# = (CalibPos(3, t%) - Avrg3Pos#) *
  (CalibPos(1, t%) - AvrgXtl#) + F1#
  Next t%
Else
 If MidNum% + NumReg% / 2 > Numcal Then
  For t% = Numcal - NumReg% + 1 To Numcal
  F1# = (CalibPos(3, t%) - Avrg3Pos#) *
  (CalibPos(1, t%) - AvrgXtl#) + F1#
  Next t%
 Else
  For t% = -NumReg% / 2 + 1 To NumReg% / 2
   F1# = (CalibPos(3, t% + MidNum%) - Avrg3Pos#)
   (CalibPos(1, t% + MidNum%)
   - AvrgXtl#) + F1#
  Next t%
 End If
End If



F2# = 0
If MidNum% < NumReg% / 2 Then
```

```
  For t% = 1 To NumReg%
  F2# = (CalibPos(1, t%) ^ 2 - AvrgXtl2#) ^ 2 + F2#
  Next t%
Else
 If MidNum% + NumReg% / 2 > Numcal Then
  For t% = Numcal - NumReg% + 1 To Numcal
  F2# = (CalibPos(1, t%) ^ 2 - AvrgXtl2#) ^ 2 + F2#
  Next t%
 Else
  For t% = -NumReg% / 2 + 1 To NumReg% / 2
   F2# = (CalibPos(1, t% + MidNum%) ^ 2 - AvrgXtl2#) ^ 2 + F2#
  Next t%
 End If
End If


F3# = 0
If MidNum% < NumReg% / 2 Then
  For t% = 1 To NumReg%
  F3# = (CalibPos(1, t%) ^ 2 - AvrgXtl2#) * (CalibPos(3, t%) - Avrg3Pos#) + F3#
  Next t%
Else
 If MidNum% + NumReg% / 2 > Numcal Then
  For t% = Numcal - NumReg% + 1 To Numcal
  F3# = (CalibPos(1, t%) ^ 2 - AvrgXtl2#) *
  (CalibPos(3, t%) - Avrg3Pos#) + F3#
  Next t%
 Else
  For t% = -NumReg% / 2 + 1 To NumReg% / 2
   F3# = (CalibPos(1, t% + MidNum%) ^ 2 - AvrgXtl2#) *
```

```
   (CalibPos(3, t% + MidNum%)
   - Avrg3Pos#) + F3#
  Next t%
 End If
End If


F4# = 0
If MidNum% < NumReg% / 2 Then
  For t% = 1 To NumReg%
  F4# = (CalibPos(1, t%) ^ 2 - AvrgXtl2#) * (CalibPos(1, t%) - AvrgXtl#) + F4#
  Next t%
Else
 If MidNum% + NumReg% / 2 > Numcal Then
  For t% = Numcal - NumReg% + 1 To Numcal
  F4# = (CalibPos(1, t%) ^ 2 - AvrgXtl2#) * (CalibPos(1, t%) - AvrgXtl#) + F4#
  Next t%
 Else
  For t% = -NumReg% / 2 + 1 To NumReg% / 2
   F4# = (CalibPos(1, t% + MidNum%) ^ 2 - AvrgXtl2#) *
   (CalibPos(1, t% + MidNum%)
    - AvrgXtl#) + F4#
  Next t%
 End If
End If


F5# = 0
If MidNum% < NumReg% / 2 Then
  For t% = 1 To NumReg%
```

```
      F5# = (CalibPos(1, t%) - AvrgXtl#) ^ 2 + F5#
      Next t%
    Else
     If MidNum% + NumReg% / 2 > Numcal Then
      For t% = Numcal - NumReg% + 1 To Numcal
      F5# = (CalibPos(1, t%) - AvrgXtl#) ^ 2 + F5#
      Next t%
     Else
      For t% = -NumReg% / 2 + 1 To NumReg% / 2
       F5# = (CalibPos(1, t% + MidNum%) - AvrgXtl#) ^ 2 + F5#
      Next t%
     End If
    End If


   beta2# = (F1# * F2# - F3# * F4#) / (F5# * F2# - F4# * F4#)
   beta3# = (F3# * F5# - F1# * F4#) / (F5# * F2# - F4# * F4#)
   beta1# = Avrg3Pos# - beta2# * AvrgXtl# - beta3# * AvrgXtl2#

   NuAxisPos3 = beta1# + beta2# * NuAxisPos + beta3# * NuAxisPos ^ 2

   OK = True
   Else  ' less than 9 calibration points

   OK = False
   End If


End Sub
```

```
Sub SecondRegWav(NuAxisPos As Long, WaveSignal, OK)
' this subroutine calculates the WaveLength (WaveSignal)
' from a given axis position (NuAxisPos)
' AvrgWav# is the average of the wavelengths
' AvrgWav2# is the average of the square of the wavelengths
' AvrgXtl# is the average of the #1 crystal position
' AvrgXtl2# is the average of the square of the #1 crystal position

If Numcal > NumReg%(1) Then

'NumReg% must be an even number
    If CalibPos(1, 1) < CalibPos(1, Numcal) Then
       MidNum% = 1
       For i% = 1 To Numcal
            If CalibPos(1, i%) > NuAxisPos Then
            MidNum% = i%
            i% = Numcal
            Else
            End If
       Next i%

    Else
       MidNum% = Numcal
       For i% = 1 To Numcal
            If CalibPos(1, i%) < NuAxisPos Then
            MidNum% = i%
            i% = Numcal
            Else
            End If
       Next i%
```

```
    End If


AvrgWav# = 0
If MidNum% < NumReg%(1) / 2 Then
  For t% = 1 To NumReg%(1)
  AvrgWav# = CalibWave(t%) + AvrgWav#
  Next t%
Else
 If MidNum% + NumReg%(1) / 2 > Numcal Then
  For t% = Numcal - NumReg%(1) + 1 To Numcal
  AvrgWav# = CalibWave(t%) + AvrgWav#
  Next t%
 Else
  For t% = -NumReg%(1) / 2 + 1 To NumReg%(1) / 2
   AvrgWav# = CalibWave(t% + MidNum%) + AvrgWav#
  Next t%
 End If
End If
AvrgWav# = AvrgWav# / NumReg%(1)

AvrgXtl# = 0
If MidNum% < NumReg%(1) / 2 Then
  For t% = 1 To NumReg%(1)
  AvrgXtl# = CalibPos(1, t%) + AvrgXtl#
  Next t%
Else
 If MidNum% + NumReg%(1) / 2 > Numcal Then
  For t% = Numcal - NumReg%(1) + 1 To Numcal
  AvrgXtl# = CalibPos(1, t%) + AvrgXtl#
```

```
  Next t%
 Else
  For t% = -NumReg%(1) / 2 + 1 To NumReg%(1) / 2
   AvrgXtl# = CalibPos(1, t% + MidNum%) + AvrgXtl#
  Next t%
 End If
End If
AvrgXtl# = AvrgXtl# / NumReg%(1)

AvrgWav2# = 0
If MidNum% < NumReg%(1) / 2 Then
  For t% = 1 To NumReg%(1)
  AvrgWav2# = CalibWave(t%) ^ 2 + AvrgWav2#
  Next t%
Else
 If MidNum% + NumReg%(1) / 2 > Numcal Then
  For t% = Numcal - NumReg%(1) + 1 To Numcal
     AvrgWav2# = CalibWave(t%) ^ 2 + AvrgWav2#
  Next t%
 Else
  For t% = -NumReg%(1) / 2 + 1 To NumReg%(1) / 2
   AvrgWav2# = CalibWave(t% + MidNum%) ^ 2 + AvrgWav2#
  Next t%
 End If
End If
AvrgWav2# = AvrgWav2# / NumReg%(1)

AvrgXtl2# = 0
If MidNum% < NumReg%(1) / 2 Then
  For t% = 1 To NumReg%(1)
```

```
  AvrgXtl2# = CalibPos(1, t%) ^ 2 + AvrgXtl2#
  Next t%
Else
 If MidNum% + NumReg%(1) / 2 > Numcal Then
  For t% = Numcal - NumReg%(1) + 1 To Numcal
    AvrgXtl2# = CalibPos(1, t%) ^ 2 + AvrgXtl2#
  Next t%
 Else
  For t% = -NumReg%(1) / 2 + 1 To NumReg%(1) / 2
   AvrgXtl2# = CalibPos(1, t% + MidNum%) ^ 2 + AvrgXtl2#
  Next t%
 End If
End If
AvrgXtl2# = AvrgXtl2# / NumReg%(1)


F1# = 0
If MidNum% < NumReg%(1) / 2 Then
  For t% = 1 To NumReg%(1)
  F1# = (CalibWave(t%) - AvrgWav#) * (CalibPos(1, t%) - AvrgXtl#) +
   F1#
  Next t%
Else
 If MidNum% + NumReg%(1) / 2 > Numcal Then
  For t% = Numcal - NumReg%(1) + 1 To Numcal
  F1# = (CalibWave(t%) - AvrgWav#) * (CalibPos(1, t%) - AvrgXtl#) +
  F1#
  Next t%
 Else
  For t% = -NumReg%(1) / 2 + 1 To NumReg%(1) / 2
```

```
   F1# = (CalibWave(t% + MidNum%) - AvrgWav#) *
   (CalibPos(1, t% + MidNum%)
   - AvrgXtl#) + F1#
  Next t%
 End If
End If



F2# = 0
If MidNum% < NumReg%(1) / 2 Then
  For t% = 1 To NumReg%(1)
  F2# = (CalibPos(1, t%) ^ 2 - AvrgXtl2#) ^ 2 + F2#
  Next t%
Else
 If MidNum% + NumReg%(1) / 2 > Numcal Then
  For t% = Numcal - NumReg%(1) + 1 To Numcal
  F2# = (CalibPos(1, t%) ^ 2 - AvrgXtl2#) ^ 2 + F2#
  Next t%
 Else
  For t% = -NumReg%(1) / 2 + 1 To NumReg%(1) / 2
   F2# = (CalibPos(1, t% + MidNum%) ^ 2 - AvrgXtl2#) ^ 2 + F2#
  Next t%
 End If
End If



F3# = 0
If MidNum% < NumReg%(1) / 2 Then
  For t% = 1 To NumReg%(1)
```

```
  F3# = (CalibPos(1, t%) ^ 2 - AvrgXtl2#) *
  (CalibWave(t%) - AvrgWav#) + F3#
  Next t%
Else
 If MidNum% + NumReg%(1) / 2 > Numcal Then
  For t% = Numcal - NumReg%(1) + 1 To Numcal
  F3# = (CalibPos(1, t%) ^ 2 - AvrgXtl2#) *
  (CalibWave(t%) - AvrgWav#) + F3#
  Next t%
 Else
  For t% = -NumReg%(1) / 2 + 1 To NumReg%(1) / 2
   F3# = (CalibPos(1, t% + MidNum%) ^ 2 - AvrgXtl2#) *
   (CalibWave(t% + MidNum%)
   - AvrgWav#) + F3#
    Next t%
 End If
End If


F4# = 0
If MidNum% < NumReg%(1) / 2 Then
  For t% = 1 To NumReg%(1)
  F4# = (CalibPos(1, t%) ^ 2 - AvrgXtl2#) *
  (CalibPos(1, t%) - AvrgXtl#) + F4#
  Next t%
Else
 If MidNum% + NumReg%(1) / 2 > Numcal Then
  For t% = Numcal - NumReg%(1) + 1 To Numcal
  F4# = (CalibPos(1, t%) ^ 2 - AvrgXtl2#) *
  (CalibPos(1, t%) - AvrgXtl#) + F4#
```

```
  Next t%
 Else
  For t% = -NumReg%(1) / 2 + 1 To NumReg%(1) / 2
   F4# = (CalibPos(1, t% + MidNum%) ^ 2 - AvrgXtl2#) *
   (CalibPos(1, t% + MidNum%)
    - AvrgXtl#) + F4#
  Next t%
 End If
End If


F5# = 0
If MidNum% < NumReg%(1) / 2 Then
  For t% = 1 To NumReg%(1)
  F5# = (CalibPos(1, t%) - AvrgXtl#) ^ 2 + F5#
  Next t%
Else
 If MidNum% + NumReg%(1) / 2 > Numcal Then
  For t% = Numcal - NumReg%(1) + 1 To Numcal
  F5# = (CalibPos(1, t%) - AvrgXtl#) ^ 2 + F5#
  Next t%
 Else
  For t% = -NumReg%(1) / 2 + 1 To NumReg%(1) / 2
   F5# = (CalibPos(1, t% + MidNum%) - AvrgXtl#) ^ 2 + F5#
  Next t%
 End If
End If


beta2# = (F1# * F2# - F3# * F4#) / (F5# * F2# - F4# * F4#)
```

```
beta3# = (F3# * F5# - F1# * F4#) / (F5# * F2# - F4# * F4#)
beta1# = AvrgWav# - beta2# * AvrgXtl# - beta3# * AvrgXtl2#

WaveSignal = beta1# + beta2# * NuAxisPos + beta3# * NuAxisPos ^ 2

OK = True

Else  ' less than 7 calibration points

OK = False
End If

End Sub
Sub sortCalib()
For i = 1 To Numcal
  MinWave = CalibWave(i)
  MinPos% = i

  'find minimum
  For j = i To Numcal
  If MinWave > CalibWave(j) Then
    MinWave = CalibWave(j)
    MinPos% = j
   Else
   End If
  Next j

  'swap
  CalibWave(MinPos%) = CalibWave(i)
  CalibWave(i) = MinWave
```

```
  For AxisD = 1 To param.NumberAxes
   MinCalPos = CalibPos(AxisD, MinPos%)
   CalibPos(AxisD, MinPos%) = CalibPos(AxisD, i)
   CalibPos(AxisD, i) = MinCalPos
  Next AxisD

  Next i

  If CalibPos(1, 1) < CalibPos(1, Numcal) Then
   LowLimitMotor = CalibPos(1, 1)
   UpLimitMotor = CalibPos(1, Numcal)
  Else
   UpLimitMotor = CalibPos(1, 1)
   LowLimitMotor = CalibPos(1, Numcal)
  End If

End Sub



**********************************************************************
**********************************************************************
' This subroutine shows how to use the regression subroutines
above to calculate positions for each axis

 Private Sub GotoCmd_Click()
    positions = Val(SetPosition.Text)

  '*******  With unit of nm  ********************
    If NanoMeter2.Value = True Then
```

```
      If (positions < UpLimitWave) And (positions > LowLimitWave) Then
        Call SecondRegPos(positions, Xt1Pos&, OK)
        OKMove = True
      Else: MsgBox ("Invalid value, Can not reach!")
      OKMove = False
      End If
  '********  With unit of cm-1  *****************
    ElseIf WaveNumber2.Value = True Then
      TmpPos = 10 ^ 7 / positions
      If (TmpPos < UpLimitWave) And (TmpPos > LowLimitWave) Then
         Call SecondRegPos(TmpPos, Xt1Pos&, OK)
         OKMove = True
      Else: MsgBox ("Invalid value, Can not reach!")
      OKMove = False
      End If
    End If

    If OKMove = True Then
    Call SecondRegPos2(Xt1Pos&, Xt2Pos&, OK)
    Call SecondRegPos3(Xt1Pos&, SHGPos&, OK)

'*******  set the absolute postion for each motor  ******

  '  If Xt1Pos& >= McGetPosition(Controller, 1) Then
    Call MCMoveAbsolute(Controller, 1, Xt1Pos&)
    Call MCMoveAbsolute(Controller, 2, Xt2Pos&)
    Call MCMoveAbsolute(Controller, 3, SHGPos&)
   ' Else
    'Call MCMoveAbsolute(Controller, 1, Xt1Pos& - BackLash(1))
    'Call MCMoveAbsolute(Controller, 2, Xt2Pos& - BackLash(2))
```

```
    'Call MCMoveAbsolute(Controller, 3, SHGPos& - BackLash(3))
    'End If
     Call MCWaitForStop(Controller, 0, 0.5)
    Else
    End If

End Sub
```